DESIGN, CHARACTERIZATION AND EXPERIMENTAL TESTING OF TWO NOVEL RECONFIGURABLE JOINTS

Ph.D. THESIS
presented to obtain the degree of
Doctor

Mykhailo Riabtsev

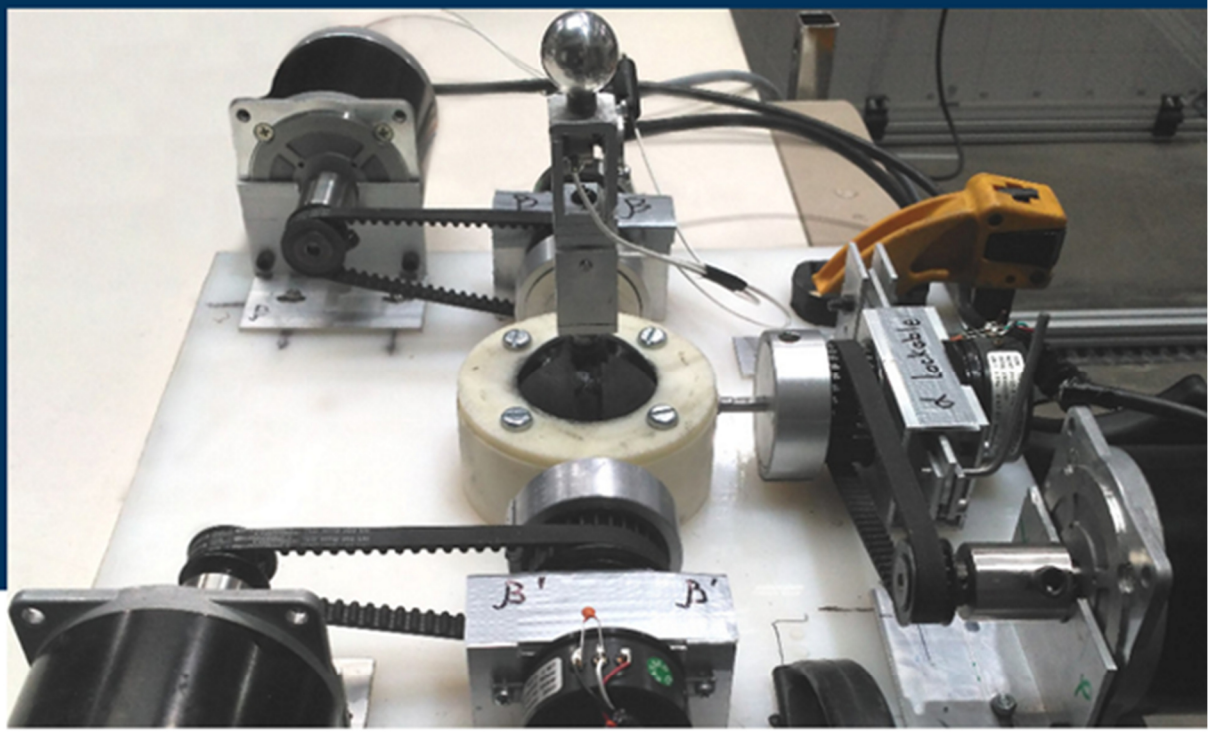

THESIS ADVISORS:
Prof. Dr.-Eng. Víctor Petuya Arcocha
Prof. Dr.-Eng. Mónica Urízar Arana

December 2021, Bilbao

eman ta zabal zazu
Universidad del País Vasco
Euskal Herriko Unibertsitatea

INGENIARITZA MEKANIKOA SAILA
DEPARTAMENTO DE INGENIERÍA MECÁNICA

eman ta zabal zazu
Universidad del País Vasco
Euskal Herriko Unibertsitatea
Ingeniaritza Goi Eskola Teknikoa
Escuela Técnica Superior de Ingeniería
Bilbao

Ph.D. Thesis

Design, Characterization and Experimental Testing of Two Novel Reconfigurable Joints

Presented by:

Mykhailo Riabtsev

belonging to the
Department of Mechanical Engineering
Faculty of Engineering in Bilbao
University of the Basque Country (UPV/EHU)
Spain

To obtain the degree of
Doctor of Philosophy in Mechanical Engineering

Thesis Advisors:
Prof. Dr.-Eng. Víctor Petuya Arcocha
Prof. Dr.-Eng. Mónica Urízar Arana

December 2021, Bilbao

Dedicated to my parents,

Feci quod potui, faciant meliora potentes

Acknowledgements

This thesis has been developed thanks to the research grant BES-2016-077073 provided by Ministerio de Ciencia e Innovación. I am very grateful for the ability to grow as a researcher and develop invaluable skills given by this opportunity.

I would like to express my deepest thanks to Victor and Monica for their guidance and encouragement, for being patient and understanding with me. Without their professional and moral support, I would not be able to complete this Thesis. I also would like to extend my sincere gratitude to Alfonso and Erik for their help with understanding the basics of parallel mechanisms and later my own creations as well. I am very grateful to Oscar for giving valuable advice and the opportunity of using the ultraflexible parallel mechanism in my experiments. It would be impossible to accomplish my studies without his help. I would also like to acknowledge the help of all the people who have participated in the practical testing of my haptic devices. They sacrificed their time and did their best to help me completely selflessly. I gratefully acknowledge the assistance of Raul, Isaak and Jose in all issues related to hardware manufacturing.

I would like to express my gratitude to Prof. Marco Ceccarelli for the excellent experience during my stay in the University of Rome Tor Vergata. He is an amazing person whose activity and hospitality impressed me to the core.

I would also like to thank Maria Jose for always being ready to help with any possible issue.

Finally yet importantly, I am very grateful to my wife Nastassia for her support and advice.

Abstract

This Thesis is framed within the scope of investigation of mechanisms and manipulators with reconfiguration capacity. The term reconfigurability refers to an ability of the mechanism to change its topology for changing the characteristics of this mechanism according to some varying tasks. The expansion of the parallel mechanism capacity by means of reconfigurability brings various benefits, including flexibility, cost reduction, and time saving. However, existing solutions do not outweigh the risks related to incorporating novel design solutions in production. Thus, there is still the open issue in a reliable reconfigurable solution that would prove to provide enough benefits to implement it in a commercially available manipulator.

This Thesis focuses on the conception and design of joints to be used in reconfigurable parallel manipulators. A set of different joint designs was proposed and subjected to characteristics analysis in order to select the ones that provide better qualities. From the comparison among the various designs, it will be shown that two of them present such potential benefits as big workspace area, high load capacity and accuracy, small inertia forces, simplicity of manufacturing, and small dimensions. Therefore, these two joints will be selected for further study, performing an in-depth analysis of their application as reconfigurable joints. Their kinematics and structural analysis have been carried out.

The selected joint designs have potential to be applied in various types of mechanisms where reconfigurability can be profitable. One of such applications is a haptic device. As one of the primary goals of the practical tests is design

validation by obtaining clear and unambiguous results, this application was chosen for testing the joints' performance and reconfigurability due to the simplicity of the necessary setup. It allowed to decrease the amounts of elements that potentially could affect the experimental testing results. Application of the proposed reconfigurable joints in a haptic device provides additional benefit consisting in an ability of performing precise straight motion along the selected axis.

The joints' reconfiguration ability and performance were tested by application of the joint prototypes in haptic device that controlled a 2-RFR planar ultraflexible parallel manipulator. The haptic device was equipped with a force feedback system that was intended to help indicating the singular areas of the workspace in which the control of the manipulator can be lost. Both joint designs were tested by a group of operators that was asked to perform several testing tasks. The results of the test demonstrate that the proposed joint designs are suitable for implementing them as haptic device and presenting the ability of joint reconfiguration. They provide reliable operation and control simplicity. After thorough analysis of the experimental results, the most beneficial joint design and the most appropriate control mode for it were determined. After adapting this design to conventional manufacturing technologies, the joint could be tested in a commercially available manipulator.

The Thesis is organized as follows:

In Chapter 1, the existing research in the field of reconfigurable parallel mechanisms will be presented. The reconfiguration methods will be reviewed with the further focus on the reconfiguration with special joints. Haptic devices related researches as an application field for reconfigurable joints will be

considered. The analysis of the market of commercially available parallel robots will be presented. The existing joint solutions that allow reconfiguration will be presented and analyzed.

In Chapter 2, a series of novel reconfigurable joint designs will be proposed. The characteristics of the proposed joints will be compared and two most profitable designs in relation to reconfiguration abilities will be chosen for further study.

In Chapter 3, two of the joints that have proven to be the optimum ones for reconfiguration purposes will be analyzed in-depth. The solution to position problems, velocity equations, workspace characterization, and the quasi-static and finite element analysis will be presented.

In Chapter 4, manufacturing of the joint and haptic device prototypes will be presented. The design of the experimental setups will be explained.

In Chapter 5, the prototypes were tested for functionality and in a haptic device application. A group of people was asked to perform several tasks, controlling the 2-RFR ultraflexible manipulator with the proposed haptic device. Aside that, the reconfigurability of the joints was tested. The results, their possible explanation and discussion will be presented.

Finally, the last chapter presents the summary of all the main conclusions derived from this Thesis. Besides, the possible directions of future work will be proposed.

General Index

Index of Figures

1. State of the art

1.1. Reconfigurable parallel manipulators

Manufacturing of any product is necessary to satisfy some demands of the market. Changes in the market force modifications in the production as well. Switching fast from manufacturing one product to another one is usually a complex task, as the readjustment can take long. Every hour of non-production causes money loss and losing the position in the market. That is why fast readjustment is a very urgent issue. Many researches were carried out, trying to improve the adaptability of the robots for different tasks. Reconfigurable robots is one of the possible solution to this problem. However, reconfigurability can be reached by various different methods. A discussion on the reconfiguration principles and strategies in [1] provided the definition of topology and configuration as a ground for the development of reconfiguration approaches. The topology of a mechanism represents the information on the arrangement, quantity and types of links and joints. Unlike the topology, configuration of the mechanism is described as geometrical characteristic, focused on parameters of the links and joints relative to each other, for instance, lengths, angles, positions. The study comes with four ways of reconfiguration. It states that reconfiguration is possible if one of the next parameters changes: the number of links/joints; joint types; the adjacency and the incidence of links and joints; geometrical locations of the joint. By analyzing these possibilities, several reconfiguration strategies were formed. Among them – special kinematic geometry – the ability to change the topology and configuration in some particular positions of the mechanism. Another strategy consists in locking joints or actuators. In this case, in some

position, some degree of freedom (DOF) of the mechanism becomes blocked which causes topological and configurational changes. Next strategy is design of special links and joints and obtaining reconfiguration by these design features. The strategy of selection of multiple input variables is claimed to be most used [1]. It involves control of a complex mechanism by selection of the proper input variables among the variety of possible ones. An example of this method can be seen in selective actuation applications [2], [3] and modular robot systems [4–7] .

Several studies focused on classification and analysis of the reconfigurable manipulators were carried out. The main purpose of these research was to simplify the design process of reconfigurable mechanisms. The work [8] reveals five types of morphing, which are used for reconfiguration: topological morphing, geometrical morphing, connectivity and mobility change in furcating morphing, several types of furcating morphing, and joint-motion morphing. In this classification, by topological morphing, author means reconfiguration by physical constraints of the joints design, lockable joints and internal forces, like springs. Geometrical morphing includes manipulations with joint axis positions, joint axes orientation related to links, special joints, using internal mobilities and plane symmetry. Connectivity and mobility change in furcating morphing is mostly focused on creation of different configurations of the mechanism through passing of the singularity positions. Types of furcating morphing refer to the ways of getting several operation modes of the mechanism, including selective actuation and special design of the mechanism or its joints. Joint motion morphing takes place when the manipulator can have idle mobility. For instance, the joints of the mechanism in this case can switch between active and idle state. Despite some of the morphing types can be implemented by similar means; these

means are used in a different way, which differentiates these morphing types.

The task-based classification of the joints of reconfigurable mechanisms was presented in [9]. This classification is based on the Assur groups that can provide certain kind of motions. It simplifies the structural synthesis of the mechanisms. The work also includes mathematical means of the proposed classification. The proposed method of task-based design, proposed in [9] was tested by creation of the prototype of a robot for extra-high-voltage (EHV) power line repair. The robot is planar and has two DOF and the kinematic chain of 2-PRRR. Two legs of the robot hold the nut cut in special way, which, when connected and rotated, can fix the EHV cable by repositioning the broken wires.

In the paper [10] complex joint types are considered. The researchers proposed a special approach, based on screw theory, for the analysis of the mobility characteristics of complex joints. To make the analysis simpler, the joints were united into three groups: joints with single-closed-loop kinematic chain (SKC), joints with multi-closed-loop kinematic chain (MKC), and joints with local-closed-loop kinematic chain (LKC).

1.1.1. Modularity approach for reconfigurability

One of the ways to readjust a robot from one task to another is to design it from standardized modules, which are easy to connect and assembly, like a Lego construction set. Several researches used this approach to solve the readjustment problem.

In paper [4], an automation solution suitable for low volume and high-mix production was proposed. The focus of the research was to create "plug-and-

play" modular reconfigurable component-based robotic system, which will provide rapid reconfiguration of the production line (robotic cell). The paper provides the description of the module design (fixed dimension, including passive joints, and variable dimension modules). Active modules have one DOF each and are divided into two types: R-joint and P-joint. Passive modules have single R-joint, or U-joint. The modules of the system are presented in Figure 1. Variable dimension modules are parts, which are necessary to connect fixed dimension modes. These parts are designed so that they will be easy to manufacture in purpose of speeding up the readjustment process.

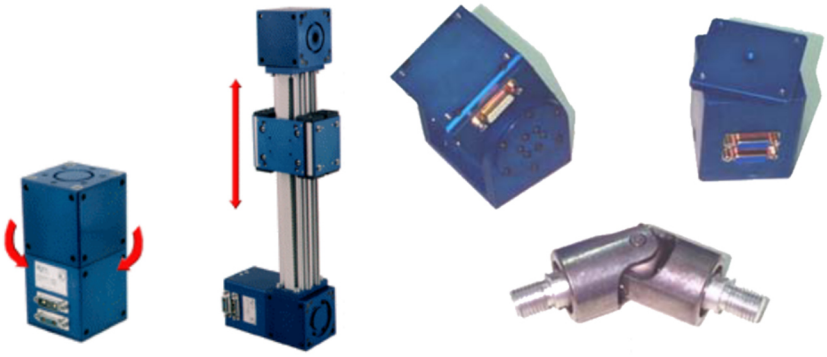

a) b)

Figure 1. The modules of the system [4]: a) actuated joints; b) passive joints

The developed concept was tested on a prototype of a work cell, consisting of 7-DOF redundant serial robot, a 6-DOF 3-RRRS parallel robot, and a 1-DOF conveyor. This work was continued in research [11], where two parallel robot configurations, consisting of three legs, are considered. Robot links are the same types as in [4]. The robotic modular system was designed for general applications for work in a production line. The research focused on three legs robot configuration as it was considered as optimal due to uniform load

distribution and minimal risk of leg interference. The configurations consisted of two joints with actuators (P or R types) and two passive joints (R and S types). There were five RRRS configurations with different joint axis directions and eight configurations with a prismatic joint (PRRS and RPRS).

In paper [5], similar approach for the reconfigurable tripod was considered. In this research the same actuators, joints and connection links are reused for each configuration of the robot. The base and the end-effector platforms are manufactured for each new task. The legs of the tripod were attached to linear actuators, fixed on the base platform with universal joints, and with spherical joints to the end-effector platform. Thus, leg kinematic chain can be characterized as PUS. The tripod configurations could include a passive leg between the platforms, which made mutual translation motion impossible. These platforms are presented like easy-to-manufacture parts for different configurations. In this research, the efficiency of the motion transformation, in other words, motion purity was used as an optimization criterion.

The modular structure has found its application in mobile robots. The authors of [6] present LOCOBOT - an assisting mobile robot for different tasks, which is equipped with the modular arm, capable to be readjusted. The robot arm of LOCOBOT has a modular design; it allows offline changing of the dimensions of the arm according to the task. The modules of the arm are active joints of revolute and prismatic types and passive links of constant length. The robot arm has PRRRP kinematic chain. One of the main features of the research was safety, due to the robot-human interactions.

The other way to readjust of a mobile robot is self-assembly. In this case, the whole robot is used as a module. In [7] the usage of parallel mechanism in

reconfigurable mobile robot system is studied (see Figure 2).

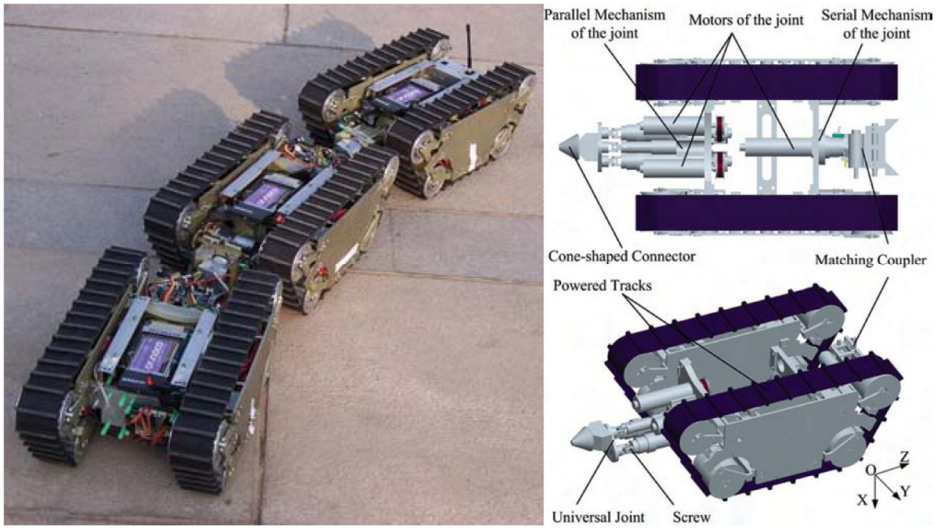

a) b)

Figure 2. Mobile self-assembly robotic system [7]: a) connected; b) internal design.

In the robotic system presented in Figure 2, a separate mobile robot module has a parallel platform with docking mechanism, which allows it to make an assembly consisting of two or more robot modules. The platform moves around a passive leg U-joint. It is moved by other two legs, which are attached to the platform with U-joints and actuated by H-joint (the screw). This structure allows robot assembly to gather, as well as to pass different obstacles, like grooves and bumps.

1.1.2. Reconfigurability by means of additional actuation

Going through some singular positions implies a loss of control of the mechanism, which may require an additional actuation. In [12] the

kinematotropical mechanism examples were introduced. In this kind of mechanisms, different number of global mobility can exist, depending on the positional parameters of the mechanism. Depending on the position, different number of actuators is necessary to control the mechanism. The transition from one mobility number to the other happens when the singularity position is being passed. Several examples of the kinematotropical mechanisms were considered: planar Wunderlich mechanism and spatial - Wren's platform and novel RR(4R)(4R)RR mechanism (The Queer Square).

The problem of the singularities and the methods of their elimination is assessed in review [13]. Redundant kinematics and actuation are one of the possible solutions. It can include the actuation of passive joints and by including additional kinematic chains, which do not increase DOF of the robot. This actuation can be temporary and used only in case the mechanism gets into a singular pose. Redundant actuation can also provide better distribution of the load among the actuators. In some cases, such actuation can provide more fail-proof mechanism, because failing of one actuator will not lead to mechanism failure.

1.1.3. Reconfigurability by detaching and reconnecting the kinematic chains

A reconfigurable robot for multimode tasks, which consists of two separable tripods, is proposed in [14]. The robot is capable to combine assembly and pick-and-place operations. The main feature of the robot is that swinging tripod can be detached from the sliding tripod to perform the gripping operations, which are impossible for the initial configuration (Figure 3).

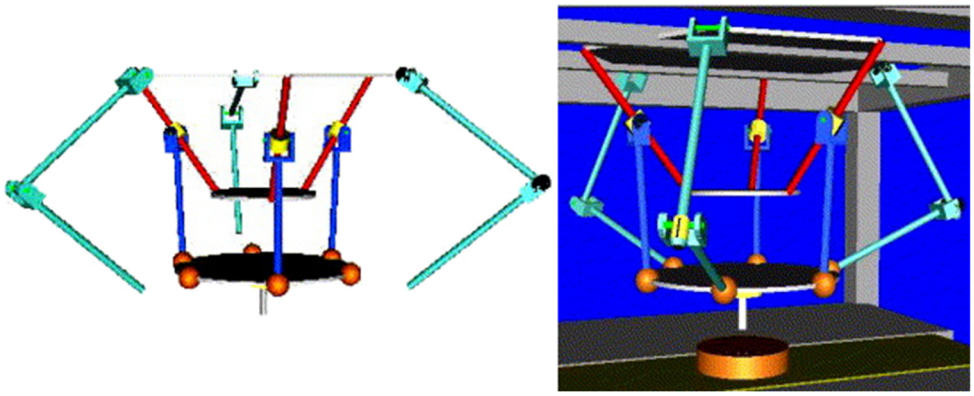

a) b)

Figure 3. Reconfigurable robot, containing two tripods [14]: a) tripods in detached position; b) tripods attached.

In this study, the reconfigurability is achieved by the ability to change the amount of DOF from 6 to 3, depending on the task, by detaching and attaching the joints of swinging tripod. Separability is reached by using magnetic joints, which connect swinging tripod legs to the platform.

Legs of the sliding tripod consist of a cylindrical joint attached to a revolute one, so they form a universal joint, and together they are attached to the moving platform with a spherical joint. A leg of the swinging tripod has a configuration of RUS, with S-joint detachable. In both legs, universal joints have one lockable axis. This feature is necessary for reconfiguration of the robot.

In [15] a concept of a novel parallel manipulator, called PARAGRIP is introduced. This robotic system uses the object, which is being transported, as a moveable platform that unites the legs of the structure. The legs separately from the moving platform (the object) consist of serial manipulators equipped with self-adjusting grasping mechanism, mounted on U-joint. The reconfigurability

in this mechanism is implemented by combination of using different number of limbs with different configurations and functions. This concept can be considered as a robot with decoupling limbs. The PARAGRIP system is presented in Figure 4.

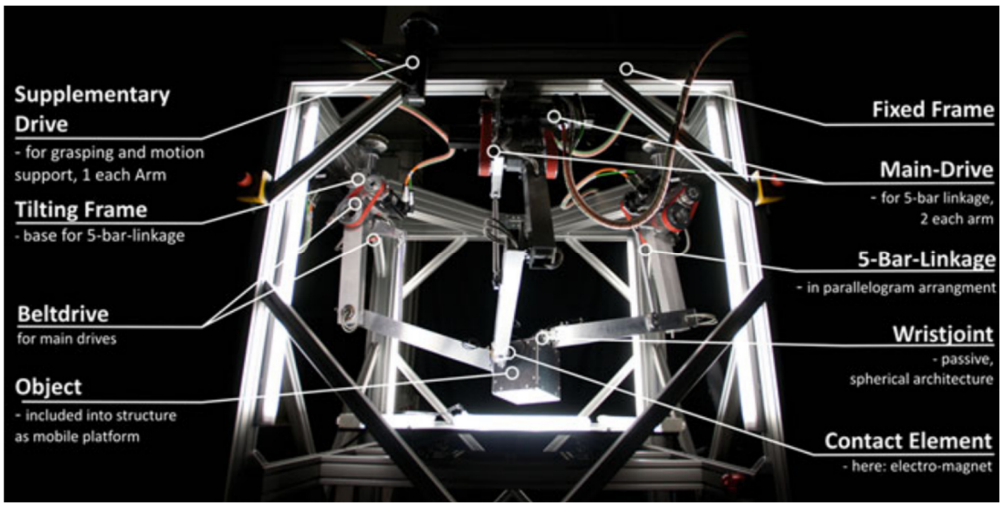

Figure 4. The PARAGRIP system [15].

In research [16] a robot was proposed, which is able to reconfigure without stopping during its operation. This parallel mechanism can change its amount of DOF from 6 to 5, 4, and 3 by detaching the legs and blocking the passive joints. The robot has 6 legs: 3 fixed and 3 detachable. Detachable legs have RRS kinematic chain in all robot designs, and for the fixed legs design variants were proposed: RUS, URS, PUS, UPS, and CPS. The fixed legs have one lockable joint to be able to stay under control when the other legs are being detached. The robot with PUS kinematics of the fixed legs is presented in Figure 5.

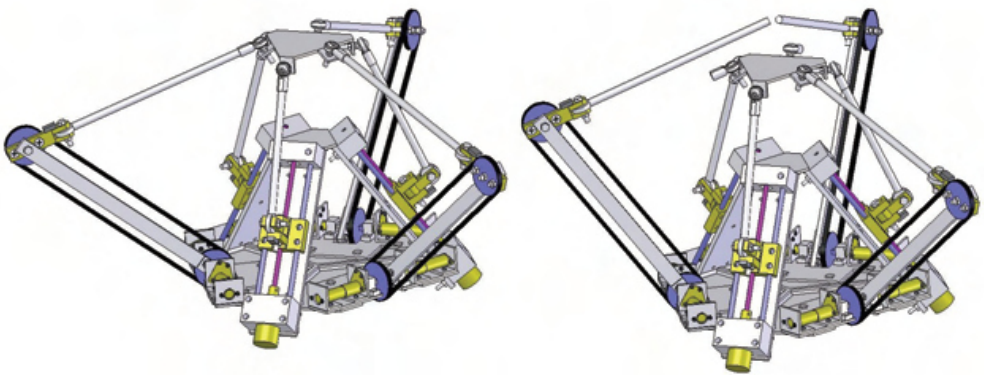

a) b)

Figure 5. The reconfigurable robot with detachable legs [16]: a) with fully attached legs; b) with partially detached legs.

In [17], another reconfigurable manipulator is presented, 4 –RUU parallel manipulator. The robot has four revolute joints actuated and universal passive joints. The decomposition of this mechanism into two 2-RUU manipulators (the prototype can be detached into two equal parts, see Figure 6) has demonstrated that it can work in two Schönflies modes and one 2-DOF motion mode.

The robot has one singular position in each of the Schönflies motion mode, two self-motion positions in the second Schönflies motion mode and possible self-motion positions in 2-DOF mode, when the links positions satisfy certain conditions. The robot cannot turn from one Schönflies mode to the other, because they do not have common configurations, but it is possible through the third mode of 2-DOF.

a) b)

Figure 6. 4-RUU reconfigurable manipulator [17]: a) attached as 4-RUU; b) detached as two 2-RUU.

1.1.4. Reconfigurability by changing the geometric dimensions

One of the ways to change the robot kinematics is varying the dimensions or the configuration of the base platform or end-effector platform. In research [18] reconfigurability was implemented by rearranging the places where the legs of Gough platform robot are attached to the base. The movement of these points was implemented with linear actuators. The change in location of the attachment points causes the variation of the workspace without altering dynamic characteristics. The research was focused on finding the optimal geometry of the modular parallel robot. Two criteria of optimality were used: workspace size criterion and the minimal necessary stiffness criterion. The second criterion appeared to be the most influencing and has been proposed as an optimality index.

Similar way of reconfiguration can be found in the paper [19], where points of

limb attachment lay on the linear guides. Here, linear guides are arranged into three groups with two guides in each. The guides in one group are parallel to each other. The groups are arranged in a three-beam star with the angle of 120 degrees between the beams.

Research [20] presents a variant of a reconfigurable Stewart-Gough platform, which can change the dimensions of its base platform. The platform performance is to operate some axisymmetric tools, like 5-axis milling machine. The mechanism has 5-PSPU kinematic chain. The legs' points of attachment to the base can be reconfigured during the operation or offline, keeping the same singularity locus of the mechanism. This feature is implemented by using linear actuators to move the spherical joints of the legs.

In [21], reconfigurable base platform has the shape of three beam star and is equipped with linear guides. The movement of the limb attachment points are not independent. Their displacement is driven with the same actuator, which is placed in the center of the star. The base platform can obtain different shape with the linear guides and rotary joints (see Figure 7).

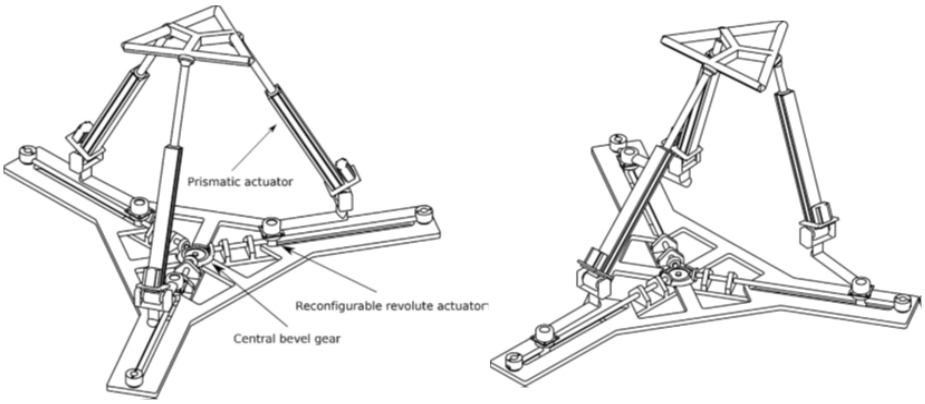

Figure 7. Reconfiguration of the base platform with linear guides and rotary joints [21].

Research [22] is the continuation of [21]. In this research the manipulator has the similar shape and actuation of the base platform. But as it can be seen from Figure 8, the beams of the star, which forms the base, can have inclination. Also, it has one intermediate triangle platform.

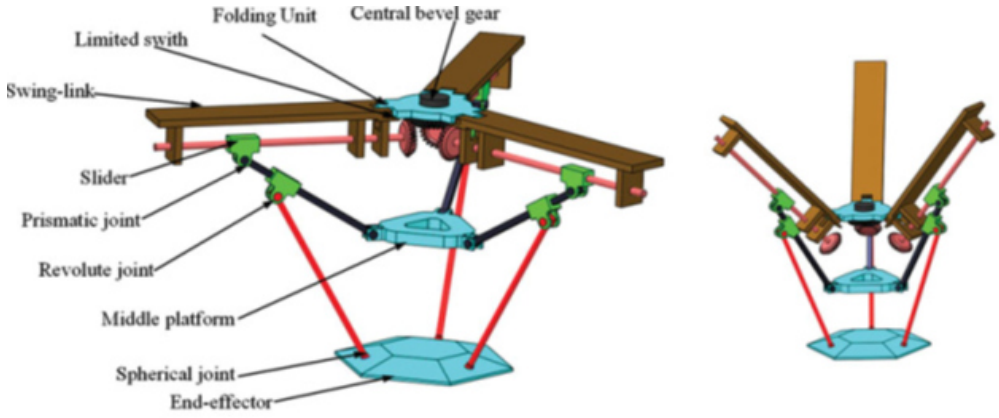

Figure 8. Reconfiguration of the base platform by the inclination of the linear guides [22].

In paper [23] the influence of the base and end-effector platform sizes on the robot's adaptability is analyzed in a planar robot and Stewart platform. Four structures were developed to implement the concept (Figure 9). The first two structures are similar to the design presented in [20]. The third structure has two sets of three limbs joint in each. The joints in the set are connected to the three-beam star, which form the base. Two stars can turn around their centers, one relative to the other, thereby changing the polar angle. The fourth structure has similar configuration as the previous one, but the stars can have inclination relative to each other. All the variants of Stewart platform have 6-UPS kinematic chain. The planar manipulator has PRPRPRP structure. Two prismatic joints form the base platform. The legs of the mechanism have PRPR structure.

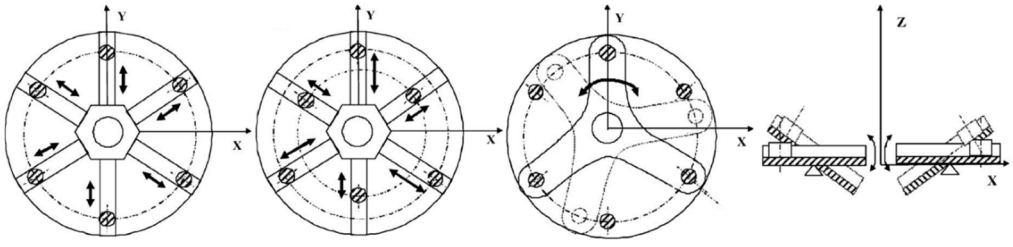

Figure 9. The four designs of reconfigurable mechanisms with changeable base platform [23]: a,b) changing the polar radius; c) changing the polar angle; d) inclination of the platforms.

Other variant of using linear guides for base platform reconfiguration is studied in the paper [24]. In this research, the special design of a delta robot was considered, where the grid of linear guides formed the base platform (see Figure 10).

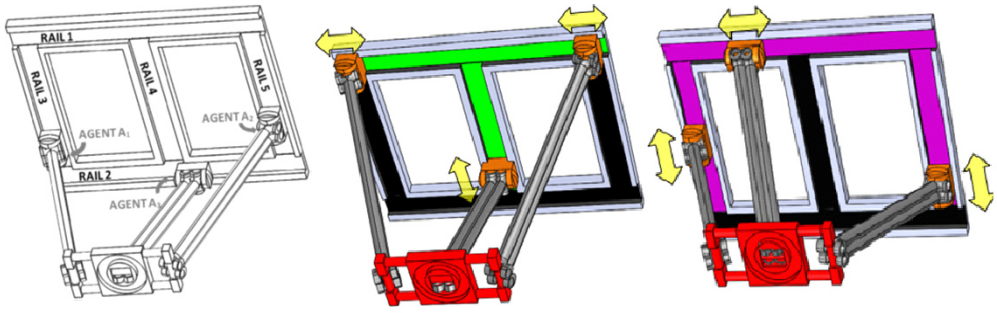

Figure 10. Reconfigurable manipulator with grid-like base platform design [25].

As can be seen from Figure 10, the linear guide carriages can travel from vertical to horizontal guides. By these means, different shape of the base platform and

workspace can be obtained.

A reconfigurable spherical wrist was presented in [26]. The implementation of the wrist is a 4-bar spherical mechanism (see Figure 11).

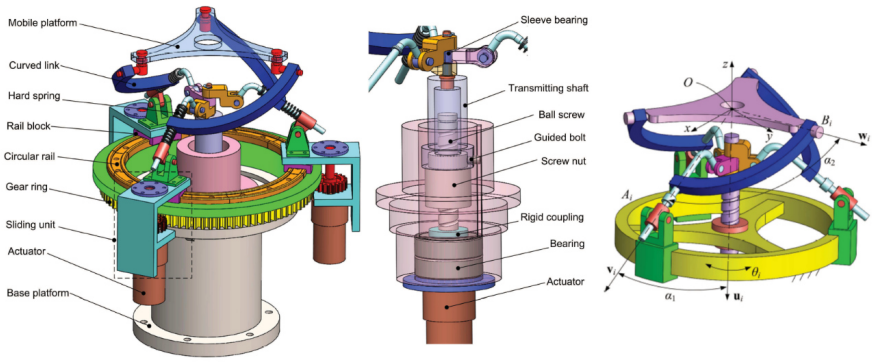

Figure 11. A reconfigurable spherical wrist [26].

As it can be seen, the base of the wrist can be reconfigured by changing the angle α_1 between the vertical axis U_i and inclined axis V_i. This angle can be changed by the actuator, which is placed in the center of the wrist. The mechanism has HRRPR structure. It can find applications in serial robots as an active spherical joint (in the wrist) and in humanoid robots as a waist joint.

Paper [27] presents a parallel wrist for the serial robot, which provides spherical movement. The wrist was designed to be mounted on a serial assembly robot, but authors admit that the resulting prototype is too big for this purpose [27]. The first concept of the wrist had 3-RRR structure, but later simulations and the prototype had 3-PRPS. The prototype has a triangle-based pyramid base platform with P-joints mounted on it. This feature allows referring this mechanism to mechanisms with a variable shape of the base platform.

In [28], a 3-PRS manipulator for high precision operation of the telescope mirror was proposed. In this 3-DOF platform, prismatic joints, fixed on the base platform of the robot are actuated. Thus, by actuating them the shape and dimensions of the base platform of robot are being changed during the operation.

Paper [29] considers reconfigurability of the legged walking robots with the purpose of creation of adjustable leg for different ground surfaces. In this work, the mechanism designed by Theo Jansen is considered, which originally has 1 revolute actuator. In the mechanism, proposed in the research (Figure 12), three bars of the leg were replaced by the prismatic actuators. This feature allows the leg to change its geometry by changing the lengths of the links, according to the surface, on which the leg steps. This mechanism cannot be classified as a leg of a parallel manipulator, because it is a mechanism itself with a complex kinematics.

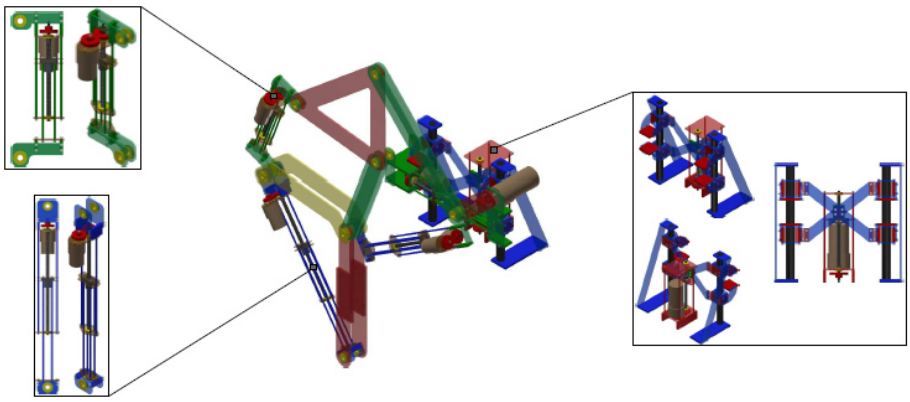

Figure 12. A reconfigurable leg for walking robots [29].

The reconfigurability of internal combustion engines with the purpose of decreasing fuel consumption and emission amount was studied in [30]. The desired effect is gained be changing the compression ratio which depends on the

volume of the combustion chamber. The patent search has shown that most of the proposed mechanisms had variable dimensions of some links of the mechanism, which had influence on the combustion chamber volume. All the mechanisms have 2 DOF, one of which was related to the piston with the crankshaft and the other is related to the reconfigurative mechanism.

An asymmetric 3-UPU manipulator was presented in paper [31]. It constitutes a Stewart-Gough platform with several asymmetrical parts: the moving platform and the universal joints which are attached to the base platform. The moving platform has triangle shape. The vertices of the platform, where the limbs are attached, are bent at the same angle: two in one direction and one in the other. The lower U-joints have an asymmetrical design to provide bigger rotation angle in one plane. The manipulator has translational (3T) and rotational (spherical) modes. The reconfiguration of the manipulator needs to be performed offline, because it requires turning the platform upside down. The researchers do not specify the application of this manipulator, but it can be assumed that it can be applied the same way as other Stewart-Gough platforms.

1.1.5. Reconfigurability by blocking actuators or joints

Another way of getting reconfigurability consists in blocking or releasing some actuators or passive joints of the mechanism. An example can be seen in paper [32], where 5 and 4 legged platforms with lockable joints are presented (see Figure 13). The leg type, used for both robots was RbRPS, where joint Rb can be blocked, and allowing reconfiguration to happen. This design provided the platform operation in six-dimensional space, as well as the singularities avoidance and actuator force reduction. In the proposed robot, only P-joints are

actuated, other joints are or passive, or lockable.

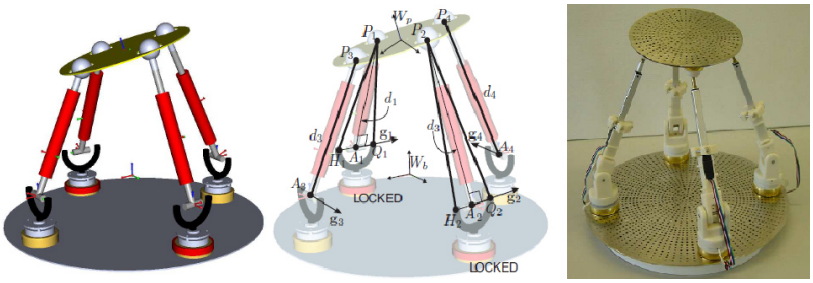

a) b) c)

Figure 13. A reconfigurable 4-RbRPS parallel manipulator [32]: a) general model; b) locked configuration; c) the prototype.

The actuation blocking concept can be also implemented on a software level. This approach is called selective actuation. In [1] 3-CPPRR parallel manipulator was presented, which can change its DOF-s by using selective actuation. Cylindrical joints are actuated, every other joint is passive. The R-joints axes of each link intersect in a common center, allowing spherical motion. Depending on the actuation, 3 DOF spherical, translation or hybrid motion types can be obtained. In addition, robot provides 6 DOF spatial motion when fully actuated. The potential application field of the robot is high precision micro and nano assembly.

Paper [33] is focused on the type synthesis of the multiple DOF parallel mechanism, which can change the motion pattern by choosing the necessary actuators, depending on the task. In this research, no particular application for the robots was proposed. Various types of legs were considered and three main classes for the legs that combine spherical and translational motion types were synthesized: 5R, 4R1P and 3R2P. A 3RRRRR mechanism was used to study

transition between motion types.

In research [3], decoupled motion is considered. In this case, the control simplification is obtained by dividing the motion to certain groups, with different actuators assigned to them. This can reduce the size of the Jacobian matrix of the mechanism and speed up the calculation. This is a particular case of selective actuation, when, for example, rotational DOF-s are separated from translational DOF-s in calculations and motion. In this research, several three-legged mechanisms were presented. The legs kinematic chains were PRPPRR, RPPPRR, PRRS, RPRS, PRPS, RPPS, PPRS, and PPPS.

In paper [34] the work in the field of decoupling of the groups of motion [3] is continued. Here the approach for type synthesis of symmetrical 3-legged 3-DOF mechanisms was proposed. In the proposed mechanisms, the vertical translation can be controlled independently from two horizontal rotations. The new architectures which were obtained in this work had PRRS, PRPS, RPPS, PPRS, and PPPS leg structure. First two joints of each limb are actuated.

A methodology for design and analysis of robots that are capable of changing their operation modes was presented in [35]. As an example, the analysis of three-legged UPS robot with blocking actuators was carried out.

A reconfigurable parallel mechanism for pick and place operations that can provide pure translation motion and pure rotation motion patterns is presented in [36]. It utilizes lockable universal joints in 3-CPU kinematic chain (Figure 14). The lockable joint has three axes. The reconfiguration occurs when the proper axis of the universal joints is being locked. The mechanism does not have singularities in the translation mode, but has singularities within the workspace

in the rotation mode. The authors claim that using several robots of proposed design in assembly operations can increase flexibility and adaptability of the assembly system. This research is a continuation of the previous work [27], where the design of a robot wrist for assembly purposes was proposed.

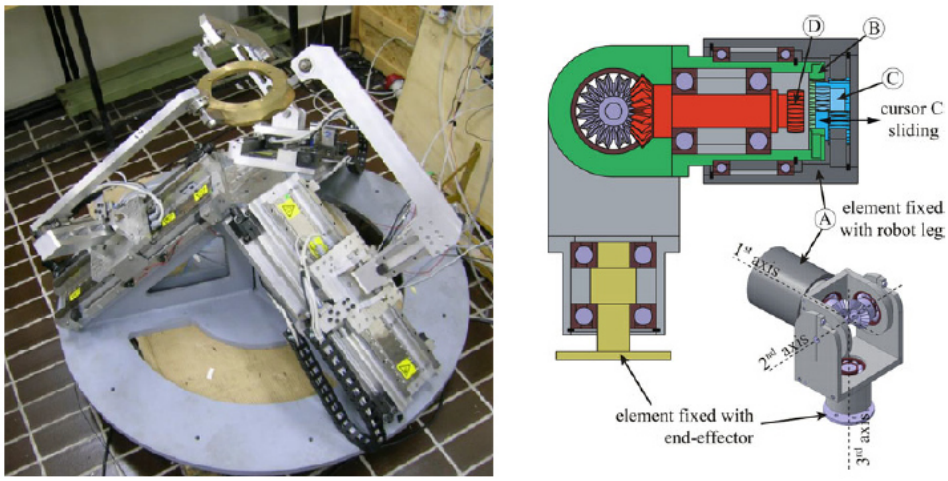

a) b)

Figure 14. 3-CPU mechanism [36]: a) general view; b) reconfigurable U-joint.

In research [37] the 3-URU manipulator with metamorphic joints was presented. By the means of locking U-joints, which are attached to the base platform of the robot, two motion patterns can be obtained. Depending on the configuration and the locked axis, the robot can have three rotational movements, the axis of which are perpendicular and intersect at one point, thus forming a spherical motion, or it can have a pure translational configuration [36] [37].

A manipulator with lockable joints, which can change the motion mode from three translational DOF to three rotational DOF, was studied in [38]. The mechanism has three legs with RRRR structure. The legs are connected from

one side to the fixed platform, but from the other side they are connected to special 4R mechanism, similar to which were used in [39]. These 4R mechanisms (Figure 15) provide different kind of motions, depending on the way it is being folded.

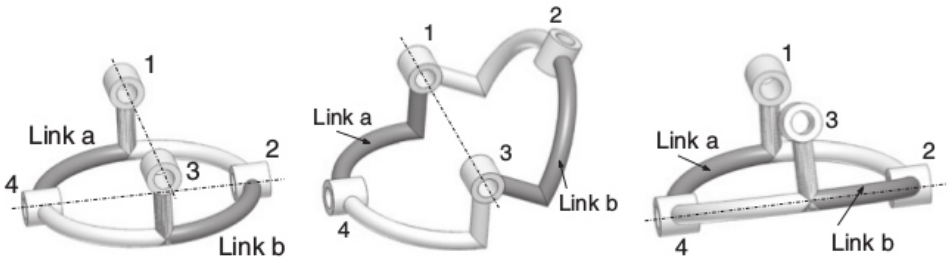

a) b) c)

Figure 15. 4R mechanism [38]: a) Transition configuration; b) R| mode c) R_ mode.

The mechanism is equipped with lockable joints, which allow the manipulator to reconfigure. The advantage of this solution is the absence of singularity positions and self-motions during the reconfiguration.

In the work [40] the holonomic under-actuated robots were studied. The research considered several planar examples of 4-RPR mechanisms with variable topology. The topological variations were implemented by the lockable passive prismatic joints. The concept was intended to be a variable wing structure (Figure 16), which could change the plane wing shape according to the necessary aerodynamics. The spatial structure has two interconnected 8-SPS mechanisms. Four legs of each mechanism are equipped with lockable passive prismatic joints and the other four legs of the mechanisms contain actuated P-joints.

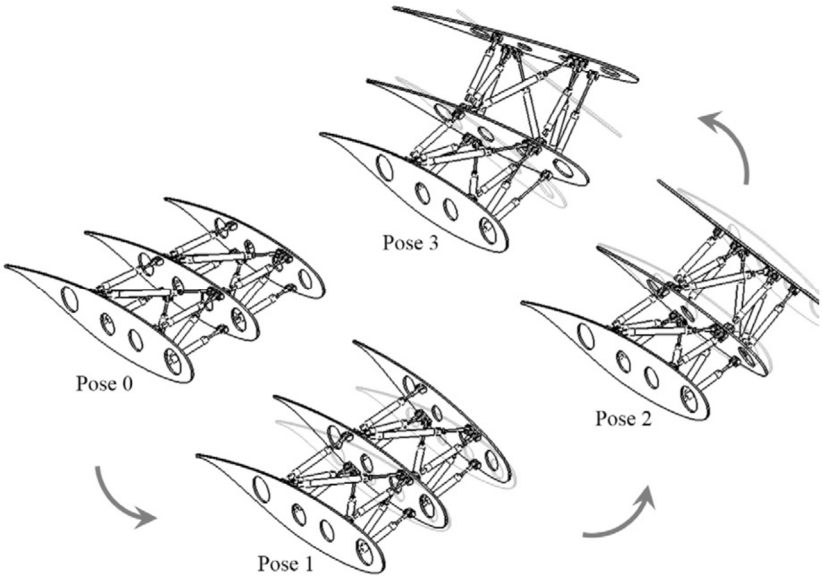

Figure 16. Variable wing structure [40].

A class of modular reconfigurable robots was presented in [41]. The mechanism implements 3-CPU under-actuated topology. The universal joint of the leg consists of three revolute joints, each of which is lockable. By these means pure translation or spherical motion can be obtained. As it is stated in current work, the approach can be implemented in different in 3-CRU structure, which has the advantages of removing P-joint, but on the other side, it requires more complex kinematic relations. The prototype, which was used to prove the concept, consisted of two separate modules, placed one on top of the other. The lower module was the spherical wrist, described in previous works [27], [36]. The upper module was a 3-CPU mechanism. The prototype was designed for assembly purposes, the lower module was planned to serve for orientation tasks and the upper one is designed for translation tasks.

New metamorphic joint is presented in paper [42]. This joint consists of three

revolute joints (see Figure 17). In the initial position, the axes of the revolute joints are perpendicular to each other. Axis 1 or 2 can be blocked, so the joint provides 2 DOF. Based on these joints, an asymmetric mechanism was simulated. The resulting metamorphic mechanism can implement 1R2T and 2R1T types of movement. The goal of this research was to create a method for development of the mechanisms with such movement types.

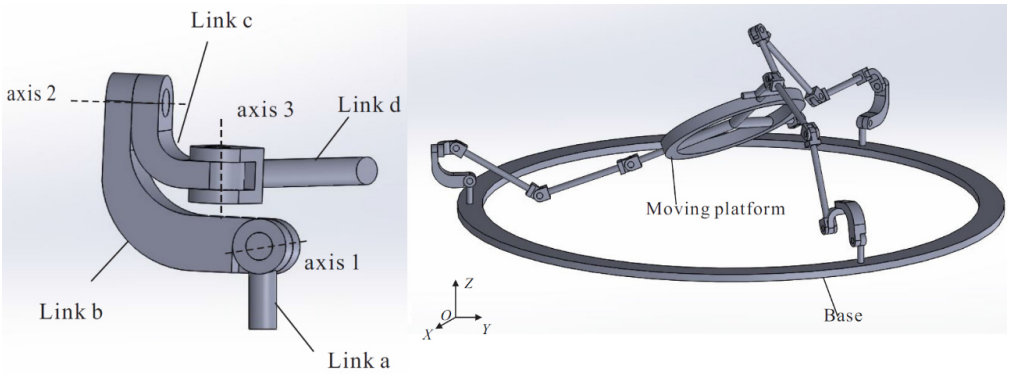

a) b)

Figure 17. A novel metamorphic joint (a) and a mechanism based on it (b) [42].

A spherical 3RPRP mechanism is studied in research [43]. The manipulator composes 3-RPR and 3-RRP mechanisms. The prototype and the CAD model are presented in Figure 18. The reconfiguration of the mechanism occurs when one of the kinematic pairs is being blocked. By blocking a certain pair, ten different types of kinematic limbs can be obtained. This spherical mechanism can find its application in shoulder and waist joints of the humanoid robots, in antennas orientation systems, engraving machines and others.

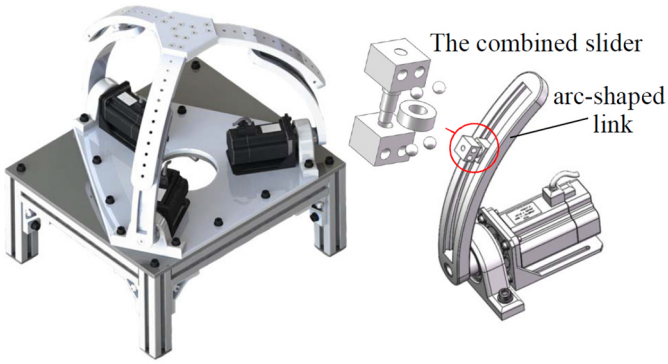

Figure 18. Spherical 3RPRP mechanism [43].

Ragnar - a 3T1R reconfigurable manipulator, was analyzed in paper [44]. The robot constitutes a 4-limb delta-robot with a special mechanism mounted on the moving platform (see Figure 19).

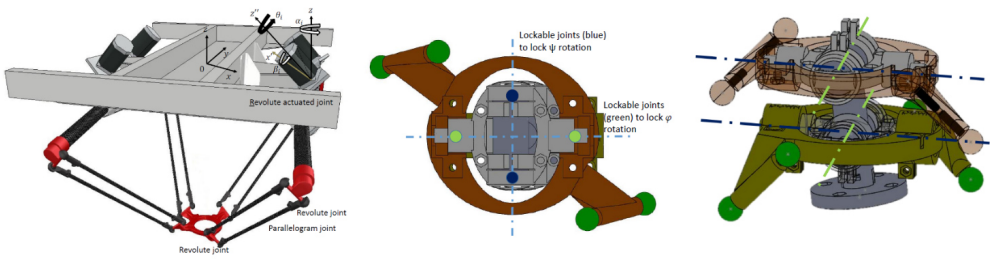

Figure 19. Ragnar - a 3T1R reconfigurable manipulator [44].

The mechanism has a set of lockable rotary joints, which allows changing the movement modes of a robot. When every joint is locked, the robot is in overactuated mode; when unlocked, it is in underactuated mode. If it is partially locked, the robot has 3R1T movement, with pitch or roll rotation, depending on which joints are locked. The purpose of the robot was to increase the amount of possible movement patterns with the same amount of actuators. The Ragnar

robot is described as a $4-\underline{R}RP\Pi R$ type (Revolute-Revolute-Parallelogram-Revolute serial joint arrange).

Among the research works developed by COMPMECH group, a methodology for analysis of multioperational capacity of reconfigurable parallel manipulators was developed in [45]. This research is focused on obtaining a variety of low-mobility parallel manipulators, which maintain constant motion patterns along their whole workspace. It is implemented by using selective actuation on 6 DOF manipulator. The concept was tested using the prototype of a 3-$\underline{C}$PCR mechanism, which provided different types of motion: Schönflies, Cartesian and planar.

1.1.6. Reconfigurability by changing the orientation of the joint axis

Reconfigurability by changing the joint axis orientation was proposed in [46]. A novel joint, called Hook (rT) joint, was introduced (Figure 20). It was implemented in two robots, which had triangular platforms and three limbs. First of them had 3-rTPS structure, the second one had 3-rT$\underline{P}$rT and the third one had 3-SPS with a central strut of rTPrT structure. The work was focused on study of mobility changes depending on the chosen actuation of the rT-joint.

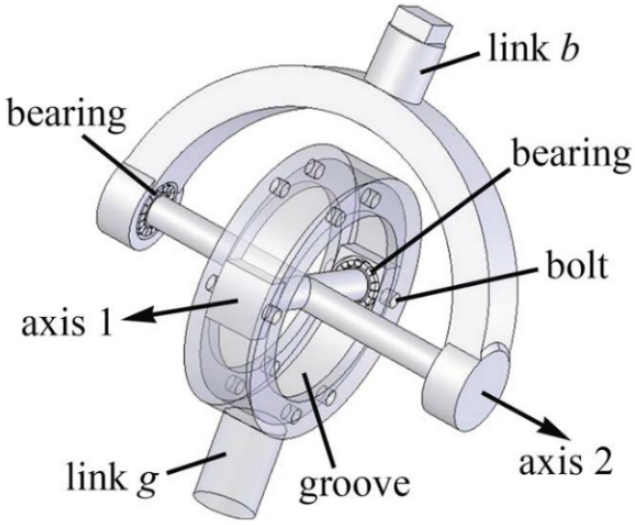

Figure 20. An rT-joint [46].

The authors continued with the implementation of the reconfigurable rT joint in other type of robots. In paper [47], a robot with three limbs connected to three mutually perpendicular base surfaces from one side and the end-effector platform from the other side is presented. The rT-joints, used in this research, are in fact U-joints, which are able to change the orientation of the axis in one of the R-joint that it consists of. The axis is turned 90 degrees from its original state, so the movement of the second R-joint becomes blocked. It causes changing the kinematic chain of the leg from UPS to RPS, which totally changes kinematics of the robot.

Research [48] continues the previous one [47] and proposes a mechanism which can provide pure translational motion or pure rotational motion. The mechanism limb has 3-rTPrT kinematic chain.

A manipulator, based on reconfigurable revolute joints (rR), is presented in [49]

It has two possible motion modes, depending on the direction of the axes forming the rR joint - 3R and 1T2R. The mechanism has three legs of rRPS structure. The rR joints are fixed to the platform with the certain inclination angle. Due to the proposed joint design, the axes of the rR joint can vary their directions resulting in changing the type of motion of the end-effector platform.

Another research [50] with rR joints was on 3-rRPS metamorphic parallel mechanism which provides several motion patterns. Depending on the configuration, motions can be 3 DOF coupled rotational, 3 DOF planar or 1T2R.

The work [51] presents the class of robots, which is capable to perform 3T1R motion. The robot considered in the article is noticeable because it consists of the same kinematic chain as H4 and Delta robots, which is 4-PRPaR, but in comparison to them, it can provide one additional rotational DOF. It became possible due to the rearrangement of all the joint axes of the manipulator, so they became parallel to each other. Although this mechanism is not able to reconfigure, the research proves that the same kinematic links can have different behavior in different configurations. The robot has very simple sub-chain topology, which is profitable for 4-DOF transportation and orientation operations.

Research [52] is a further development of [17]. Here, a 4-rRUU manipulator was presented. In this manipulator, reconfigurable revolute (rR) joints are used. The axis of rotation in these joints can be inclined manually, which allows obtaining pure translation movement mode and Schönflies motions with different axis of rotation. Double Hooke's joint is used in rR-joint to transmit the rotation from the actuator to the limb (see Figure 21).

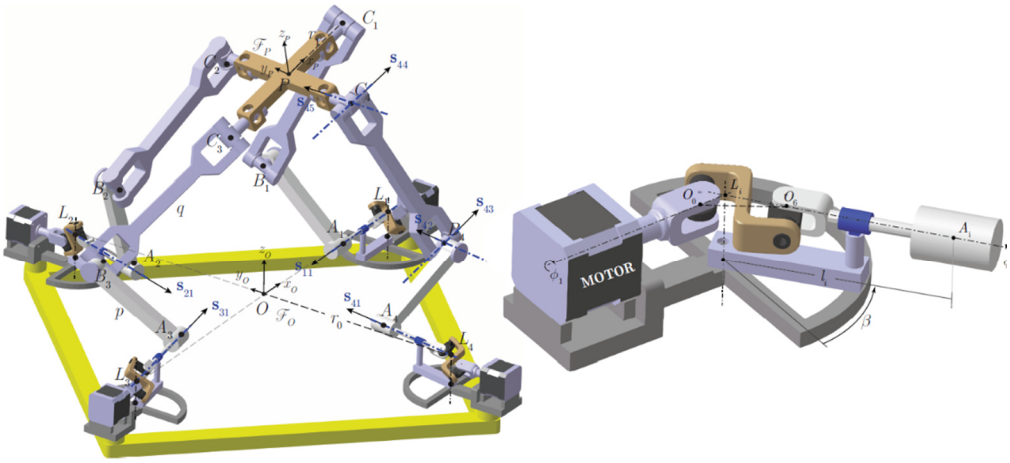

Figure 21. 4-rRUU manipulator [52].

1.1.7. Reconfigurability by using special joints or links design

Another possible way of reconfigurability is to develop special joint designs, which can change the motion type. Research [53] is focused on variable joints, which combine rotation and translation (RP-joint). The example of such joint and the real application is presented in Figure 22. The joint has a fixed part with the circular opening, in which other part that has rectangular shape is able to rotate. To allow this rotation, the short sides of the rectangular part have rounding of the same radius with the opening. In one side of the circular opening, there is a groove, with the same thickness as rectangular part. Therefore, in some point of rotation the rectangular part can get into the groove and change the motion type from rotation to translation. Reconfiguration of the robot is realized by changing this motion type, as if the joint was changed from R to P.

a) b)

Figure 22. Variable R-P joint (a) and Knipex adjustable pliers (b), based on a similar principle.

The other special joint example is presented in the work carried out in [54] devoted to the non-actuated rehabilitation mechanism. The mechanism is planar; it has two configurations for training only hip or only knee. It changes from one configuration to the other with the help of roller joint, which moves in an oblong groove of a link, which is attached to the patient's thigh (Figure 23). Depending on the exercise, the roller joint can stay in the end of the groove (the hip exercise) or move along the groove (the knee exercise).

The paper [55] presents the continuation of the work [54] in which a 1 DOF mechanism for lower limb rehabilitation was studied. The kinematics was improved, in comparison with the previous mechanism. The researchers were able to protect the patient from the contact with moving joint parts. However, reconfigurable part of the mechanism is based on the previous concept.

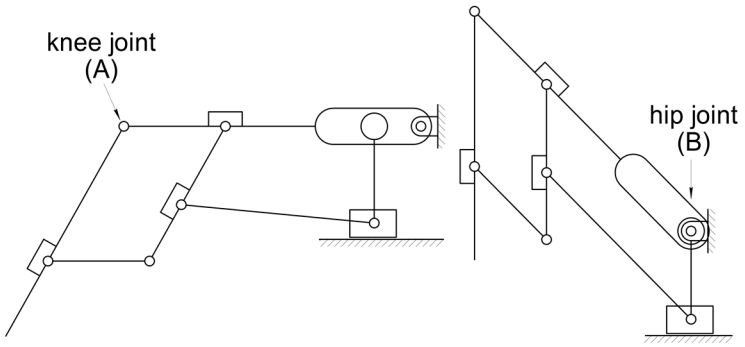

Figure 23. Rehabilitation mechanism in two modes [54]: a) knee-only motion; b) hip-only motion.

A set of variable joints is introduced in [56] (see Figure 24). The authors present a prismatic joint of L-shape, combining functions of two P-joints that are perpendicular with respect to each other. The carriage can travel between the guides, changing the motion direction, when the junction point is passed. Among the other proposed concepts there is a set of joints that combine cam pair and revolute or/and prismatic joint. One design contains a cylindrical revolute part in a uniform groove, and the other consisted of a revolute part with a segment cut and a groove with two different sizes. A revolute joint able to vary the plane of rotation was considered. It was based on spherical joint with the guides for the link. A joint, similar to the one in [53], which combines prismatic and revolute joints, was presented. Identical principle is placed in the design of a special link, which makes the other proposed joint change its type from prismatic to cylindrical. In this design, a cylindrical guide is attached to the flat object, which slides between two planes. When the object slides out of the constraining planes, it gains the rotational DOF and the joint becomes cylindrical.

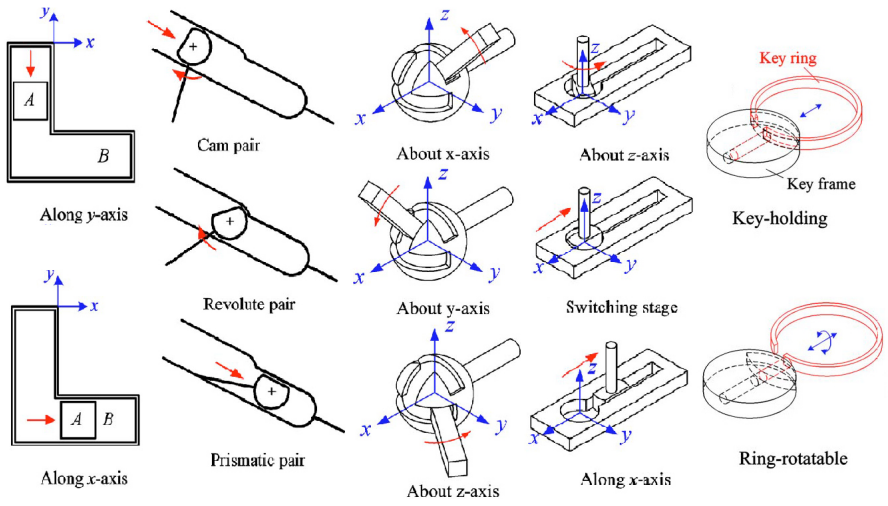

Figure 24. Set of reconfigurable joints proposed in [56].

In the paper [39] three kinematic sub-chains, which can be considered as variable joints are presented. The sub-chains, considered in the study were 4R, RPRP and so-called "diamond kinematotropic chain", which is actually a variant of Pa-joint. The mentioned sub-chains are depicted in Figure 25.

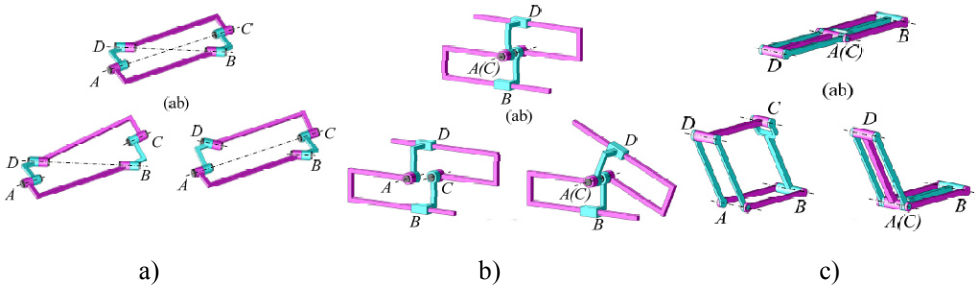

Figure 25. Kinematic sub-chains [39]: a) 4R; b) RPRP; c) "Diamond kinematotropic chain".

In the 4R sub-chain, the opposite pairs of joints can be considered as one joint. RPRP sub-chain acts like revolute joint or prismatic joint, depending on the

position. “Diamond kinematotropic chain” can provide rotational DOF or rotational and translational DOF. Based on these sub-chains, three manipulators were simulated. The manipulators had the sub-chains attached to the fixed platform from one side and to the RRPR leg to the other side. All manipulators had three legs with the triangular moving platform. Depending on the sub-chains’ states, the manipulators were providing 3T motion, 2T1R motion, 2R1T motion and 3R motion types.

In [57] a planar reconfigurable mechanism is considered. The mechanism (see Figure 26a) consists of six bars and a diamond kinematic sub-chain.

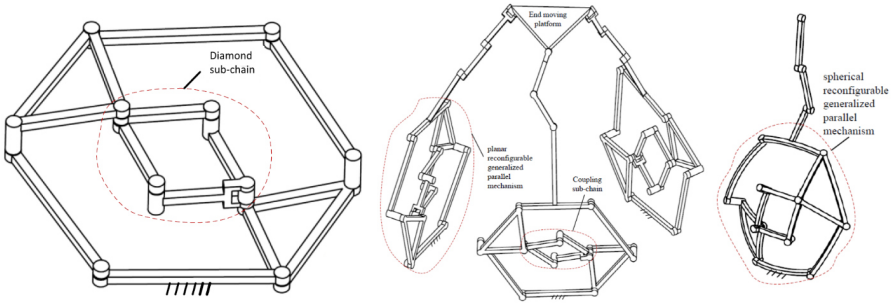

Figure 26. The mechanism with a diamond kinematic sub-chain (a), the manipulator based on it (b) and a spherical mechanism with a diamond kinematic sub-chain (c) [57].

It provides two different configurations: with 1DOF and with 2DOF. The advantage of this kind of parallel mechanism is that it allows to place all the actuators at the base platform, which leads to inertia reduction and the absence of floating weights. The example of the manipulator based on the proposed concept was presented in Figure 26b. Other mechanism proposed in this research is a modification of the previous one, where all the axis of the R-joints intersect

in one point, forming a spherical diamond sub-chain (Figure 26c).

A mechanism with a variable amount of DOF is presented in paper [58]. It consists of eight links, connected by the revolute joints (see Figure 27). Because of the joint axis arrangement, the mechanism can have 4 modes: 2 with 2 DOF and 2 with 3 DOF. The transition from one mode to another takes place through the singularity position.

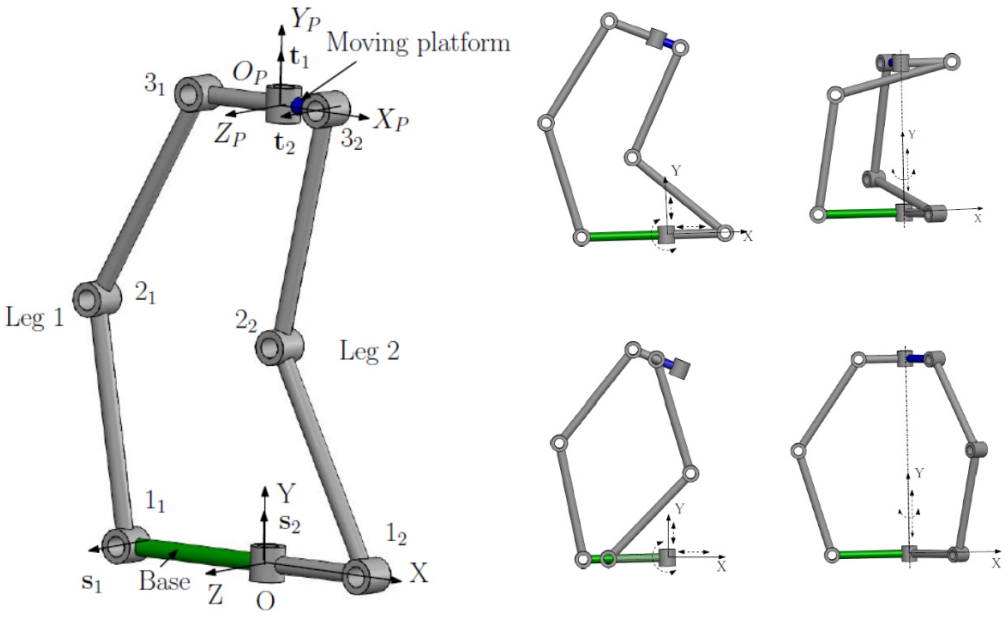

Figure 27. 8R mechanism with variable degrees of freedom [58].

Another novel joint type, called D-CORE [59] is based on two rolling cams, connected with one another with elastic bands. The bands embrace the cam surfaces, and can go from one cam to another, when they are being rolled (see Figure 28).

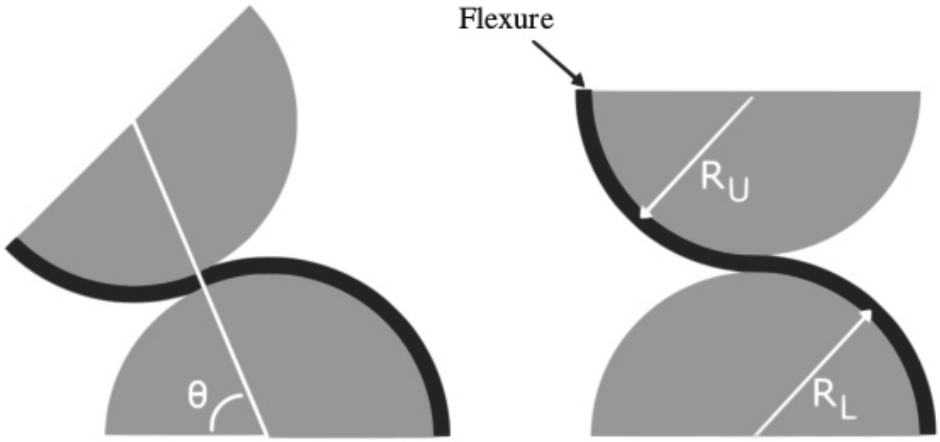

Figure 28. D-CORE joint [59].

The continuation of this work is presented in [60], where a structure similar to D-CORE, used in Jacob's ladder toy, was studied. In addition, a D-CORE origami-inspired design is presented in this study. Based on that design, the translation platform was created for testing the concept. As a particular drawback of this platform, it can be mentioned that the circumference of the joint limits the translation motion. Moreover, the platform is not restrained from the vertical movement, because of the elasticity of the bands.

A novel joint, called Koenigs joint vas introduced by Lee and Hervé [61]. In this work the set of equivalent RC//RC linkages was considered and based on that the prototype of a joint was introduced (see Figure 29). The Koenigs joint can transmit rotation through variable angles, like Cardan joint or constant-velocity joint. However, Koenigs joint can provide larger angle (up to 90 degrees) between the shafts, in comparison to the other joint types.

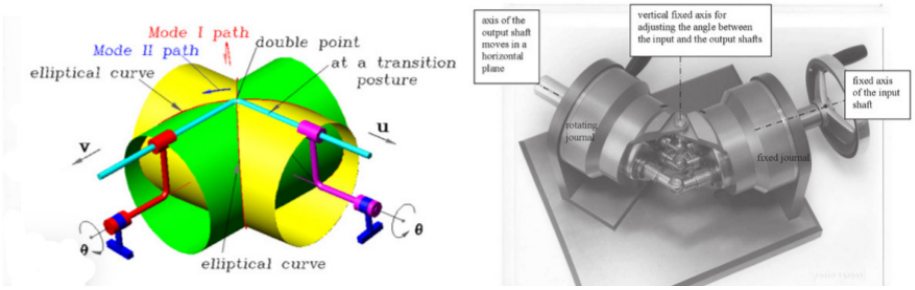

a) b)

Figure 29. Koenigs joint [61]: a) simulation; b) prototype of the joint.

1.1.8. Classification of the reconfiguration approaches and their practical application

Looking at the listed sources, some classification regarding the possible fields of application of these reconfigurable mechanisms can be introduced.

Considering manipulators and platforms, the most widespread robot application is production line [4], [5], [14–16], [18–24], [27], [32], [44], [46–48], [51], [57]. Some features of the reconfigurable manipulators were implemented in mobile robots [6], [16]. Among the other possible applications can be found: after trauma patient rehabilitation mechanism [54], [55], extra-high-voltage (EHV) power line repair robot [9], spherical mechanisms for serial robot wrists or humanoid robot waist joints [26], [27], [43], the mechanism for precise telescope mirror control [28], the adjustable leg for the walking robot [29], the mechanisms than allow to change the compression ratio of the internal combustion engine [30], the wing structure with adjustable aerodynamics [40], the platform for transportation purposes [60], and the joint for the translation of the rotation motion [61].

The significant part of the researchers, which were investigating robots similar to Stewart-Gough platform, used UPS manipulator type [5], [16], [19], [35], [47] or its variation, like PUPS/PSPU [18], [20], [25].

Novel joints as a design feature were introduced in [45–48], [53], [54], [56], [58–60].

1.2. Haptic devices

Haptic devices are mechanisms created for operating the virtual or real objects and that provide tactile feedback of a different kind. The devices have found different applications, including different kinds of surgery [62], [63], mechanism teleoperation [63–65] and operating virtual objects [67] [68].

The devices can have different type of feedback that indicates the interaction with the object, which is being manipulated. Among the most widely used feedbacks are force [67–70], torque [62] and vibration [71–73]. The haptic devices can be specialized [63], [71] or can have a general purpose application [68], [69].

In [70] the haptic devices design guidelines which were formed:

- Force feedback accuracy within the range 0.001 -10 N.
- The device should be at least 3 times stronger than the maximum possible force applied to it.
- There should not be any structural elements within the workspace, which can interfere with the operation.
- The inertia forces should be small and uniform within the workspace.

- The clearances and friction forces should be made as small as possible.
- The frequency response should be equal or exceed 300 Hz, according to the human perception abilities.

These guidelines are oriented on making haptic devices more “realistic” for the human operator and on increasing their work efficiency.

1.2.1. Haptic devices based on parallel mechanisms

A design of a 7 DOF haptic device was presented in [70]. In this work, the author reviews the existing designs of haptic devices, analyzing their advantages and disadvantages. As a result, a complex hybrid serial-parallel haptic device was proposed (see Figure 30). The mechanism contains five closed loops and utilizes revolute and universal joints. The actuators and the sensors of the device are fixed in its base in order to decrease the inertia. The mechanism is actuated with the cables.

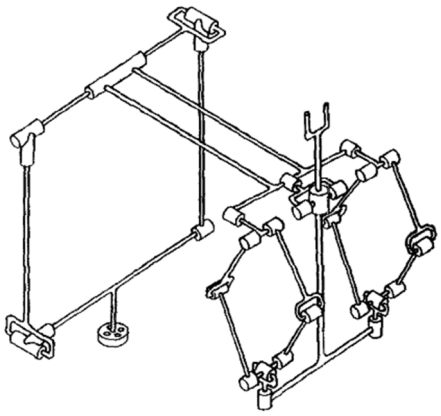

Figure 30. A 7 DOF haptic device [70].

A haptic device, called µHaptic (see Figure 31) for microsurgery was designed and built by Salisbury Robotics [71]. The device has 6 DOF and provides the force feedback of maximum 5 N in every direction. The main goal of the researchers was to decrease the inertia of the mechanism. For this purpose the low inertia motors were utilized. In addition, the links of the haptic device are cable driven, which allowed removing heavy actuators from the moving parts of the mechanism. The haptic device has a spherical workspace of 75 mm in diameter.

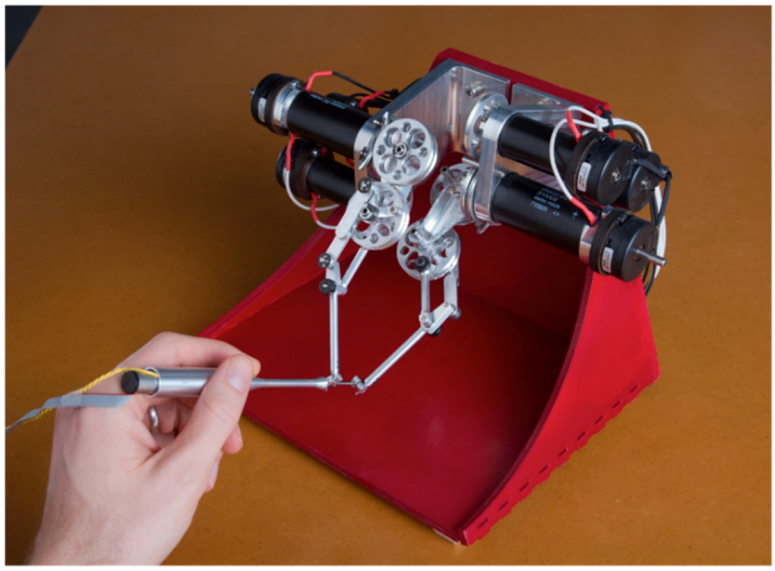

Figure 31. µHaptic device for microsurgery [71].

The design of the 6 DOF 6-PSU parallel mechanism based haptic device was proposed in research [62] (see Figure 32). The objective of the researchers was to make a mechanism with the high stiffness that provides force and torque feedback and would be “transparent” in its operation. Transparency in this case means that the operator should feel the feedback of the system as close to the

real world work as possible. The device was built using a variant of the kinematic structure proposed in [75] with active prismatic joints, actuated by the DC motors through the cables. The control system computes the necessary torque of the DC motors in order to provide the force feedback of the system. The system worked with the frequency of 1kHz. The experimental results revealed that the system needs inertia compensation.

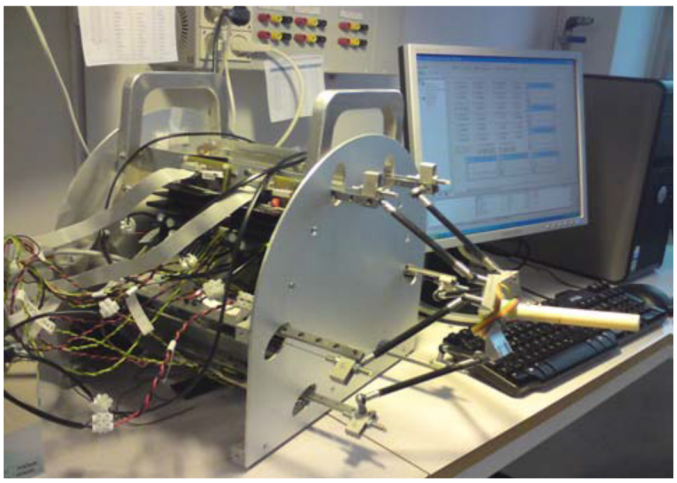

Figure 32. A 6 DOF parallel mechanism based haptic device [62].

A 6 DOF haptic device, based on the orthoglide and a hybrid agile eye was proposed in [76]. This design has three linear actuators and two revolute actuators, which are fixed to the base in order to decrease the inertia forces. The torque from the revolute actuators is transmitted through the shafts, which come to the agile eye part of the mechanism (see Figure 33). This part has a third revolute actuator, responsible for rolling. The goal of the research was to design the haptic device with the increased stiffness and low inertia in order to make the operation closer to the real world work.

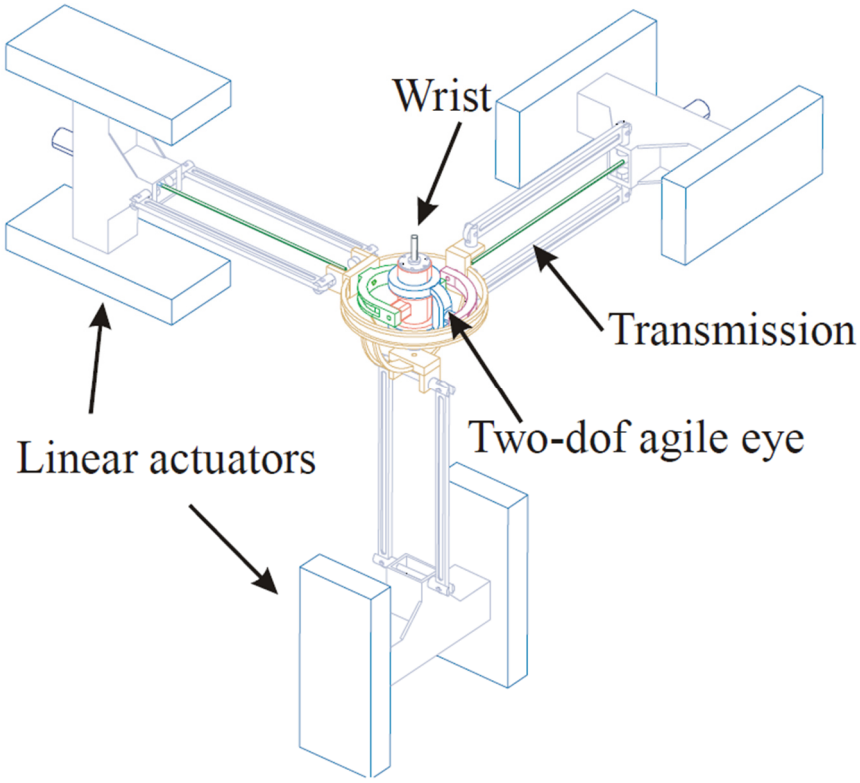

Figure 33. A 6 DOF haptic device, based on the Orthoglide and a hybrid agile eye [76].

Novint Technologies Inc. manufactures 3 DOF haptic device, called Falcon (see Figure 34) [77], which is often used as a game controller. The device has an architecture of a delta robot and has three revolute actuators in order to provide force feedback with operating frequency of 1000 Hz. The workspace of the device is 10 cm x 10 cm x 10 cm, where the translational motion can be executed. The main application of the device is virtual object manipulation and gaming, but it also can be used in medicine, for example as a cheap surgery simulator [78].

Figure 34. Novint Falcon [77].

1.2.2. Other types of haptic devices

Haptic master device (see Figure 35), based on a spherical joint was presented in the paper [63]. The device has three rotational degrees of freedom and one translational. The central part of the spherical joint is filled with the electrorheological fluid, which provides the force feedback from the slave device. The slave device is a mechanism, which is being controlled by a haptic device. In this case, the system was designed to control a surgical robot.

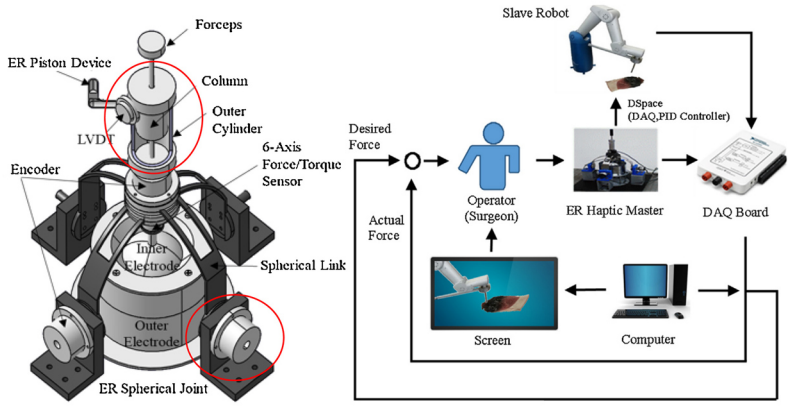

Figure 35. Haptic master device and the control plan [63].

A haptic device utilizing magnetorheological brake was presented in paper [79]. This device constitutes a passive joystick, which is used to control the virtual electrohydraulic drive. The joystick (see Figure 36) is equipped with the force sensor, the potentiometer as a position sensor and the magnetorheological brake, which creates the resistance to the force applied by the operator.

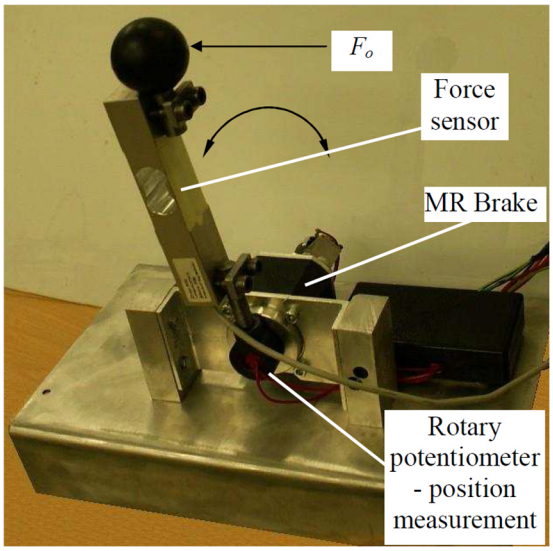

Figure 36. Joystick with magnetorheological brake [79].

A tension-based haptic device, called SPIDAR-G (see Figure 37), was presented in [80]. The device has simple structure and fast feedback due to low inertia. It provides 7 DOF (6 DOF + grabbing) and is easily scalable. The disadvantage of the structure is the necessity in the big cubic shaped base frame (see Figure 37), to which the main elements of the system are mounted. Because of this feature, the device is harder to transport than the devices with serial architecture. It is more suitable for stationary applications than for mobile ones.

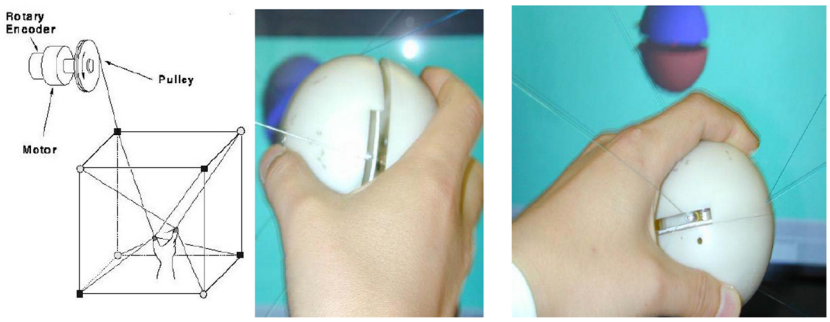

Figure 37. SPIDAR-G: a tension-based haptic device [80].

Other types of haptic devices follow a serial chain. The 3D SYSTEMS Company manufactures three types of serial haptic devices: Phantom Touch [68], Phantom X and Phantom Premium [69] (see Figure 38). These devices have similar URRU serial architecture, which provides 6 DOF and force feedback from 3.3 to 37.5 N, depending on the model. Although the devices are general purpose, the Touch device family specializes more in the virtual object operation and the Phantom Premium is positioned as a device for teleoperation and simulations.

a) b)

Figure 38. Commercially available haptic devices: a) Phantom Touch [68]; b) Phantom Premium [69].

A wearable haptic device with vibration and skin deformation feedback was presented in [72]. The haptic device is located on the operator's finger. The device contains a voice coil motor to maintain the contact with the finger, and two motors, which pull the belt that deforms the skin (see Figure 39). The revolute motor shafts are connected to the potentiometers, in order to receive the position feedback. The device can represent vertical displacement, surface collision and vibration. The disadvantage of this system is the size and weight of the device, which could create discomfort for the operator after long use and produces considerable inertia forces that make control process more complex.

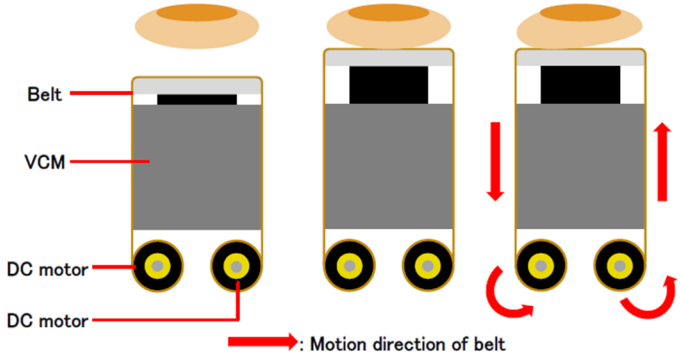

Figure 39. Skin deformation principle of a wearable haptic device [72].

A family of wearable haptic devices with vibration feedback is manufactured by CyberGlove Systems. The company produces gloves for working with three-dimensional virtual objects. The models CyberTouch [73] and CyberTouch II [74] are equipped with 18 positioning sensors [81] and lightweight vibrotactile stimulators in the ends of the fingers of the glove. The company also manufactures models CyberGrasp [82] and CyberForce [83], which provide force feedback and can be used in telerobotic applications and exoskeletons.

1.2. Parallel manipulator market analysis

To be able to identify the most used joint types, the parallel manipulators, which are available in the market, should be considered. The report on global parallel robot market made by Technavio market research company [84], states that the key manufacturers in the field of parallel manipulators are: ABB, Codian Robotics, FANUC, and OMRON. Also, other prominent vendors as Kawasaki Heavy Industries, Penta Robotics, Mitsubishi Electric, were mentioned. Aside from the companies listed in Technavio report, there are other vendors, which sell parallel manipulators, such as Symetrie, Gridbots, Yaskawa, GSK, PICVISA, Panasonic, Bosch, BFR Systems, Sipro Engineering, Schobertechnologies, MGS, TOSY Robotics, Igus, SSI SCHÄFER, Hugo Beck, Schmid, and Grandi.

The information listed on the websites and in the brochures and catalogs of these companies was used to identify the most used joints in commercially available parallel manipulators. According to the available information, the most used types of the joints are ball joints, universal joints, revolute joints parallelogram joints and prismatic joints. The majority of the manipulators are implementing Delta robot design. Delta robots are being manufactured by ABB, Codian Robotics, FANUC, OMRON, Kawasaki Heavy Industries, Penta Robotics, Mitsubishi Electric, Gridbots, Yaskawa, GSK, PICVISA, Panasonic, Bosch, BFR Systems, Sipro Engineering, Schobertechnologies, MGS, TOSY Robotics, Igus, SSI SCHÄFER, Hugo Beck, Schmid, and Grandi. The examples of the delta robots can be seen in Figure 40.

a) b) c)

Figure 40. Delta robots: a) ABB IRB 360 [85]; b) FANUC M-1 series [86]; OMRON Quattro [87].

The second most widespread robot type is a Stewart-Gough platform. However, the number of companies proposing this kind of manipulators is much smaller: FANUC, Symetrie and Gridbots (see Figure 41).

a) b) c)

Figure 41. Stewart-Gough platforms: a) FANUC F-200iB robot [88]; b) Symetrie BREVA [89]; c) Gridbots Hexamove [90].

There were found only two commercially available models of SCARA-type parallel manipulators (see Figure 42), one of them has cylindrical joint in its

design.

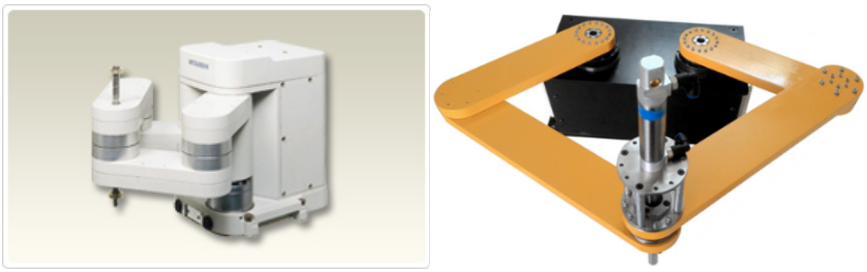

a) b)

Figure 42. SCARA-type parallel manipulators: a) Mitsubishi Electric High precision SCARA parallel robot [91]; Gridbots RAPI-MOV [92].

In a Delta robot manipulator type, most of the joints are typically spherical as there are four of these joints per one robot limb. In the Stewart-Gough platform, depending on the limb structure can be one spherical joint per one robot limb. All the spherical and universal joints that can be seen in the commercially available designs are passive. In general, the designs of the reviewed manipulators are quite conservative without any reconfiguration possibilities. It can be explained from one side with the unwillingness of the big robot manufacturers to take financial risks of releasing a completely new robot type, which might not recoup the development costs. From the other side it can be explained with the lack of the design solutions, which would provide the advantages that will overcome the mentioned risks. The second assumption pushes the researchers and designers towards the development of more perfect and more reliable reconfiguration strategies and manipulator designs.

1.3. Active spherical joints and mechanisms

In this section, the designs related to spherical mechanisms, ball joints and spherical-like joints that have been investigated and/or patented in the last years will be presented.

Spherical robotic wrist (see Figure 43) is proposed in the patent [93]. This joint's design is similar to the design of the master haptic device with electrorheological fluid force feedback, which was proposed in [63]. As it can be seen from Figure 43, the joint has two actuators, which provide two rotational DOF-s.

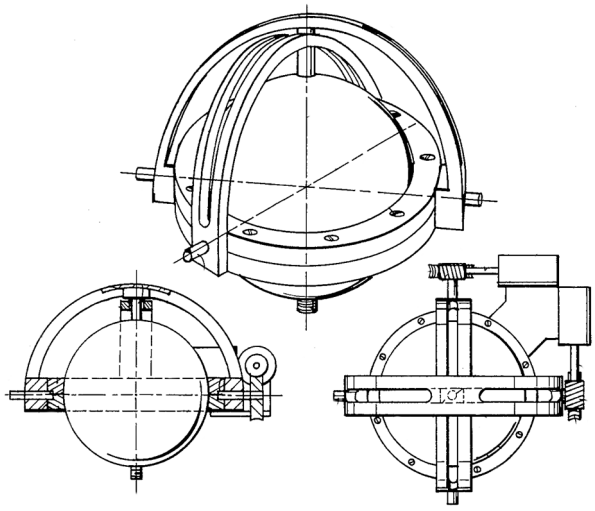

Figure 43. Spherical robotic wrist [93].

An almost spherical parallel mechanism, called ACTIVE ANKLE (see Figure 44) is presented in the paper [94]. The mechanism has three motors, each of which is connected to the end-effector with the 4S 4-bar linkage. It was designed for ankle joints in endoskeletons or other applications where big workspace is not required.

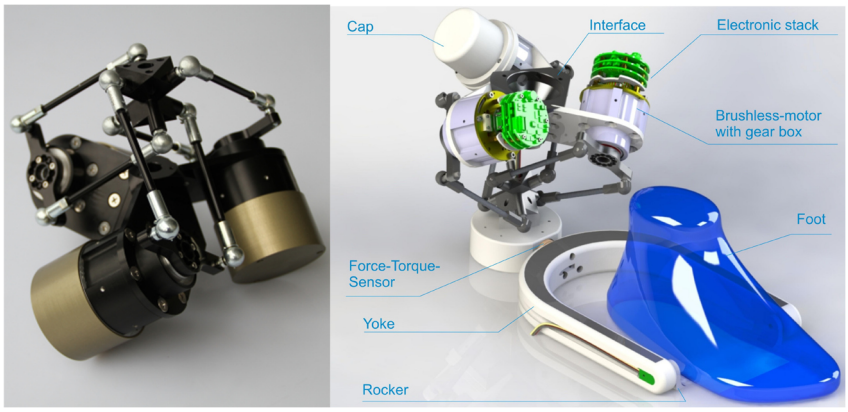

Figure 44. The prototype of the ACTIVE ANKLE [94].

A spherical parallel mini platform (see Figure 45) was described in [95]. The purpose of the platform is orienting the small and lightweight (30-100 g) parts in space. The platform corresponds to a spherical 5-bar mechanism and provides 2 DOF motion.

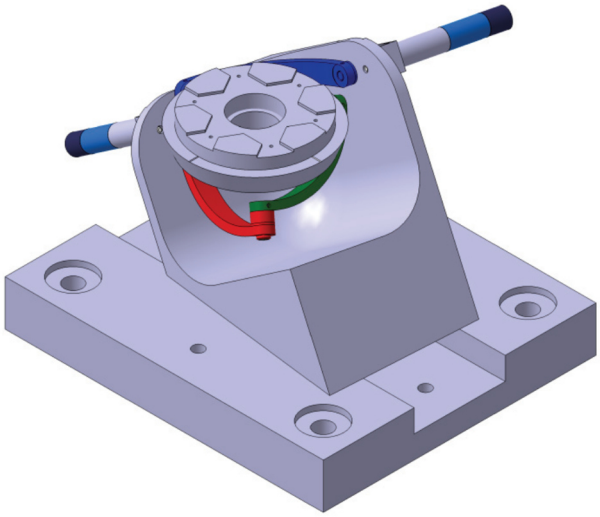

Figure 45. Spherical parallel mini platform [95].

Another possible application of the spherical mechanism is a tool head for complicated surface machining, as the one presented in [96]. The asymmetrical spherical parallel mechanism (see Figure 46), proposed in the paper, consists of two RRR legs, which orient the outer ring of the end-effector platform, and the actuated central shaft, which rotates the inner ring of the platform with the help of cardan joint. The inner and outer rings of the platform are connected with the ball bearing.

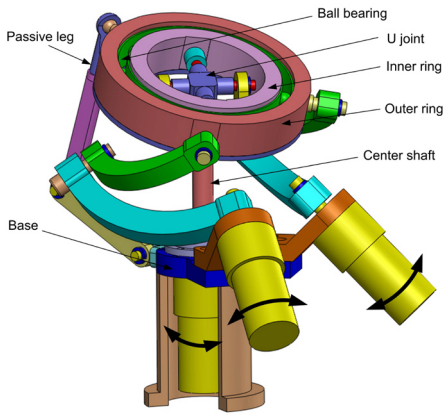

Figure 46. The asymmetrical spherical parallel mechanism [96].

A spherical joint for a prosthetic ankle (see Figure 47) was presented in [97]. The actuation principle was inspired by the ball-mouse coordinate reading mechanism. Two shafts with special pinions, rotate the sphere which has round openings for the connection with the pinions' teeth. When one pinion is locked in certain position, where its tooth is placed inside the sphere's opening, it forms the axis of rotation, around which the other pinion can rotate the sphere. This feature limits the amount of possible positions provided by the joint, as it is impossible to make infinite number of openings in the sphere.

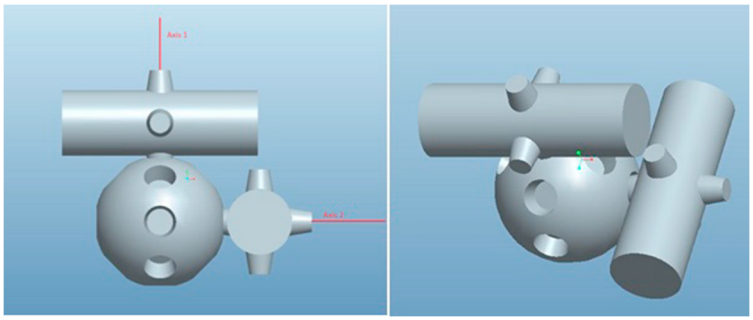

Figure 47. A spherical joint for the prosthetic ankle [97].

A similar actuation principle can be found in the patent [98], describing spherical gear. This 2DOF joint has a spherical surface covered with pyramidal shape teeth (see Figure 48). The joint can be actuated with two pinions, each of which controls 1 DOF of the joint. A cardan joint is placed in the center of rotation of the joint, allowing the spherical surface to move. It can be noted that the spherical gear is hard to manufacture. In addition, the strength the cardan joint and the teeth of the spherical gear limit the load capacity of the joint.

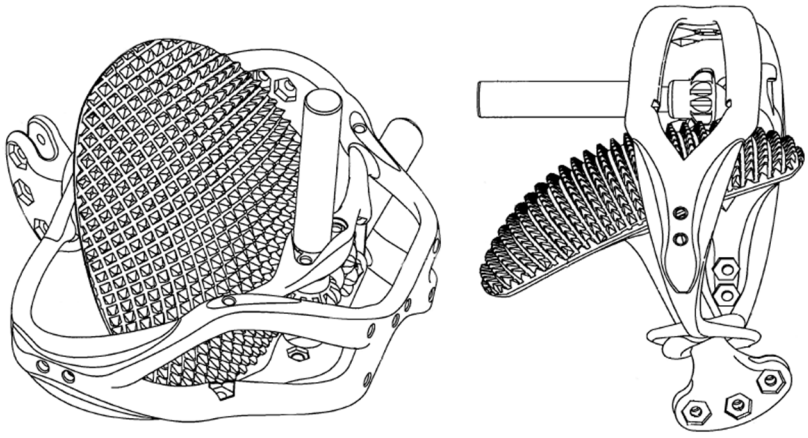

Figure 48. Spherical gear [98].

Geared approach of actuation for spherical-like joints can be also seen in the patent [99], which describes a robotic shoulder joint (see Figure 49). This joint utilizes three actuators, which control 2 DOF-s of the joint. The actuators are able to incline during the actuation process, in order to keep their pinions in contact with the geared sphere. It can be assumed that movable actuators will create significant inertia forces in this joint. The design, proposed in the patent does not present any support for the sphere other than the base plate, which limits the load capacity. In addition, no approach for compensation of the clearance in the gear was proposed.

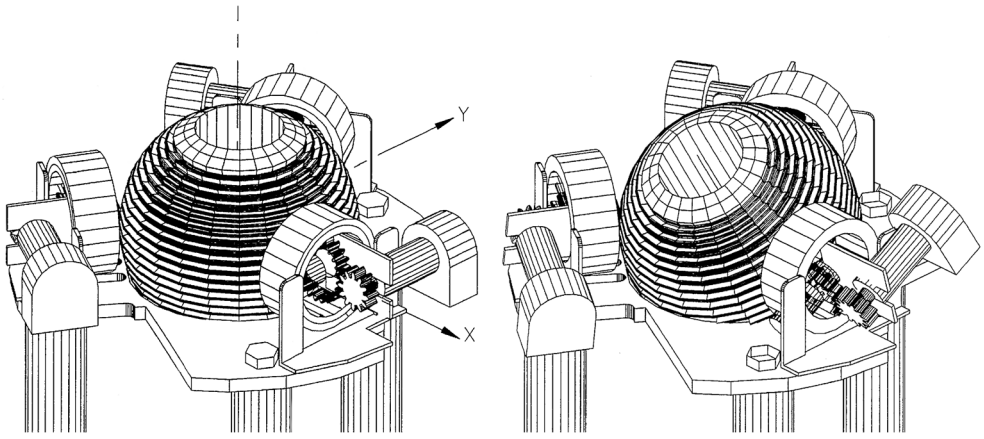

Figure 49. Spherical robotic shoulder joint [99].

A spherical active joint for the humanoid robots is proposed in [100]. In this joint, the motor shafts are attached directly to the central ball (see Figure 50), which is surrounded with three curved sliders, on which the motors are mounted. Thus, the actuators are in motion during the actuation process.

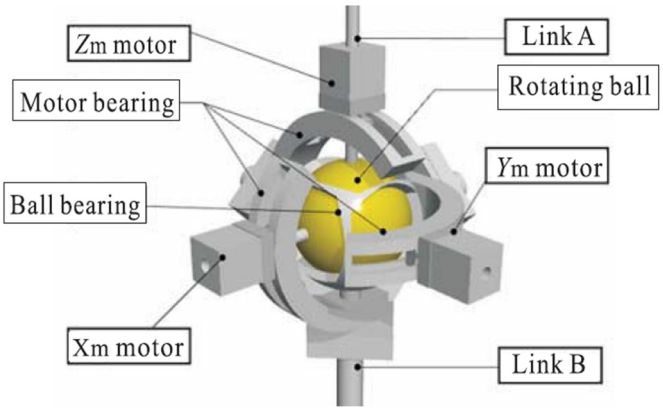

Figure 50. A spherical active joint for the humanoid robots [100].

A spherical stepper motor-like active joint (see Figure 51) was described in [101]. The spherical part of the joint incorporates strong magnets, which interact with the electrical magnets of the stator part of the joint. Magnetic suspension is used in the joint to eliminate friction and wear. The joint is equipped with 4 clamping devices, whose original purpose is to prevent the sphere from contacting with the stator.

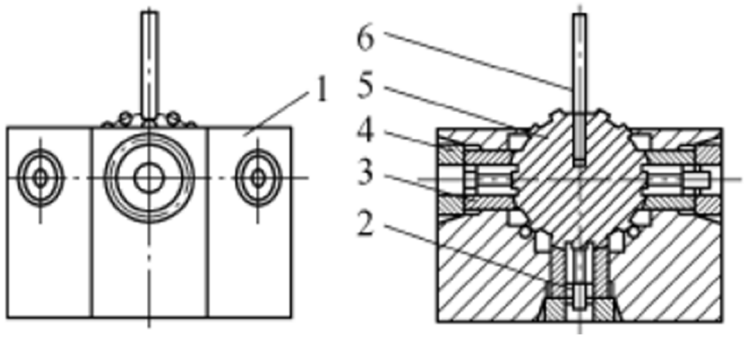

a) b)

Figure 51. A spherical stepper motor-like joint: a) joint appearance; b) stator-rotor structure [101].

An active ball joint called ABENICS was proposed in [102]. The prototype of the joint is presented in Figure 52. In comparison to the similar designs ([98] and [99]) this joint has 3 DOF with the actuators fixed on the joint's frame. The actuator arrangement allows reducing of the inertia forces; however, four actuators are necessary due to the joint kinematics. In addition, the ABENIX joint cannot provide big load capacity because of the small contact area between the central sphere and the base of the joint.

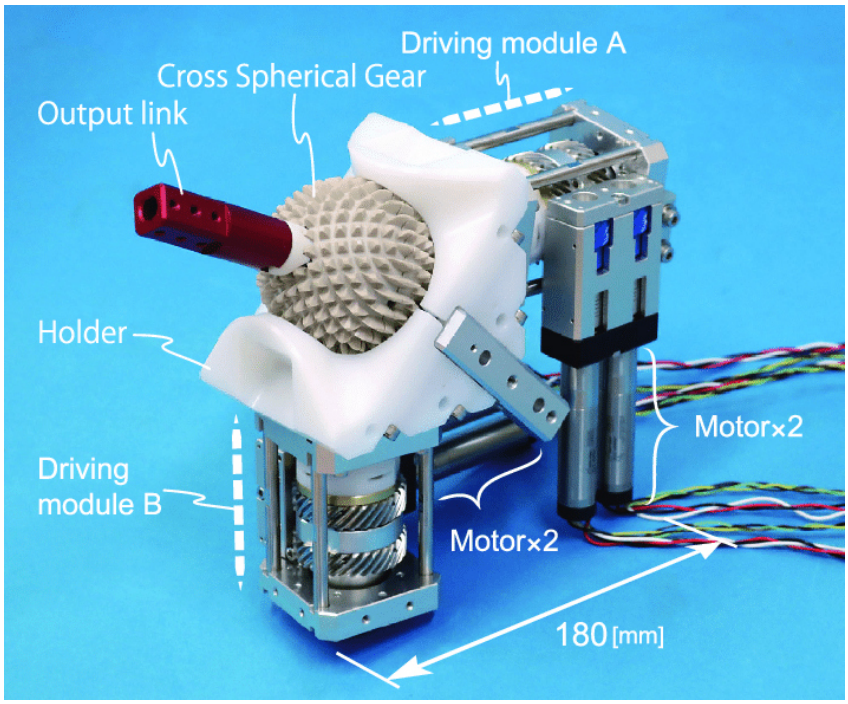

Figure 52. A prototype of ABENICS [102].

2. Comparative study of different joint design proposals

2.1. Introduction

In the previous sections, various reconfiguration methods were analyzed. The methods that implement special joints seem to lack the reliable solution for the reconfigurable spherical joint. The market analysis has also demonstrated the absence of reconfigurable joints in the commercially available robots, although the conventional spherical joint is one of the most used. This fact proves that the reconfigurable spherical joint design that would be suitable for the real world applications does not exist yet.

The goal of this chapter is to present the joint designs that extend the capacity of the conventional spherical joints. The characteristics and features of the designs will be presented and compared. Among the compared parameters are complexity, load capacity, dimensions, inertia, accuracy, functionality and reachable workspace area. To estimate the complexity several parameters can be considered: number of parts, manufacturing complexity, or assembly complexity. Load capacity can be divided into passive and active. Passive load capacity can be estimated for the joints, which are not actuated or the parts of active joints, which do not take part in joint actuation. Active load capacity can be estimated for the actuated joints. It will depend on the parameters of the parts, which participate in the actuation process. Both types of load capacity are defined by the geometry of the joint components. The most important are the shape of the parts and their contact surface areas. These parameters will influence the load distribution in the joint. If the joint design is similar to the ball

joint, the percent of the central sphere area that is in contact with the base can be compared with the conventional ball joint, where it can be up to 75%. The overall dimensions of the joint are measured by the base, as it is normally the biggest part in the design. The dimensions of the biggest moving part in the joint can roughly assess inertia parameters. The accuracy of the joint is influenced by the clearances and backlashes between the parts and the possibility of their compensation. Functionality refers to the ability of performing certain operations. The bigger the amount of functions and modes the joint can implement, the wider is its possible application field, thus, enhancing the functionality indicator. As the presented joint designs are spherical or universal, the shape of their workspaces is spherical, the reachable workspace being a certain part of the whole sphere. Only practical workspace will be considered in this section. It will be calculated as the percentage of the complete sphere, which is taken as an ideal workspace.

The comparison and assessment of the proposed designs will be presented in section 2.3.

2.2. Proposed designs of reconfigurable joints

2.2.1. Design 1: Lockable passive joints

At first, the idea of a passive lockable joint was born (see Figure 53). This design was partially inspired by the constant-velocity joints, which are widely used in front driven automobiles. Unlike the constant-velocity joint, in the proposed design the balls serve to lock the DOFs of the central sphere. As it can be seen in Figure 53, the joints have similar design, except the shape of the locking

elements of the central sphere. One of the spheres has cavities 1, and another one has grooves 2. The difference between these locking elements is how many DOF can be locked with one ball. The locking takes place when one ball 3 is pushed through the cylindrical opening of the base part 4 towards the central sphere. It can be done using the linear actuator or manually, for instance with the screw. To be able to lock the joint, it is necessary for the locking element of the central sphere to be positioned next to the outlet of the opening, through which the ball is moving. When the first ball is pressed to the locking element of the sphere, in case of the sphere with cavities, 2 DOFs of the joint become locked.

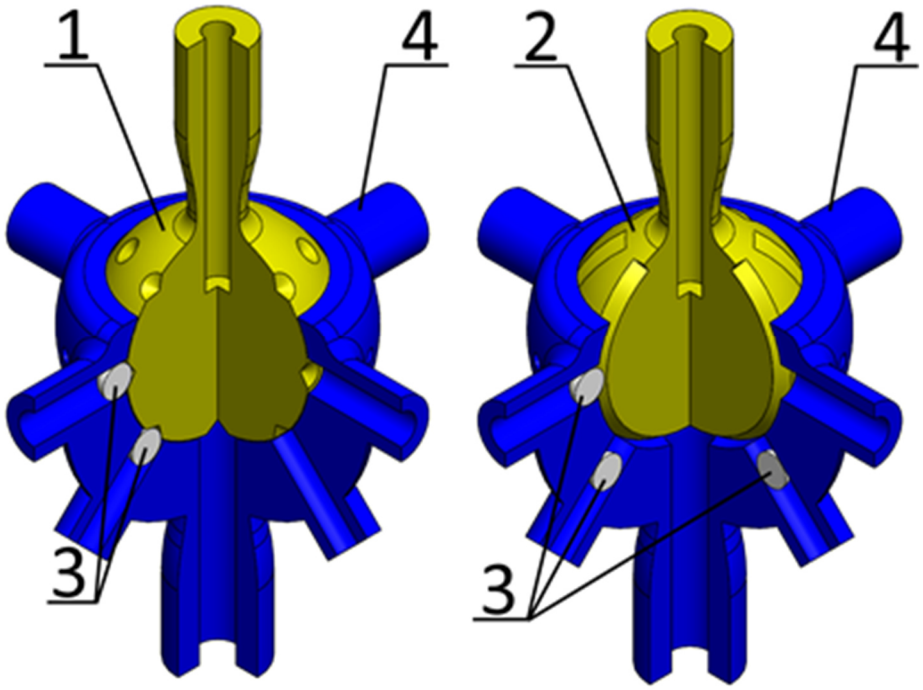

a) b)

Figure 53. Lockable passive joints: central sphere with cavities (a) and with grooves (b).

The joint can provide rotation around the axis that goes through the center of the central sphere and the center of the ball. The second ball, pressed through any other opening of the base part (except the opposite one to the first) will lock this joint completely. In case of the sphere with the grooves, the first ball locks only one DOF, which is the rotation of the central sphere around the axis of the output rod of the joint. The second ball locks one more DOF, making possible only the one rotation. The joint now can rotate around the axis, which goes through the center of the sphere and is perpendicular to the plane in which the groove lays. The third ball locks the joint completely.

As for achieving a successful locking, it is necessary for the locking element and the ball's opening outlet to coincide. It is clear that the joint has only several discrete positions in which it can be locked. This disadvantage cannot be eliminated in this design, because increasing the amount of the locking elements will decrease the contact surface between central sphere and the base part. In addition, the material characteristics of the parts will limit the minimum size of the locking elements and the balls. The maximum angle of the rod deflection for the both joints is $\pm 45°$, which constitutes 14.64% of the sphere. Although, this design was not adapted for conventional manufacturing, it is easy to build, as its elements do not have many distinctions from the parts of the conventional ball joint. The clearance compensation can also be implemented in these designs by incorporating the adjustable top ring with the pads under it. This top ring on one hand will hold the central sphere in its place, and on the other hand, it will allow clearance adjustment by regulating the thickness of the pad under the top ring. As the overall dimensions of the joints are small, the inertia forces affecting them will be insignificant. The load capacity of these joints is smaller, compared to the convention ball joints. For the design with the groves, the central ball has

44.02% of the area in contact with the base. For the design with cavities, it is 67.4%. The complexity of the control will depend on the mechanism where the joints will be applied, as they are passive and the output rod position is dependent. The joints are suitable for the applications in reconfigurable parallel mechanisms similar to the ones presented in [46-50].

2.2.2. Design 2: Active spherical joint with prismatic and revolute actuation

Locking the spherical joint at any desirable position, is possible if an active joint is used. In this case, the joint can be locked by blocking its actuators when selective actuation method is applied.

This idea led to the development of the first active spherical joint design concept, which can be seen in Figure 54. In this design, two rotational DOFs of the joint are actuated with the prismatic active joints. The third actuator is revolute; it rotates the constant velocity joint (in green and purple in the Figure 54) around the vertical axis. This constant velocity joint transmits the rotation to the joint's rod, making it rotating around its longitudinal axis. The linear actuators transmit the motion through two spherical joints. The lower joint (in yellow) also allows the rod (in purple) to move along its axis inside the sphere, which forms additional cylindrical joint. This movement is necessary for the compensation of the variating distance between the centers of the yellow and purple spheres, during the actuation of prismatic joints. The blue part of the joint is also necessary to allow the rod's movement. When the rod is close to vertical position, its end goes out of the yellow spherical joint.

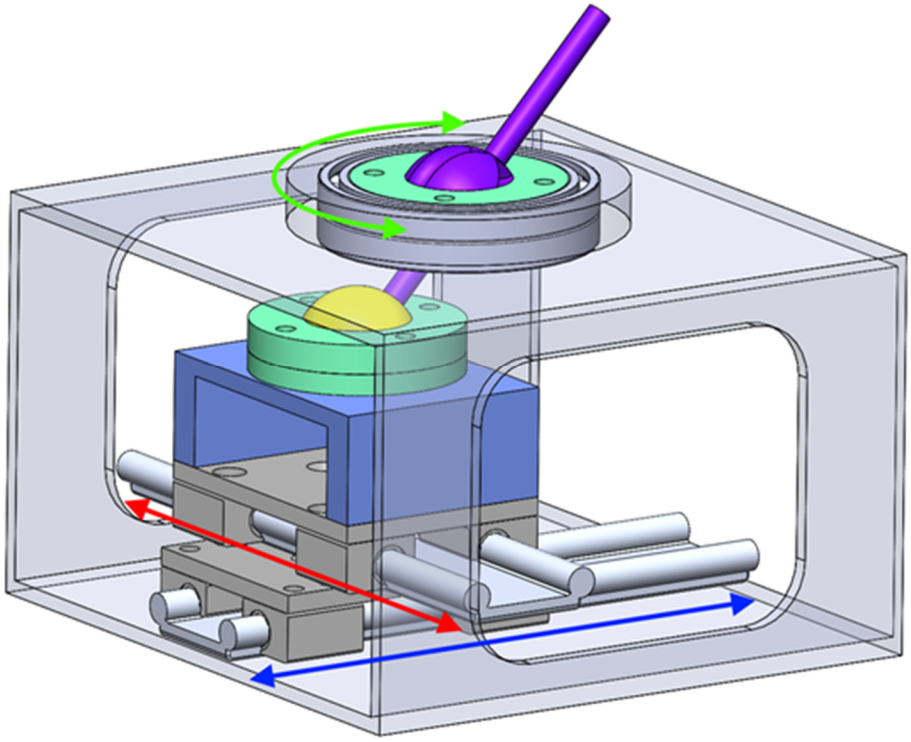

Figure 54. Active spherical joint with prismatic and revolute actuators.

This joint design allows locking at any position, limited only by the actuator resolution. The kinematics of this joint is simple. The location of the yellow ball joint center with respect to the purple ball joint center of the joint can be directly translated into the deflection angles of the output rod. In addition, the revolute actuator provides direct rotation of the rod around its longitudinal axis. The maximum deflection angle of the rod is $\pm 49°$ in any direction. This provides the workspace, constituting 17.2% of the sphere. The dimensions of the top spherical joint limit the passive load capacity of this joint design. The central sphere of that joint has small contact area (from 29.12% to 34.11% of the sphere, depending on the rod orientation). Active load capacity, on the contrary, will be

satisfactory due to big cross section of the main parts that transmit forces and torques. The joint is easy to manufacture and assembly, it consists of the parts that can be found in commonly used mechanisms. The clearance compensation is also possible to implement in this design. However, there are several disadvantages, which can limit its application. It would be really complex to make this joint small enough to be able to apply it in most of the manipulators, which have conventional spherical joints. In addition, as a consequence of its big dimensions, the inertia forces in the joint will be high. The joint contains large number of parts, which raises its price. In addition, the rotation of the rod around its longitudinal axis is not necessary for most of the applications, which causes overcomplicating of the design.

2.2.3. Design 3: Active 2R spherical mechanism-based joint 1st concept

Taking into account the disadvantages of the previous design, it was decided to reject this type of design, and something similar to the first proposed design was rethought, but with several improvements. Then, the new joint concept, presented in Figure 55, was born. In this joint, the central sphere with the grooves from a passive lockable joint (2 in Figure 53) was taken as a base. In this concept, the balls 6, which are placed in the grooves of the central sphere 1, serve to transmit rotation from the input cranks 2-5. Each pair of cranks (red and blue) controls one DOF of the joint. This joint has only two DOFs, as the rotation around the rod's longitudinal axis is impossible. The cranks in their pairs are redundant, but are useful for a better distribution of the load. In addition, red pair of cranks serves as a support for the central sphere.

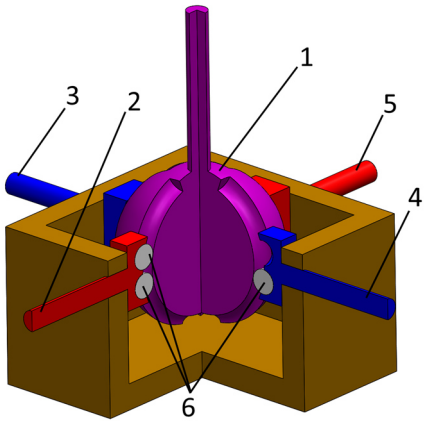

Figure 55. Active 2R spherical mechanism-based joint 1st concept.

As it can be seen in the Figure 55, the joint's design is much simpler than the previous one. The number of components of this joint is smaller. It makes the manufacturing and assembly simpler and cheaper. The general dimensions of this design are much smaller, which makes its possible application wider. The size of the joint also provides small inertia forces in it. The workspace of the joint constitutes 28.9% of the sphere. It is more than in the previous designs because this design provides bigger inclination angles of the output rod. Depending on the position, the maximum inclination angles can constitute from $\pm 58°$ to $\pm 75°$. Nonetheless, the joint's central sphere has insufficient support, being carried only by the red cranks. The balls, which connect the input cranks with central sphere, have very small contact area with their grooves. It leads to increase of the stress, which acts in that area and can cause plastic deformation of the material if the load on the joint will be too high. It also limits passive and active load capacity of the joint. In this joint design, the clearance compensation is possible by creating the pretension in the sliding surfaces by the means of proper actuation. However, this feature will require four actuators to implement

it. In addition, the clearance compensation will work only for the actuated joint, as there is no mechanism of providing it in a passive mode.

Simultaneous actuation of both DOF-s allows using the proposed joint in selective actuation reconfiguration method. The red actuators can relocate the axis of one of the revolute pairs of the joint and lock it in a proper position. Similar principles can be seen in rT-joint [46] and rR joint [48], but the rotation planes in these joints are different, which makes it impossible to apply the proposed joint in the same way as rT or rR joint.

2.2.4. Design 4: Active 2R spherical mechanism-based joint 2nd concept

Considering advantages and disadvantages of the previous design concepts, the new joint design was proposed (see Figure 56). This design is based on the previous joint. The main drawbacks of the previous concept were eliminated by modification of all the main parts of the joint. In order to provide a sufficient support for the central sphere, the base part was extended and provided with a concave spherical surface. The grooves of the central sphere became rectangular in cross section. The connection balls were eliminated from the design. Instead of them, the red cranks were given big contact surfaces, which stay connected with the proper groove of the central sphere. In case of the blue cranks, the balls were replaced with an intermediate connection links, which also have much bigger contact area in comparison to the balls. These improvements ensured the reliability of the design along with the increased load capacity.

As it can be seen from the Figure 55, the joint consists of a base with a top ring, which contain the cranks 2 and 3, and provide support to the central sphere 1. The joint provides two rotational DOFs, which can be controlled with the proper

pair of cranks. The cranks form two rotary pairs with the grooves of the central sphere. The red cranks 2 are connected directly to the sphere 1, and the blue cranks 3 are coupled with it through the intermediate links 4. Despite the possibility of complete control of the mechanism with only one of each pair of cranks, the duplicating cranks were left to improve the stress distribution in the joint. Moreover, the redundancy of the blue cranks helps keeping the joint under control, when the singularity position takes place (see Section 3.1.2.1). The actuation of the red cranks is completely symmetrical and the difference is only the direction, nevertheless, the blue crank control is more complex as the relation between their displacement is not linear. This relation will be described in detail in Section 3.1.1.3.

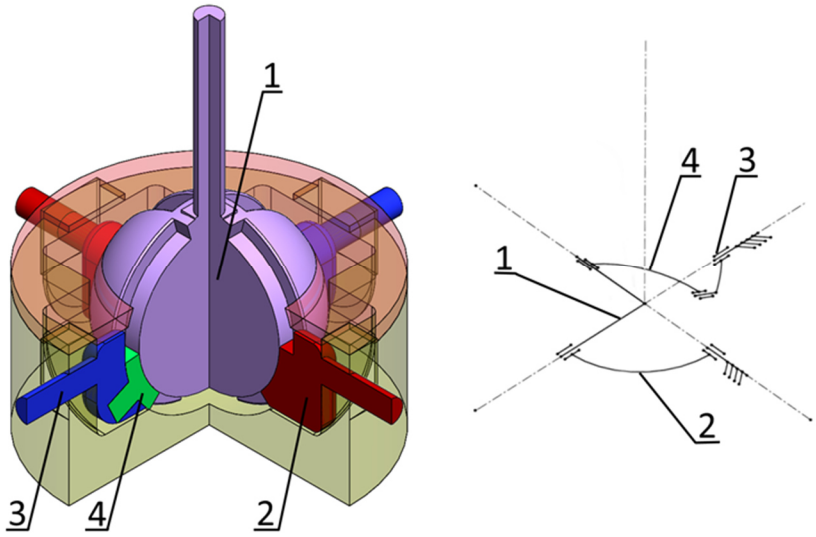

a) b)

Figure 56. Active 2R spherical mechanism-based joint 2nd concept: joint (a) and its kinematic scheme (b).

Considering the proposed joint from the kinematical point of view, it can be seen

that it corresponds to a spherical five-link mechanism [95,103]. Its kinematic representation can be seen in Figure 56b.

The proposed joint provides concurrent actuation of two DOFs, with the ability of locking in the desirable position. Similar to the design 3, this makes possible relocation of the axis of one of the rotary pairs, which form the joint. It allows application of this joint in reconfigurable solutions. The maximum angle of the output rod deflection is $\pm 55°$ in any direction that provides the workspace constituting 21.32% of the sphere. The joint has small amount of parts, which simplifies manufacturing and assembly. The central ball stays in contact with the base and the top ring with the area constituting 18.66% of the sphere. Though it is four times less than a conventional ball joint, it is an improvement compared to the previous design. The joint is compact and simple from the manufacturing point of view. The assembly of the joint is also easy. These qualities make it potentially cheap in production. Small dimensions of the main moving parts also decrease the inertia forces in the joint. As in the previous design, the clearance compensation with the pretension is possible. However, in this design, the clearance compensation for the passive applications also can be partially implemented. The position of the top ring can be adjusted by using pads in order to compensate the wear between the spherical surfaces of the joint. Nevertheless, the clearances between the grooves of the central ball and the cranks cannot be easily compensated in the passive mode.

The main disadvantages of this design are the load capacity, being much smaller than the conventional ball joint of the same size, and the necessity of three actuators to control 2 DOF, or four actuators in order to implement clearance compensation in active mode.

2.2.5. Design 5: Crankless design 1st concept

The main goals for the next design was reducing the number of actuators, increasing the workspace and the contact area between the central ball and the base. In addition, the elimination of the sliding contacts as much as possible could reduce the friction forces in the joint.

The design, which satisfies these requirements, is presented in Figure 57. In this joint, the sliding pairs of the input cranks were replaced with the bearings. It should decrease the clearances in the joint and make the repair process simple. In this design both red and blue inputs are made as a single part, because the actuation for both sides of the joint is symmetrical. This feature simplifies the control and eliminates the singularity position from the joint's workspace. The only place where the sliding contact is preserved is between the base of the joint and the central sphere. It is necessary in order to keep high load capacity of the joint.

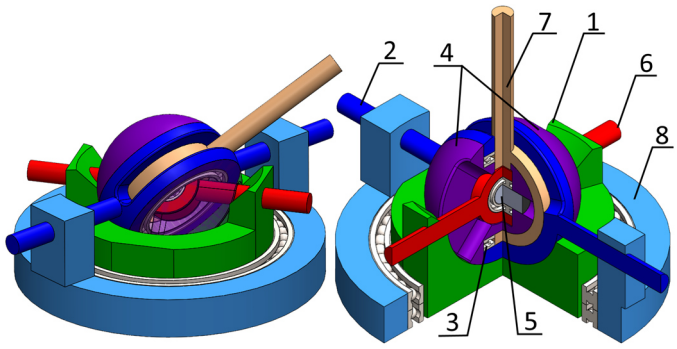

a) b)

Figure 57. Crankless design 1st concept: a) general view; b) cross-section.

The main part of the joint is an integral central sphere which is placed on a base

1 with a concave spherical surface. The central sphere consists of a blue input 2, in which two radial bearings 3 are installed. Two spherical segments 4 are inserted in the inner races of the bearings. These segments are also connected to the shaft 5, which links the sphere with the red input 6. The output rod 7 is made one with the ring-like part and is placed on the same surface as the bearings. During the actuation, the axis of blue and red input change their relative position, which creates the necessity in making blue actuator floating around the base. For that purpose, additional ring 8 was designed to be a frame for the blue actuator.

The maximum output rod deflection is $\pm 73°$ in one plane and $\pm 45°$ in the other. One of the maximum deflection angles is smaller than the other one because it is impossible to make the slot in part 4 bigger. The workspace of this joint design has irregular shape and constitutes 27.9% of the sphere. The contact surface area of the central ball assembly and the base constitutes 44% of the sphere, which provides good passive load capacity. Active load capacity is also good due to the big cross section of the main load transmitting parts. The joint does not need the measures related to the clearance compensation because of the use of bearings that can be replaced after significant wear will occur.

Unfortunately, this design also has several disadvantages. The floating actuator will create inertia forces which will affect the mechanism. In addition, the joint is really complex to manufacture and assemble with satisfactory enough tolerances as there are many parts with spherical surfaces which should coincide.

2.2.6. Design 6: Crankless design 2nd concept

The next joint design (see Figure 58) was created in attempt to eliminate the moving actuator and the inertia problems related to it.

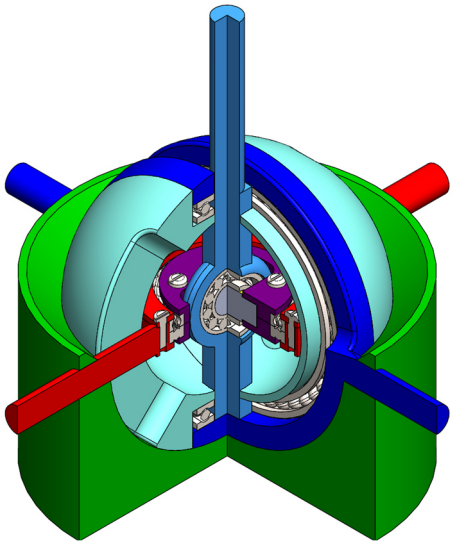

Figure 58. Crankless design 2nd concept.

In this design, the parts equivalent to the additional ring 8 of the previous design, were located inside the central ball. Consequently, the necessity in the moving actuator is eliminated, as all the rotations take place inside the ball, thus decreasing the inertia forces. The maximum output rod deflection is $\pm 78°$ in one plane and $\pm 45°$ in the other. As in the previous joint design, one of the deflection angles is smaller than the other one due to the physical limitations. This limitation makes the workspace shape irregular, constituting 30.11% of the sphere. The passive load capacity of this joint is good as the contact area between the central sphere and the base constitutes 45.84% of the sphere. Good active load capacity is ensured thanks to the big cross section of the load transmitting parts.

The main disadvantage of this design is its complexity, which makes its manufacturing and assembly very hard. The central ball consists of three parts,

whose centers should coincide with minimum tolerance in order to provide the correct joint operation. Although the main purpose of this joint design was the elimination of the clearances and sliding contacts, in real prototype it will be impossible to implement. The real bearing always has a clearance between the balls and the rings. This clearance is necessary to compensate the thermal expansion. In addition, when the bearing reaches its working temperature, there is still a small clearance, which is necessary to prevent jamming. These clearances allow the shafts to move in radial and axial direction, which is normal for most of the applications. However, in this joint design it will lead to misplacing the centers of the spherical surfaces of the central ball. When it takes place, the contact spot area between the bottom part of the central sphere and the base becomes much smaller. Most of the load is taken by the blue part, meanwhile in the top part of the central sphere, the cyan parts come in contact with the blue part, due to the distortion. This undesirable contact induces friction forces in the mechanism. The distortion could be decreased by installation of the second bearing, thus giving the second support for the cyan parts, but there is no space to put it in this joint design. It is possible to enlarge the central sphere in order to put another bearing to each side, but it will increase the dimensions of the joint, which are already the biggest, from all the proposed designs based on a single spherical joint. Considering all the mentioned drawbacks, other designs were proposed.

2.2.7. Design 7: Differential gear-based design 1st concept

In order to get away from the disadvantages of the previous designs, the design concept was changed. The next design (see Figure 59) was inspired by the differential gear. The output rod 1 is attached to the bevel gear 2 and can rotate

around the axle of the cross 3. The rotation of the output rod is controlled with the red and blue shafts (elements 4 and 5 respectively) attached to the proper bevel gears. All the main parts are attached to the frame 6.

The output rod can be deflected to $\pm 35°$ in one plane and to $\pm 180°$ in the other. This range is caused by the limitations associated to the frame of the joint. The volume of the workspace, colored in gray, is depicted in Figure 59.

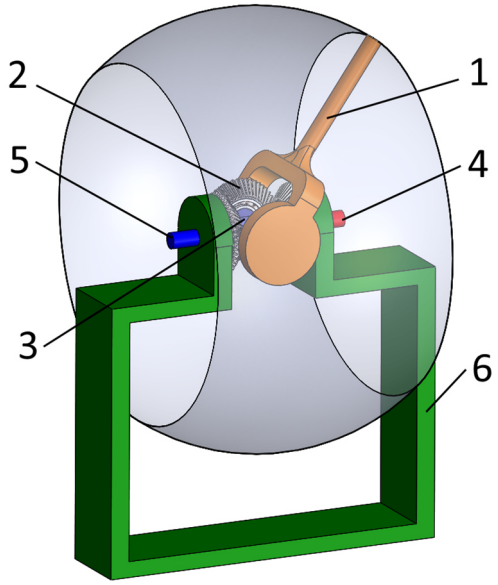

Figure 59. Differential gear-based design 1st concept.

The proposed joint design has several advantages. It is easy to manufacture and control. The moving parts of the joint are comparatively small, which provides low inertia. The theoretical workspace is big, constituting 58% of the sphere. However, in real applications it will be impossible to use this workspace completely because of the physical limitations of the frame. In this design, the frame comes from two sides of the gear mechanism of the joint. If it does not

have a “window” in the bottom part, it cuts the lower part of the workspace. The size of the workspace depends on the size of the “window” in the frame, thus, it depends on the size of the frame. The application of such joint in a mechanism may require increasing the size of the “window” in the joint’s frame, affecting its overall dimensions. In addition, the gears of the joint will have backlash or this backlash can appear as a result of the wear process. This will affect the precision of the joint. In this design, it is impossible to create a mechanism for the backlash compensation. The load capacity of this joint is defined by the load capacity of the bearings, as there is no other surface, which transfers load. The other potential limitation of the load capacity is the strength of the bevel gear teeth, which will be ones of the most loaded points in the joint.

2.2.8. Design 8: Differential gear-based design 2nd concept

In order to improve the performance of the joint, the new design was proposed (see Figure 60). This design contains the main idea of the previous one, but the actuators here are located from one side, which allowed removing the bulky frame and increasing the workspace. To do that, the cross 1 and the red input shaft 2 were made hollow, so blue input shaft could be placed inside them.

The maximum angle of the output rod deflection in one plane is $\pm 121°$ and in the other plane is $\pm 180°$. The joint provides a quite wide workspace, which constitutes 75.86% of the sphere.

The same as the previous design, this joint is easy to manufacture and control. The parts of the joint have low inertia. The dimensions of the joint were decreased due to the location of the actuators. As the actuators of this joint are placed on the same side, the joint can be applied in various mechanisms where

this arrangement is profitable, such as shoulder joint of the humanoid robots, or wrist joint of serial manipulators. However, this joint inherits from the previous design the disadvantage related to the gear backlash, which affects the precision. The load capacity of this joint also will be limited by the bearings and the strength of the parts material.

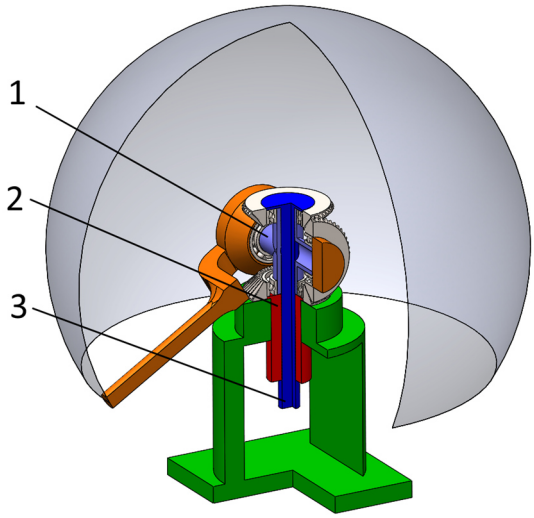

Figure 60. Differential gear-based design 2nd concept.

2.2.9. Design 9: Differential gear-based design 3rd concept

The main disadvantage of the two previous joint designs is a lack of precision due to the gear backlash. As it was impossible to eliminate this problem in those designs, a new joint design was proposed (see Figure 61). This joint is a hybrid between the two previous designs and a ball joint. As in the previous designs, the gears are used to transmit the torque from the actuators to the output rod. The difference is that this joint has three actuators, two of which control the position of the output rod and the third one creates the pretension in the gears in order to compensate the backlash. Though the amount of the actuators increased, the

control of the joint did not become more complex as the compensating actuator executes the same commands as the one, which controls the position of the rod. The hybrid structure of the joint provides bigger passive load capacity and good load distribution, as the contact area between the parts, constituting the central sphere and the base part is large.

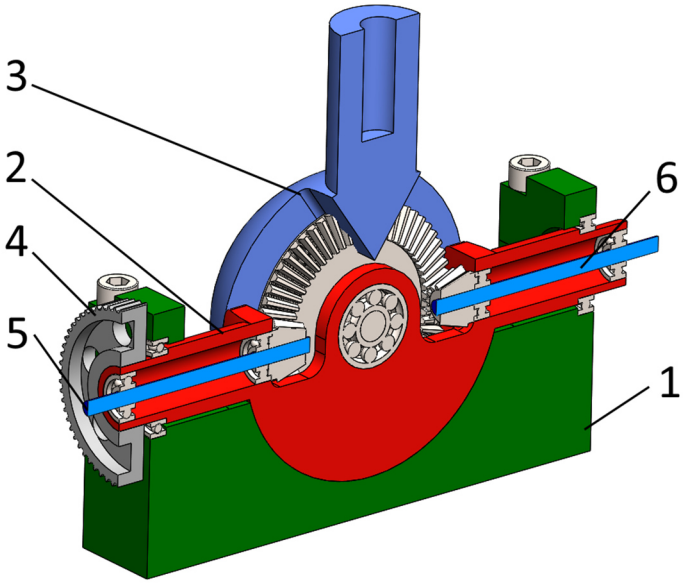

Figure 61. Differential gear-based design 3rd concept.

The joint consists of a base 1, which is in contact with the parts 2 and 3 that form the central sphere. Parts 2 and 3 are connected with an axle, passing through the bearing in the center of the part 2. This connection allows part 3 rotate around part 2. One of the actuators is connected to the part 2 through a pulley 4. This actuator directly controls the deflection of the output rod. Two other actuators are connected to the blue shafts 5 and 6. These actuators control the position of the output rod through the bevel gears. The actuators can work in two modes: high load and high precision. In high load mode, both actuators transmit the

torque through the gears without backlash compensation. In high precision mode, only one actuator transmits the torque, meanwhile the other one creates the pretension in the gears. Depending on the direction of load vector, the actuators switch their functions. In both modes, the actuators connected to the blue shafts, use the same control commands, with only difference in direction.

The output rod can be deflected by the red actuator in range of $\pm 90°$. The blue actuators can deflect the rod in range of $\pm 55°$. It gives the workspace constituting 40.96% of the sphere.

Except mentioned backlash compensation, this joint design has several other advantages. It has small dimensions and as a result, small inertia. The passive load capacity is big due to large contact surface area, constituting 34%-36.25%. The main disadvantage of the joint is manufacturing complexity, as the central sphere consists of two parts that should require precise manufacturing and assembly for operating properly. The other disadvantage is active load capacity, limited by the strength of the gear material, as the gear teeth are the most loaded parts of the design.

2.2.10. Conventional universal joint

In order to provide fair comparison of the proposed designs, a conventional universal joint design should be considered. This type of joint was chosen for the comparison because, form the kinematic point of view, it is the most similar type of joint to the proposed designs. Universal joint can be used in reconfigurable mechanisms with locking devices installed as can be seen in [32], [36], [37]. An example of the cardan joint can be seen in Figure 62.

Figure 62. Universal joint, proposed by RS Components [104].

According to the specifications [104] the maximum working angle of this joint is 45°. In reality the joint can be bent up to $\pm 90°$, however in these extreme positions the range of motion is very limited. Considering the recommended working range and the extremes, the workspace constitutes 20.7% of the sphere. The joint has small dimensions, which provide low inertia forces in the joint. The manufacturing and assembly of the joint is simple and cheap. The accuracy of the joint is good due to the use of needle bearings that can be replaced in case of significant wear. The load capacity is also limited by the bearings.

The main disadvantage of joint is that despite of potentially reconfigurable, significant changes in its design should be made in order to implement it, such as installation of locking mechanisms, axis shifting mechanisms or actuators.

2.3. Assessment and comparison of the proposed designs

The different joint designs that have been proposed in previous section, provide 2 or 3 DOF motion and can be applied in several applications, such as reconfigurable manipulators or haptic devices. In order to choose the best

designs they should be compared by their most important characteristics. As it was stated before, those characteristics are functionality, workspace, accuracy, manufacturing and assembly complexity, load capacity, control complexity, dimensions and inertia. The comparison of the proposed joint designs is presented in Table 1.

Table 1. Joint design comparison

	Functionality (1-10)	Workspace (1 - 10)	WS homogeneity (1-10)	Accuracy (1 – 10)	Manufacturing and assembly complexity (1-10)	Load capacity (1 – 10)	Dimensions (1 – 10)	Inertia (1 – 10)	Total
Design 1	4	1	10	9	9	10	9	9	61
Design 2	10	2	10	5	3	6	1	1	38
Design 3	7	7	9	3	4	1	7	8	46
Design 4	7	4	10	4	5	5	8	7	50
Design 5	5	5	8	6	2	8	4	2	40
Design 6	7	6	7	7	1	9	5	5	47
Design 7	6	9	5	1	8	4	2	3	38
Design 8	9	10	10	2	7	3	3	4	48
Design 9	8	8	6	10	6	7	6	6	57
Conventional U-joint	3	3	4	8	10	2	10	10	50

Each characteristic has been evaluated with 10 grade scale, where 1 is the worst result and 10 is the best. Where it was possible, the joints were ranked from the worst to the best with no repeating grades (workspace, accuracy, manufacturing complexity, load capacity, dimensions, and inertia). The other parameters could have the same results for several joints. If the joints share the same grade, then the next joint has a grade that is bigger or smaller by one. In this case, the lowest grade may not be one.

The functionality parameter is rated considering the number of DOF, possibility of reconfiguration, actuator arrangement and type of the joint (active or passive).

The workspace grade is directly proportional to the workspace size. However, the size cannot be the only criteria of workspace estimation because sometimes the workspace can be wide, but having a very irregular shape, which complicates the motion control along this workspace. Thus, in order to provide more information about the workspace, the workspace homogeneity parameter was introduced. This parameter represents how regular the shape of the workspace is. To clarify the grading, the workspaces of the joints (see Figure 63) should be considered.

The workspaces 1 (designs 1, 2 and 4) and 4 (design 8) are completely homogenous. They have the shape of a spherical dome without any cuts. These workspaces have the highest grade (10). The workspaces 2 (design 3) 3 (designs 5 and 6) and 6 (design 9) have relatively small cuts. These designs were assigned with the grades 9-6, respectively. The workspaces 5 (design 7) and 7 (conventional universal joint) have big cuts. These designs were assigned with the grades 5 and 4, respectively.

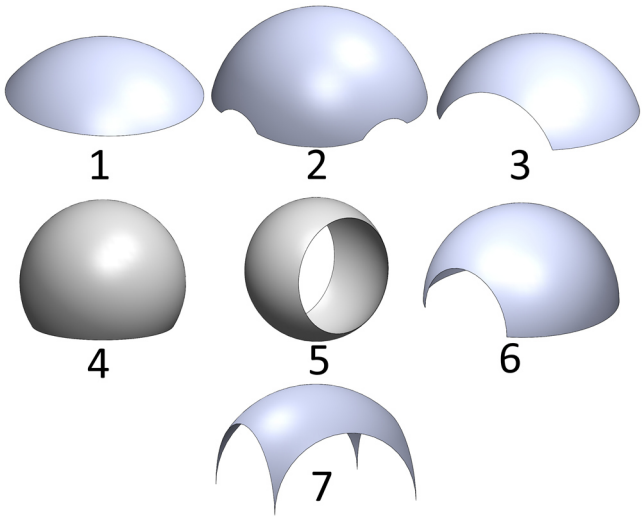

Figure 63. Workspace shapes.

The grade for the accuracy depends on the possibility of clearance compensation implementation, and design features that affect accuracy, for instance parts affected by bending and wear.

Manufacturing and assembly complexity, load capacity, dimensions and inertia are quantitative parameters and are ranked from the worst joint to the best one within the 10-grade scale. Inertia is rated so that the high grade is assigned to the joint designs with small inertia.

It can be seen from the Table 1 that the best results are obtained for the lockable passive joints. It makes sense because of their simple design, which is very similar to the conventional spherical joint design. These joints inherit all the advantages of the conventional joints, which compensate lack of functionality and workspace. The control complexity of this joint depends more on the control

complexity of the mechanism, where they are applied, and it can be quite complex. According to the rating, the second best joint design is the differential gear-based joint design 3rd concept. This joint has most of the parameters slightly higher than average, top grade for accuracy and third workspace size. The bi-actuated design 2nd concept and the conventional universal joint share the third place. Most of the parameters of the bi-actuated design 2nd concept are average, but it has small dimensions and low inertia. In addition, it has good accuracy and workspace homogeneity. Conventional universal joint has the highest possible grade for manufacturing complexity, dimensions and inertia, but the lowest for functionality and workspace homogeneity. The rest of the criteria are also quite low. Most of the other joint designs have their grades in range from 40 to 48. The worst result is presented by the active spherical joint with Cartesian and revolute actuation and the differential gear-based joint design 1st concept (38 points). The first of them has the best functionality, and medium load capacity, but big dimensions, complex design and small workspace make this joint uncompetitive. The second joint has good workspace and manufacturing complexity and medium functionality and workspace homogeneity. The rest of the parameters have low grades.

Therefore, resulting from the established comparison, the best four designs are:

1. Lockable passive joints
2. Differential gear-based design 3rd concept
3. Active 2R spherical mechanism-based joint 2nd concept and conventional universal joint

However, the parameters in the current comparison are quite general and cannot fully represent the qualities of the joints. The functionality parameter does not

fully represent the reconfigurability potential of the joints. It is hard to create a simple objective criterion, which can numerically describe all potential applications of the reconfigurable joint.

In order to provide better view over this aspect, the possibility of implementation of different reconfigurable strategies should be considered (see Table 2).

Table 2. Possibility of joint application in different reconfiguration methods.

Reconfigurability approach / Joint design	Modularity	Additional actuation	Detaching links	Changing links dimensions	Blocking actuators or joints	Changing axis orientation
Lockable passive joints	+	-	-	-	+	±
Differential gear-based design 3rd concept	+	+	-	-	+	+
Active 2R spherical mechanism-based joint 2nd concept	+	+	-	-	+	+
Conventional universal joint	+	-	-	-	-	-

As it can be seen, most of the joints can be used in the same reconfiguration methods with few exceptions. Lockable passive joints cannot be used in additional actuation method, as they cannot be actuated. In addition, lockable passive joints cannot provide infinite amount of axis positions, when changing axis orientation method of the reconfiguration is used. The other proposed designs provide infinite amount of axis positions, which widens the application field of these joints.

It should be noted that the universal joint, which is present in this comparison, is only potentially reconfigurable. It needs significant alterations in its design to obtain reconfigurability. In addition, possibly, after these changes it will have different characteristics than the ones that were considered here. The easiest way to modify the universal joint is the installation of the locking mechanisms, such as in [32] or [36]. In this case, the universal joint can be also used in blocking joints reconfiguration approach.

Consequently, taking into consideration all the characteristics, differential gear-based design 3rd concept and active 2R spherical mechanism-based joint 2nd concept are the most promising joints, which can be applied in most of the reconfiguration strategies. As it can be seen in Table 1, the joints characteristics differ, providing advantages in various areas. The differential gear-based design 3rd concept joint design has bigger workspace, clearance compensation in active and passive modes and load capacity. The active 2R spherical mechanism-based joint 2nd concept joint design is smaller and simpler; it has a more uniform workspace and smaller inertia forces inside.

In order to define the best design, the characteristics of the proposed joint designs were studied in detail. The kinematics of the joints is presented in sections 3.1.1 and 3.2.1. The quasi-static analysis, which studies the force transmission in the joints, is considered in sections 3.1.3 and 3.2.3. The indication of the most stressed points in the designs was done with the finite element analysis in sections 3.1.4 and 3.2.4. In order to test the performance of the proposed designs, the prototypes were manufactured (see sections 0 and 4.2) and tested (see section 5). The prototypes were applied as haptic devices, which controlled five bar flexible mechanism, designed by COMPMECH research group. This application

was chosen, 2R joints are used often in haptic devices as it was demonstrated in section 1.2. The proposed joints implement the reconfiguration method consisting in relocation of the axis of one of the revolute joint. Being used in a haptic device, this feature provides additional precision, when the controlled mechanism should follow straight line, without any undesirable deviations. Considering a number of researches dedicated to haptic devices, the experimental plan was proposed in Section 5. The experimental setups for both joints are considered in Sections 0 and 4.2. The detailed discussion on the experimental results is presented in section 5.3. Finally, the conclusions about the joints' performance were made in Section 5.4.

3. Kinematic and quasi-static analysis of joints under study

The joint designs, Active 2R spherical mechanism-based joint and Differential gear-based design, proposed in Chapter 2 and selected in Section 2.3, should be considered in detail in order to identify their strong and weak points. In order to do that, in subsequent Sections the position analysis, the velocity equations, the workspace characterization, quasi-static and finite element analysis will be presented. The position analysis consists of direct and inverse position problem solving, relating input and output variables. As active 2R spherical mechanism-based joint has two blue input cranks which require different input commands, the relationship between these cranks will be considered. Next, the velocity equations will be obtained and the joint workspace will be characterized with performance indices. In the quasi-static analysis, the force transmission from the actuators to the end of the joint's rod will be presented. Finally, in finite element analysis section, the verification of the structural properties of the joints will be executed.

3.1. Active 2R spherical mechanism-based joint

3.1.1. Position analysis of the joint

3.1.1.1. Direct position problem

First, the direct position problem of the active 2R spherical mechanism-based joint will be performed. For that, the position parameters of the joint that can be

seen in Figure 64, and which corresponds to a schematic representation of Figure 56a, should be considered. Here, vector $\boldsymbol{n}$, which represents the rod of the joint, is placed in the intersection line of the planes: red and blue. These planes pass through the centers of the grooves of the central sphere and are perpendicular to each other as are the grooves. The planes are controlled with the cranks of corresponding color, where, α and β are input variables of red 2 and blue 3 cranks, respectively. The red plane is rotated around the X-axis directly by its crank. The normal vector of the plane, $\boldsymbol{n_\alpha}$, which determines its orientation in space, can be written as:

$$\boldsymbol{n_\alpha} = \begin{Bmatrix} 0 \\ -cos\alpha \\ sin\alpha \end{Bmatrix} \tag{1}$$

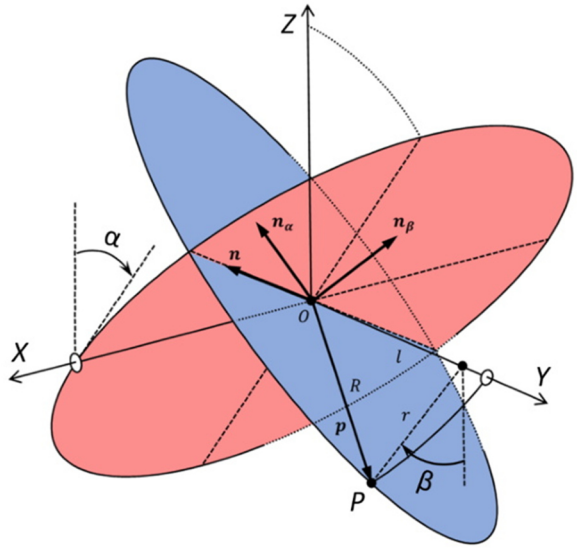

Figure 64. Position parameters of the joint [105] in isometric view.

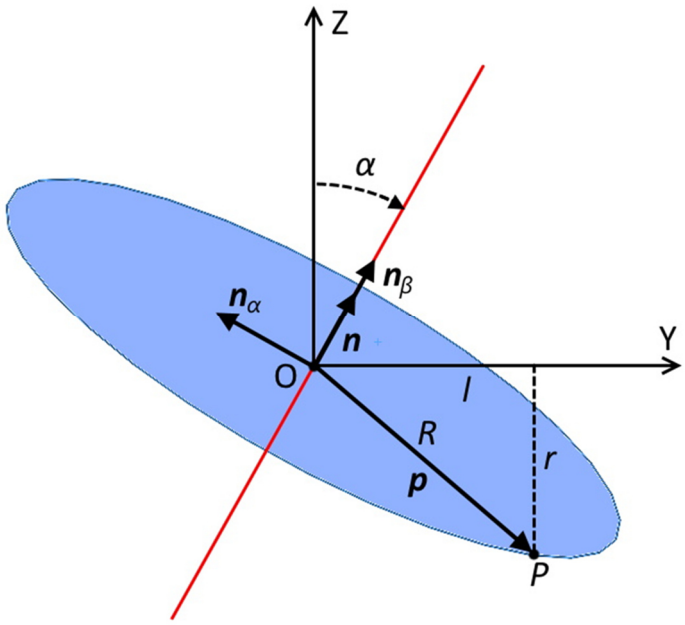

Figure 65. Position parameters of the joint [105], projection in the YZ.

However, the blue crank does not rotate the blue plane directly. It is connected with the crank through the intermediate link (4 in Figure 56a), which is represented as point P in Figures 64 and 65. In real model, point P is located where the axis of rotation of the intermediate link crosses the contour of the central sphere. In this design it is approximately in the middle of the link, but in the schematic representation the link itself can be reduced to this point. The position vector of the point P is defined mainly by the parameters of the blue crank (its length r and input value β) and the radius R of the central sphere, which together define the parameter $l = \sqrt{R^2 - r^2}$. Considering that, the position vector $\boldsymbol{p}$ can be put as,

$$\boldsymbol{p} = \begin{Bmatrix} r sin\beta \\ l \\ -r cos\beta \end{Bmatrix} \tag{2}$$

The normal vector of the blue plane, which characterizes its location, $\boldsymbol{n_\beta}$, can be obtained as,

$$\boldsymbol{n_\beta} = \boldsymbol{n_\alpha} \times \boldsymbol{p} = \begin{Bmatrix} r cos\alpha cos\beta - l sin\alpha \\ r sin\alpha sin\beta \\ r cos\alpha sin\beta \end{Bmatrix} \tag{3}$$

Now, the vector $\boldsymbol{n}$, which represents the rod of the joint can be calculated as,

$$\boldsymbol{n} = \boldsymbol{n_\alpha} \times \boldsymbol{n_\beta} \tag{4}$$

This results in,

$$\boldsymbol{n} = \begin{Bmatrix} -r sin\beta \\ sin\alpha(r cos\alpha cos\beta - l sin\alpha) \\ cos\alpha(r cos\alpha cos\beta - l sin\alpha) \end{Bmatrix} \tag{5}$$

To simplify the solution of the inverse position problem (see Section 3.1.1.2), vector $\boldsymbol{n}$ can be transformed by dividing it by the z component, resulting in:

$$\boldsymbol{n} = \begin{Bmatrix} \dfrac{-r sin\beta}{cos\alpha(r cos\alpha cos\beta - l sin\alpha)} \\ tan\alpha \\ 1 \end{Bmatrix} \tag{6}$$

In order to solve the direct position problem, the relation of the input variables to the output variables should be found. This step is necessary to ensure that every solution, which is valid for the input variables of the mechanism, is

detected.

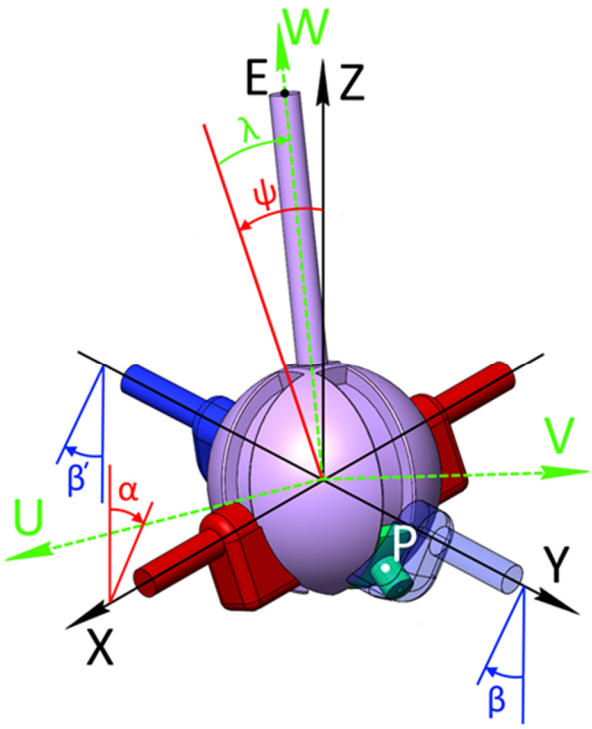

Figure 66. Representing the location of the joint's rod.

To find the orientation of the rod given by the output variables, two coordinate frames should be considered – fixed frame XYZ and moving frame UVW. At first, when the output variables ψ, λ are zero and the rod is vertical, the frames coincide. Then the rotation around the X-axis (output variable ψ) takes place (see Figure 66). After that, the rotation around the V-axis can be done (output variable λ). It should be noted, that due to the design features, this is the only possible order of rotations, which is possible in this mechanism. If the other order is used, it leads to the displacement of the axis of rotation of the red cranks, which becomes not perpendicular to the axis of the blue cranks. And due to the

physical restrictions, it is not possible in this design.

The described rotation order can be put in the matrix form by means of rotation matrices:

$$\boldsymbol{R}_{\psi,U} \cdot \boldsymbol{R}_{\lambda,V} = \begin{bmatrix} cos\lambda & 0 & sin\lambda \\ sin\psi sin\lambda & cos\psi & -cos\lambda sin\psi \\ -cos\psi sin\lambda & sin\psi & cos\psi cos\lambda \end{bmatrix} \tag{7}$$

Now, the orientation of the rod can be found by multiplying the rotation matrix by the vector of the rod in its vertical position:

$$[\boldsymbol{R}_{\psi,U}][\boldsymbol{R}_{\lambda,V}]\begin{Bmatrix}0\\0\\1\end{Bmatrix} = \begin{Bmatrix} sin\lambda \\ -cos\lambda sin\psi \\ cos\psi cos\lambda \end{Bmatrix} \tag{8}$$

Finally, utilizing the equations (5) and (8), the system of equations that relate inputs α and β to outputs λ and ψ can be acquired. It should be mentioned that the coordinates of $\boldsymbol{n}$, given by equation (5) have been divided by its modulus to obtain a unit vector.

$$\boldsymbol{n_x} = sin\lambda = \frac{-rsin\beta}{(r^2 sin\beta^2 + (rcos\alpha cos\beta - lsin\alpha)^2)^{0.5}} \tag{9}$$

$$\boldsymbol{n_y} = -cos\lambda sin\psi = \frac{sin\alpha(rcos\alpha cos\beta - lsin\alpha)}{(r^2 sin\beta^2 + (rcos\alpha cos\beta - lsin\alpha)^2)^{0.5}} \tag{10}$$

$$\boldsymbol{n_z} = cos\psi cos\lambda = \frac{cos\alpha(rcos\alpha cos\beta - lsin\alpha)}{(r^2 sin\beta^2 + (rcos\alpha cos\beta - lsin\alpha)^2)^{0.5}} \tag{11}$$

Equations (9) to (11) provide the coordinates of vector $\boldsymbol{n}$.

From equation (9), the value of λ as a function of the inputs is obtained as:

$$\lambda = sin^{-1}\left(\frac{-rsin\beta}{(r^2sin\beta^2 + (rcos\alpha cos\beta - lsin\alpha)^2)^{0.5}}\right) \quad (12)$$

Dividing equation (10) by equation (11) we obtain:

$$-tan\psi = tan\alpha \quad (13)$$

From equations (12) and (13) it is clear that, several solutions will exist for the same values of input variables. For the range $\alpha \in [-\pi, \pi]$ and $\beta \in [-\pi, \pi]$, the following set of solutions of the direct position problem is obtained: $\begin{Bmatrix} (\psi, \lambda) \\ (\psi, \pi - \lambda) \\ (\pi + \psi, \lambda) \\ (\pi + \psi, \pi - \lambda) \end{Bmatrix}$

3.1.1.2. Inverse position problem

From the equations (9-11), components of vector $\boldsymbol{n} = (u \quad v \quad 1)^T$ were obtained. Considering equation (6), the input α can be found as:

$$\alpha = tan^{-1}v \quad (14)$$

However, calculating the input β is not straightforward, as it depends on the value of input α. In order to obtain it, the following equation should be solved:

$$(urcos^2\alpha)cos\beta + rsin\beta = ulsin\alpha \cos\alpha \quad (15)$$

To simplify the solution, dividing Eq. (15) by r and reorganizing the (16)

equation, it results in:

$$n\cos\beta + \sin\beta = m$$

where,

$$n = u\cos^2\alpha \tag{17}$$

$$m = \frac{ul}{r}\cos\alpha\sin\alpha \tag{18}$$

Next, a supplementary variable φ is introduced:

$$\varphi = \tan\frac{\beta}{2} \tag{19}$$

Utilizing the trigonometric relationships:

$$\sin\beta = \frac{2\tan\frac{\beta}{2}}{\left(\tan\frac{\beta}{2}\right)^2 + 1} \tag{20}$$

$$\cos\beta = \frac{1 - \left(\tan\frac{\beta}{2}\right)^2}{\left(\tan\frac{\beta}{2}\right)^2 + 1} \tag{21}$$

and substituting into equation (16) we obtain:

$$-(n-m)\varphi^2 + 2\varphi + n - m = 0 \tag{22}$$

By solving this equation and substituting φ given by equation (19) we obtain the roots:

$$\beta = 2\tan^{-1}\left(\frac{(1 \pm (1 - m^2 + n^2)^{0.5})}{n + m}\right) \tag{23}$$

Finally, substituting the values of n and m, given by equations (17) and (18), the input angle β yields:

$$\beta = 2\tan^{-1}\left(\frac{\left(1 \pm \left(1 - \left(\frac{ul}{r}\cos\alpha\sin\alpha\right)^2 + (u\cos^2\alpha)^2\right)^{0.5}\right)}{u\cos^2\alpha + \frac{ul}{r}\cos\alpha\sin\alpha}\right) \tag{24}$$

Typically, there are two solutions for each given value of ψ and λ. The blue crank can take two physical positions, as it is presented in Figure 67. In this Figure, the cranks in positions, corresponding to alternative solutions are semi-transparent.

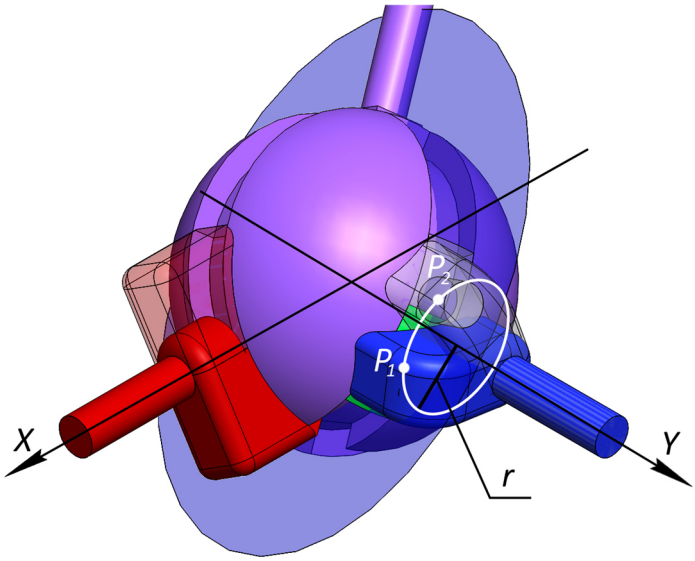

Figure 67. Possible solutions for α and β inputs.

The red crank solutions are $(\alpha, \quad \alpha \pm \pi)$. In order to find β solutions, we need

to consider a circumference, formed by rotation of point P around axis Y (blue crank axis of rotation) and the blue plane. Normally, the blue plane intersects this circumference in two points, which gives two possible positions of point P (see Figure 67). When the blue plane is tangent to the circumference, the solution will be unique. Knowing the positions of point P, β can be found in a way, presented in Figure 64.

The second solution, shown in Figure 67 are impossible for the real joint due to the design features. The top ring limits the range of rotation of both cranks to $\pm 90°$. Thus, only one solution for each crank is available.

3.1.1.3. Relationship between the blue input cranks

When input angle $\alpha \neq 0$, the blue cranks cannot be actuated symmetrically. In this case, they have a nonlinear relationship between input angles β and β'. In order to explain it, the Figures 64 and 66 should be considered.

First, the equation of the blue plane (see Figure 64) should be obtained. It can be done by using the normal vector $\boldsymbol{n_\beta}$, that defines this plane (equation (3)) and the point O, which is located in the center of the sphere. As the blue plane passes through the be origin, point O belongs to the blue plane.

$$(r\cos\alpha\cos\beta - l\sin\alpha)x + r\sin\alpha\sin\beta\, y + r\cos\alpha\sin\beta\, z + D = 0 \quad (25)$$

$$0x + 0y + 0z + D = 0 \quad (26)$$

From equation (26) it is clear that $D = 0$. By dividing the equation (25) by the coefficient of x component we obtain:

$$x + \frac{rsin\beta tan\alpha}{rcos\beta - ltan\alpha} y + \frac{rsin\beta}{rcos\beta - ltan\alpha} z = 0 \quad (27)$$

Now, the point *P* should be considered. It belongs to both, the blue plane and the blue crank. As the crank rotates around its axis (being axis Y), point P forms a circumference around it. The radius of this circumference is the radius r of the blue crank.

$$\begin{cases} x^2 + z^2 = r^2 \\ y = -l \end{cases} \quad (28)$$

The intersection of the blue plane and the circumference of the point *P*, in most cases provides two solutions (see Section 3.1.1.2). However, it can provide one solution, when the blue plane is tangent to the circumference.

Combining the equations (27) and (28) we obtain the equation of the intersection,

$$(1 + g^2)z^2 - (2gh)z + (h^2 - r^2) = 0 \quad (29)$$

where,

$$g = \frac{rsin\beta}{rcos\beta - ltan\alpha}$$
$$h = \frac{rlsin\beta tan\alpha}{rcos\beta - ltan\alpha} \quad (30)$$

According to the discriminant formula, the roots of the equation (29) are:

$$z = \frac{2gh \pm \sqrt{4g^2h^2 - 4(1 + g^2)(h^2 - r^2)}}{2(1 + g^2)} \quad (31)$$

Considering the projection of the radius r to the Z-axis, it is clear that,

$$z = r\cos\beta' \tag{32}$$

Solving the equation (32), input β' can be found as:

$$\beta' = \cos^{-1}\left(\frac{z}{r}\right) \tag{33}$$

As it was said, typically two solutions are obtained for β', however, due to the physical limitations of the joint design, the cranks' rotation angles are limited to $\pm 90°$. This means that the solution, presented in Figure 67b, cannot be implemented in this design.

In Figure 68 the dependency graphs of β' from β for several values of the input α are presented.

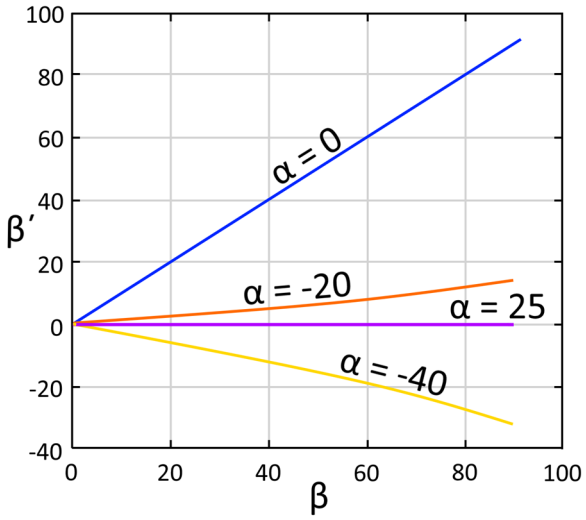

Figure 68. Dependency graphs of β' from β for several values of the input α ($r = 12.68$ mm; $l = 27.19$ mm).

As it can be seen, there are two linear relationship in this graph. The first one, when input $\alpha = 0$ and the second one, when $\alpha = 25°$, which is the singular position for this joint design (see Section 3.1.2.1). The existence of this singularity and the necessity in better load distribution are the reasons why both of the blue cranks were kept in the design of the proposed joint, despite the control complexity.

3.1.2. Velocity equations and workspace characterization

3.1.2.1. Kinematic Jacobians and singularities

Obtaining the Jacobian matrices is an essential step when performing the kinematic analysis of the mechanism. They will enable assessing the workspace provided by the mechanism. In addition, Jacobians are necessary to identify direct and inverse singular positions, which should be known in order to implement successful control.

From equations (12) and (13), it is possible to formulate the position problem as:

$$\begin{cases} f_1: \psi + \alpha = 0 \\ f_2: (r^2 sin\beta^2 + (rcos\alpha cos\beta - lsin\alpha)^2)^{0.5}\ sin\lambda + rsin\beta = 0 \end{cases} \quad (34)$$

After differentiating the system of equations (34) with respect to time and rearranging it into matrix form, direct (left one) and inverse (right one) Jacobians can be obtained:

$$\begin{bmatrix} 1 & 0 \\ 0 & (r^2 sin\beta^2 + (rcos\alpha cos\beta - lsin\alpha)^2)^{0.5} \cos\lambda \end{bmatrix} \begin{Bmatrix} \dot{\psi} \\ \dot{\lambda} \end{Bmatrix} = \begin{bmatrix} -1 & 0 \\ \frac{-\partial f_2}{\partial \alpha} & \frac{-\partial f_2}{\partial \beta} \end{bmatrix} \begin{Bmatrix} \dot{\alpha} \\ \dot{\beta} \end{Bmatrix} \quad (35)$$

where,

$$\frac{\partial f_2}{\partial \alpha} = \frac{\sin\lambda(l\cos\alpha + r\cos\beta\sin\alpha)(l\sin\alpha - r\cos\beta\cos\alpha)}{\left(r^2(\sin\beta)^2 + (l\sin\alpha - r\cos\beta\cos\alpha)\right)^{0.5}} \quad (36)$$

$$\frac{\partial f_2}{\partial \beta} = r\cos\beta + \frac{\sin\lambda\left(2r^2\cos\beta\sin\beta + 2r\cos\alpha\sin\beta\,(l\sin\alpha - r\cos\beta\cos\alpha)\right)}{2\left(r^2(\sin\beta)^2 + (l\sin\alpha - r\cos\beta\cos\alpha)\right)^{0.5}} \quad (37)$$

Considering equation (35), it is clear that the singularities caused by the direct Jacobian of the joint take place when,

$$|\boldsymbol{J}_{DKP}| = 0 \rightarrow (r^2 sin\beta^2 + (rcos\alpha cos\beta - lsin\alpha)^2)^{0.5}\cos\lambda = 0 \quad (38)$$

The inverse problem singularities will occur when:

$$|\boldsymbol{J}_{IKP}| = 0 \rightarrow \frac{df_2}{d\beta} = 0 \quad (39)$$

In Figures 69 and 70, the plots of the values of direct and inverse Jacobians are presented. The singularity positions are highlighted with red straight lines and curves. For every calculation, from now on, the parameters of $r = 12.68$ mm and $l = 27.19$ mm will be used as they are the ones implemented in the proposed joint design.

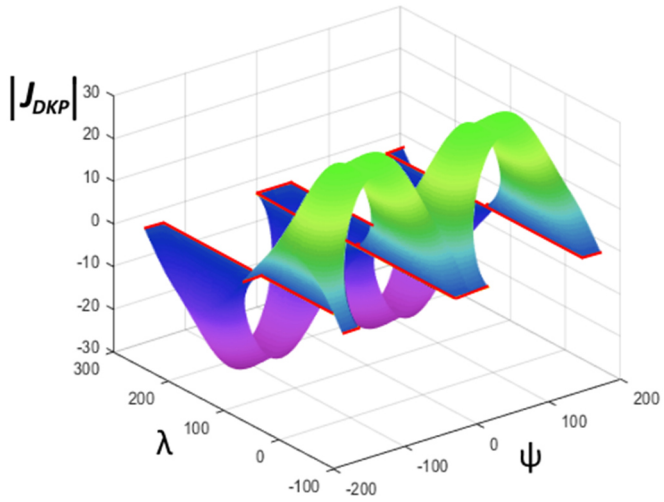

Figure 69. Representation of the direct Jacobian in the workspace

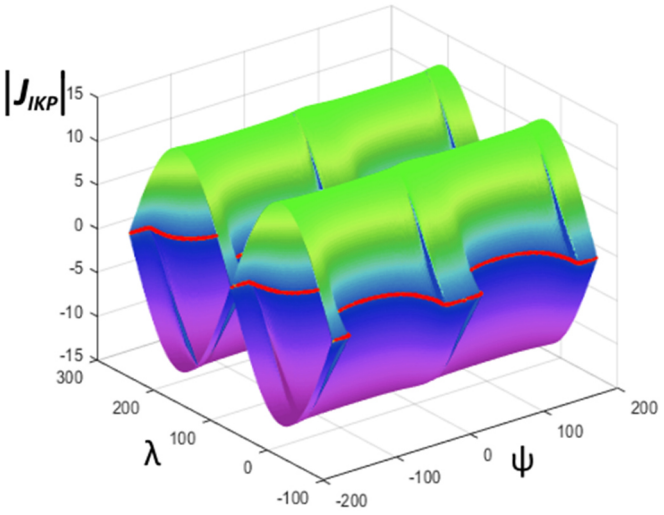

Figure 70. Representation of the inverse Jacobian in the workspace.

Considering Figures 69 and 70, it can be verified that the inverse Jacobian plot presents the singular positions only in the workspace limits. On the other hand,

it can be seen that the singularities on the direct Jacobian plot are located inside the workspace. Setting the mechanism's motion near these singular positions is undesirable because of a possibility of a control loss or breakage of the mechanism. From (38), the direct singularities will take place when:

$$\cos\lambda = 0 \rightarrow \lambda = \pm\frac{\pi}{2} \tag{40}$$

or,

$$r^2 sin\beta^2 + (rcos\alpha cos\beta - lsin\alpha)^2 = 0 \tag{41}$$

It can be seen that there are several possible solutions for the equation (41):

$$sin\beta = 0 \rightarrow \beta = 0 \pm \pi \tag{42}$$

$$rcos\alpha cos\beta - lsin\alpha = 0 \rightarrow \ \beta = 0 \rightarrow tan\alpha = \frac{r}{l} \tag{43}$$

$$rcos\alpha cos\beta - lsin\alpha = 0 \rightarrow \ \beta = \pm\pi \rightarrow tan\alpha = \frac{-r}{l} \tag{44}$$

In the proposed joint design, it is impossible to reach the singular positions, which are characterized by the equation (40). Physically these positions mean that the axis of the rod of the joint will coincide with the axis of the red crank. The physical meaning of the singularity condition, which satisfies equations (42) and (43) is presented in Figure 71. Here, one of the β inputs is in the zero position, meanwhile the axis of rotation of its intermediate link coincides with the axis of one of the rotary pairs of the joint. In this joint design it occurs when red input α equals $25°$.

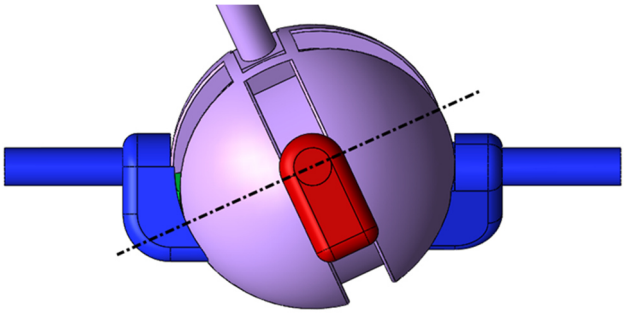

Figure 71. Singular position corresponding to equations (42) and (43).

Also, it can be seen from the Figure 71, that the second blue crank is not in a singular position and continues keeping the joint under control. However, there is a theoretical possibility of reaching the singular position simultaneously for the both blue cranks (see Figure 72). It can occur, when one of the blue cranks is already in the singular position and the other one rotates to $\beta = \pm\pi$. In this case, axes of both of the connection links become collinear with the rotary pair axis. In addition, in the end of the second crank rotation, the rod's axis will coincide with the red crank's axis, as it was mentioned before and presented in Figure 72.

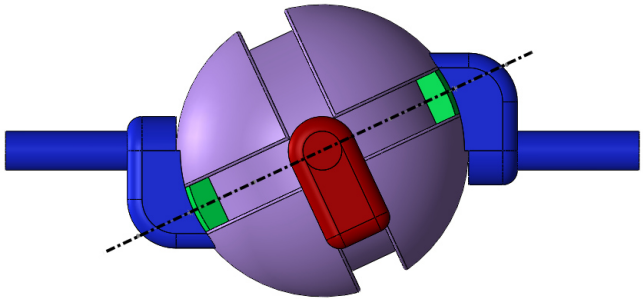

Figure 72. Singular position corresponding to equations (40) and (42-44) (the rod of the joint coincides with the red crank, opposite to the observer).

As a result, this singular position satisfies the equations (40) and (42-44). Both of the possible singularities can be well seen in the plot (see Figure 73), representing the possible coordinates that the extreme of the vector $\boldsymbol{n}$ (see equations 9-11) can take. For the real joint, this plot would represent the possible coordinates of the end of the rod. In this plot, there are four gaps with missing values, corresponding to the singular positions.

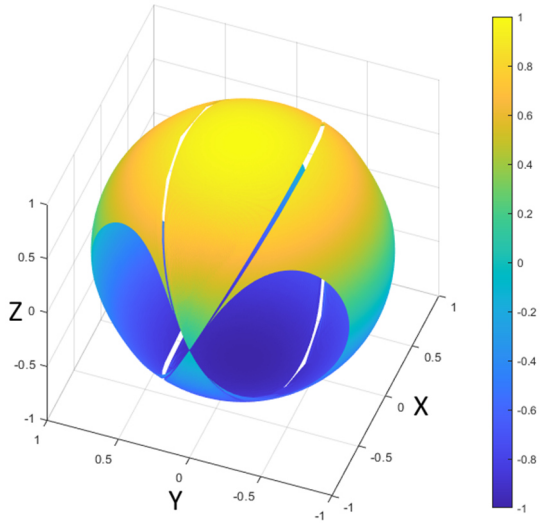

Figure 73. Possible coordinates of the extreme of vector $\boldsymbol{n}$ (point P).

In reality, the singular position where both blue cranks axes are collinear cannot be reached due to the features of the joint design. The top ring limits the rotation of the cranks to $\pm\frac{\pi}{2}$ and the rod orientation to $\pm 55°$ from vertical to any direction. Thus, the joint's controllability is ensured in all the practical workspace.

3.1.2.2. Performance indices

Performance indices represent the motion transmission quality of the mechanism and can serve as optimization criteria of the mechanism's design. The ones of the most widely used indices are Kinematic Conditioning Index (KCI) and Global Conditioning Index (GCI).

3.1.2.2.1. Kinematic Conditioning Index

This index is sometimes referred as the Dexterity Index [106]. Dexterity is the ability of a mechanism to provide precise orientation of its end-effector. In this case, the end of the rod of the joint can be considered as an end-effector. Dexterity Index is directly related to the Jacobians of the mechanism. First step is finding a full Jacobian matrix:

$$\boldsymbol{J} = \boldsymbol{J}_{DKP}^{-1}\boldsymbol{J}_{IKP} \tag{45}$$

Second, the condition number should be found as,

$$\kappa(\boldsymbol{J}) = \|\boldsymbol{J}^{-1}\|\|\boldsymbol{J}\| \tag{46}$$

The condition number itself also can serve for the dexterity assessment, but its value is in range from 0 to ∞. It is a disadvantage, for example for graphical representation. In order to make the evaluation more efficient and visually understandable, KCI was created [107]. It can be calculated as follows,

$$KCI = \frac{1}{\kappa(\boldsymbol{J})} \tag{47}$$

The range of KCI is from 0 to 1, where 0 indicates a singular position and 1

indicates a special point, where the studied mechanism has the highest dexterity. Utilizing the above-stated equations, the values of the KCI for the joint workspace were calculated with the discretization of one degree. The resulting plot is presented in Figure 74.

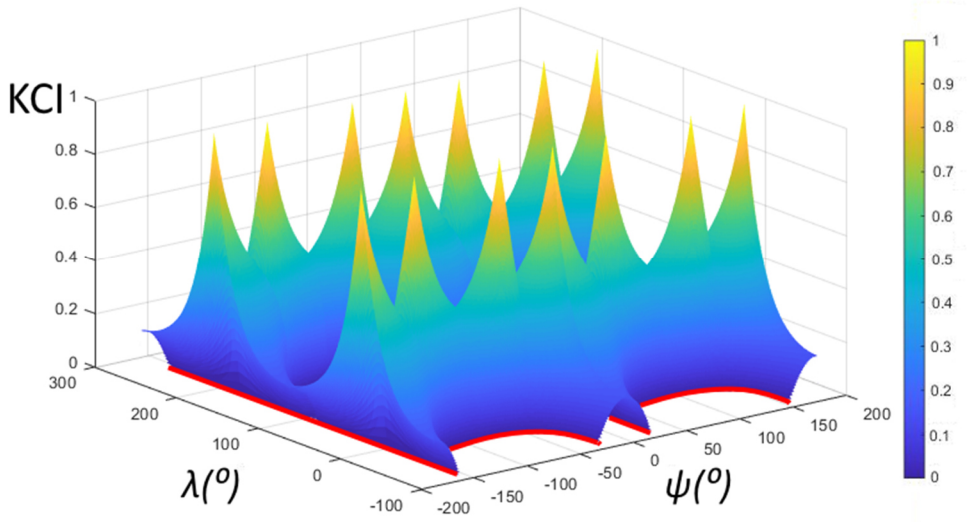

Figure 74. Values of KCI along the workspace.

The singularity positions appearing in the workspace are depicted in red in Figure 74. The curved lines represent the boundaries of the workspace, and the straight lines indicate the singularities, which lay within the workspace. It can be noted that the arrangement of the singular positions is the same as in Figures 69 and 70. Also, there are 14 points, where the joint demonstrates maximum possible dexterity. However, most of these points lay beyond the practical workspace of the joint. Considering the proposed design (see Figure 56a), the practical workspace of the joint is constrained by the top ring, which limits the angle of the rod deflection to 55 degrees in all directions. In other words, the output variables change in range $\in [-55°, 55°]$ $\lambda \in [-55°, 55°]$. In this range,

there is one point of maximum dexterity ($\psi = 0°, \lambda = 0°$), it is located in the center of the workspace (see Figure 75), the second point is located near the boundary ($\psi = 50°, \lambda = 0°$). The dexterity decreases from these two points to the workspace boundaries, where the average value of KCI is 0.33.

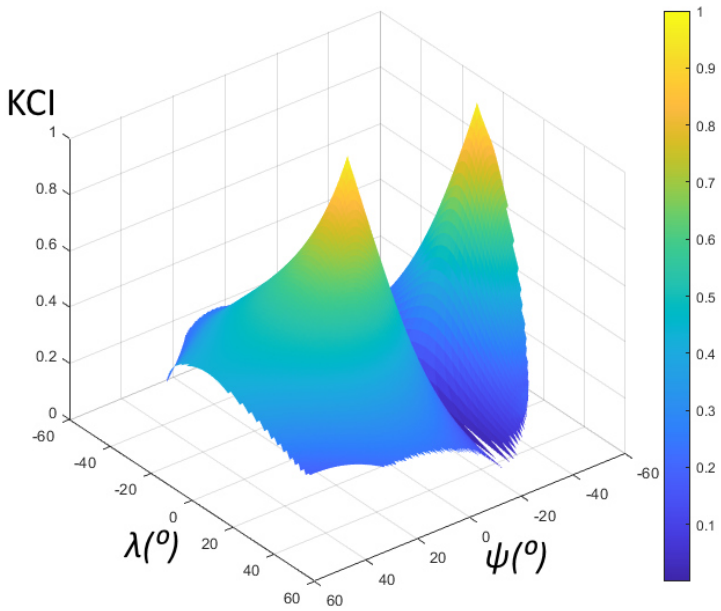

Figure 75. Values of KCI along the practical workspace.

3.1.2.2.2. Global Conditioning Index

GCI was proposed by Gosselin and Ángeles [108] as a measure of the dexterity through the whole workspace of the mechanism. In comparison to KCI, this index does not depend on the links orientation, being the average value of dexterity of the mechanism. It can be calculated as follows,

$$GCI = \frac{1}{n}\sum_{i=1}^{n}\frac{1}{\kappa_i(\boldsymbol{J})} \tag{48}$$

where n is the number of workspace points, for which condition number was calculated.

As KCI, GCI ranges between 0 and 1, being the worst and the best values, respectively. The calculations have indicated that for the theoretical workspace, the value of GCI for the proposed joint is 0.291. For the real workspace of the joint, the value is higher and equals 0.35. This value can be improved by further limiting of the workspace. When the output variables are in range of $[-30°, 30°]$, GCI becomes 0.5. This can be explained by approaching the special point of maximum dexterity on the KCI plot (see Figure 74).

3.1.3. The quasi-static analysis

Quasi-static analysis is necessary to reveal the ways of the force transmission in the joint for the purpose of implementation of control. The force transmission from the actuators to the end-point of the rod will be considered in this section.

The proposed design of the joint has two pairs of the actuated cranks. However, in this section, for the calculation simplicity it will be assumed that only one crank of each color is actuated. The actuation scheme is presented in Figure 76. A certain torque is applied to each of the cranks by their actuators (T_r and T_b in Figure 76). These torques induce two components of the output force F_{red} and F_{blue} (from the red and blue cranks, respectively). These components are applied to the end-point E, which is located on longitudinal axis of the output rod at a radius r_E from the center of the sphere. The axis of the joint's rod belongs to the plane A, which corresponds to the red plane in Figure 64. As it was mentioned before, this plane is rotated directly by the red crank, thus the output force

component F_{red} is perpendicular to the plane A. Also, plane A is perpendicular to the axis of one of the rotary pairs, which is collinear with the axis V in Figure 76.The other component of the output force, F_{blue}, acts within the plane A and is perpendicular to F_{red}. This is caused by the arrangement of the grooves of the joint.

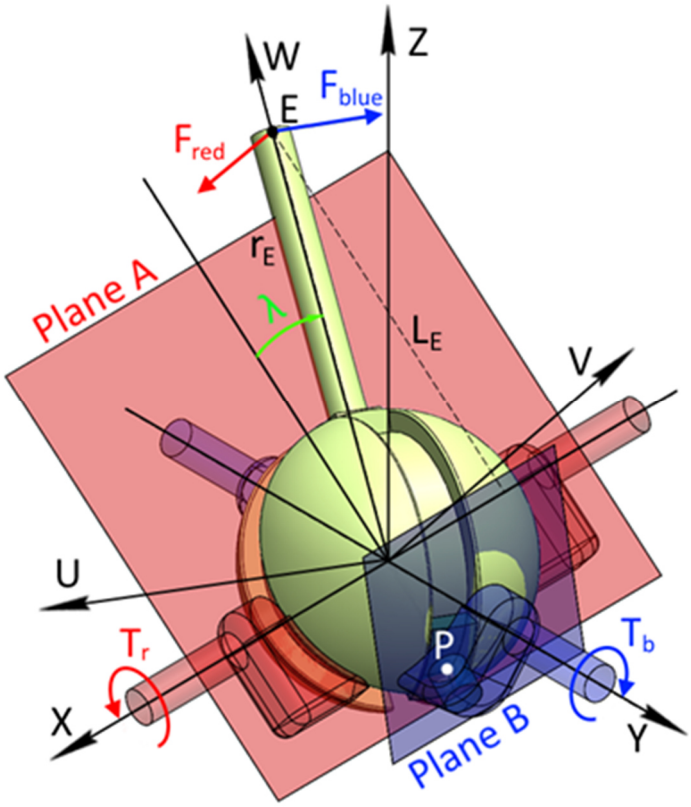

Figure 76. The input torques and the output components of the resulting force.

The output force component, induced by the red actuator is calculated as follows,

$$F_{red} = \frac{T_r}{L_E} \tag{49}$$

where,

$$L_E = r_E cos\lambda \tag{50}$$

Calculation of the F_{blue} is different from F_{red} for all the cases, when the rod of the joint is not in a vertical position. In order to obtain this component, the forces which act on the planes B, A' (see Figure 78) and A and their projections should be considered.

As it mentioned in Section 3.1.1.3, point P forms a circumference while rotating around the axis of the blue crank. This circumference lays in the plane B (dash-dot line in Figure 77), which is parallel to plane ZX. The force F_b is induced by the blue input torque T_b and is applied to point P, which is located on a distance r from the axis of the crank.

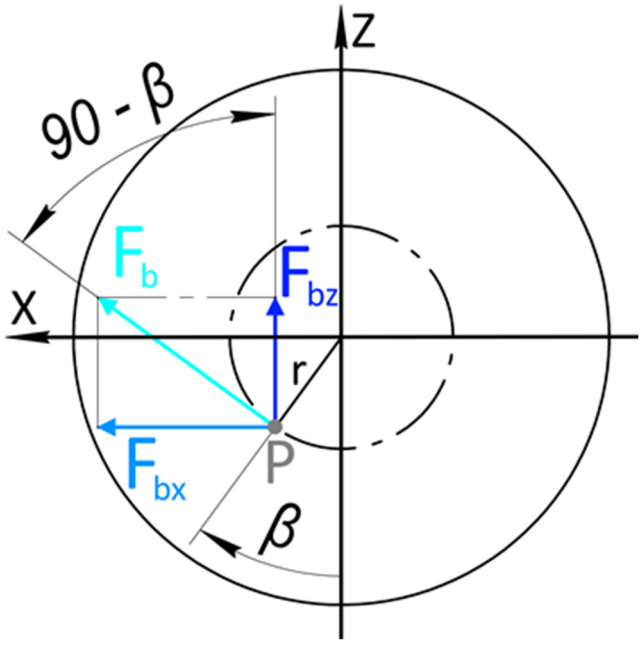

Figure 77. Plane B: force F_b and its projections.

The force F_b, induced by the blue actuator is:

$$F_b = \frac{T_b}{r} \tag{51}$$

As the force F_b is perpendicular to the crank, it should be decomposed in order to be projected to the plane A, where the output blue force component F_{blue} acts. The components of the force F_b can be obtained as follows,

$$F_{bx} = F_b sin\left(\frac{\pi}{2} - \beta_1\right) \tag{52}$$

$$F_{bz} = F_b \cos\left(\frac{\pi}{2} - \beta_1\right) \tag{53}$$

As explained before, the output blue force component F_{blue} acts within the plane A, however, point P does not belong to this plane. In order to continue the calculation, the intermediate plane A', which passes through the point P and is parallel to plane A should be introduced (see Figure 78). Because the planes A' and A are parallel, all the force vectors projected from one plane to another will be equivalent. It allows us working with the plane A' instead of the plane A. It can be noted that in a real joint, the forces, which act within the plane A' will create the bending moments because of the distance between the two planes. These bending moments create the reaction and friction forces, which are neglected in this calculation for simplifying it.

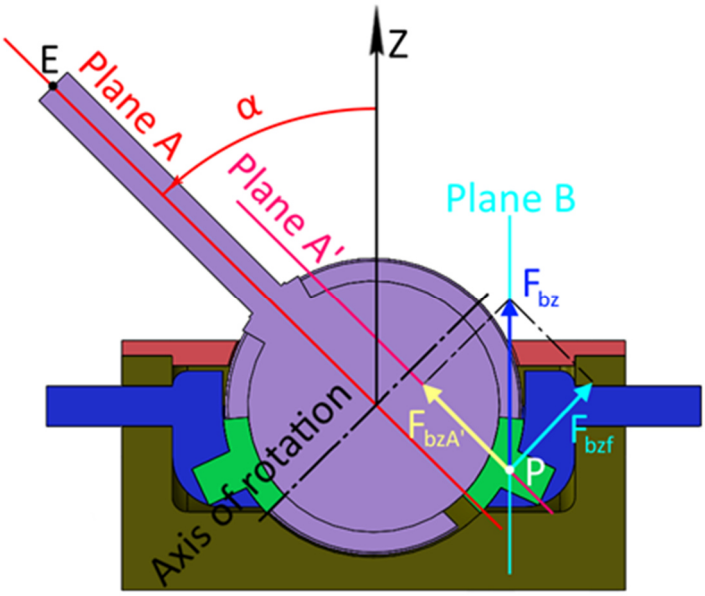

Figure 78. Planes and forces in the joint; cross-section in the YZ plane.

Now, the components of the force F_b should be considered. The F_{bx} component coincides with the intersection line of the planes B and A', thus it has the same value on both of the planes. This component cannot be seen in Figure 78, as it is perpendicular to the YZ plane and has to be seen as a dot, coinciding with the point P. The other component, F_{bz}, should be decomposed and projected on the plane A' in a way, which is presented in Figure 78. The projection $F_{bzA'}$ depends on the input angle α, it exists when $\alpha \neq 0°$. The component F_{bzf} is not participating in the force transmission, as it is directed perpendicular to the plane A', so it produces the friction force between the elements of the joint. The components can be obtained as:

$$F_{bzA'} = F_{bz} cos\alpha \tag{54}$$

$$F_{bzf} = F_{bz} sin\alpha \tag{55}$$

Now, the projection of F_b to plane A' can be calculated as,

$$F_{bA'} = \sqrt{F_{bzA'}^2 + F_{bx}^2} \tag{56}$$

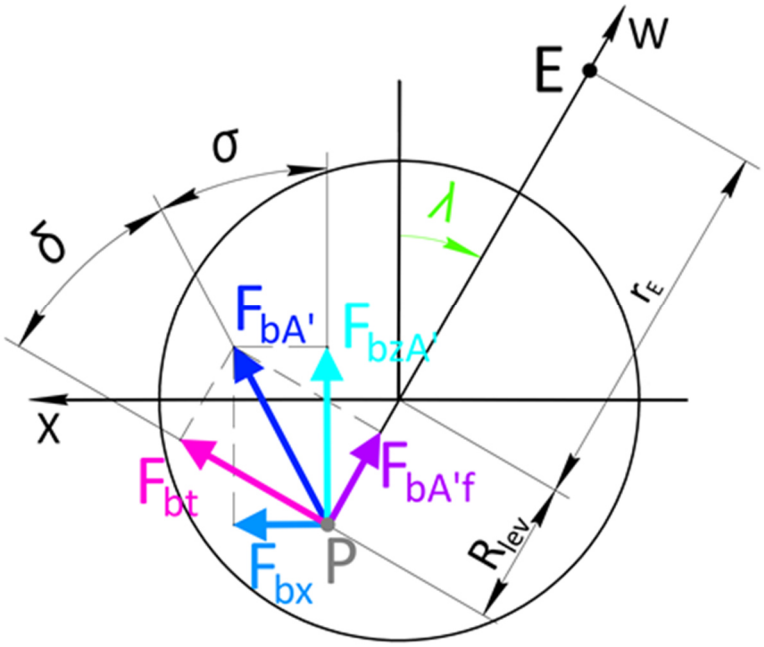

Figure 79. Plane A': forces and their components.

As it is well known, a force, which induces a torque, should be perpendicular to the lever. Typically, $F_{bA'}$ is not perpendicular to the longitudinal axis of the rod (it occurs only when $\alpha = 0°$). Therefore, it is necessary to decompose the force $F_{bA'}$ as it is presented in Figure 79. The component F_{bt} creates the torque around the rotary pair axis and is directly connected to the output force F_{blue}. The other component ($F_{bA'f}$) is directed to the axis of the rotary pair, which induces the

friction force (together with F_{bzf}). The components can be found as,

$$F_{bA\prime f} = F_{bA\prime} sin\delta \tag{57}$$

$$F_{bt} = F_{bA\prime} cos\delta \tag{58}$$

where,

$$\delta = 90 - (\sigma + \lambda) \tag{59}$$

and,

$$\sigma = arccos\left(\frac{F_{bzA\prime}}{F_{bA\prime}}\right) \tag{60}$$

The output blue force component can be found as,

$$F_{blue} = F_{bt}\frac{R_{lev}}{r_E} \tag{61}$$

where R_{lev} is the leverage between point P and the axis of the rotary pair (see Figure 79). In order to locate the vector $\boldsymbol{p}$ (see equation (2)) in the *UVW* coordinate frame, the rotation matrix $\boldsymbol{R_{\psi,U}}$ can be used:

$$\boldsymbol{R_{\psi,U}} \cdot \boldsymbol{p} = \begin{Bmatrix} r\sin\beta \\ l\cos\psi + r\cos\beta\sin\psi \\ l\sin\psi - r\cos\psi\cos\beta \end{Bmatrix} \tag{62}$$

Now R_{lev} can be found as,

$$R_{lev} = \sqrt{(U^2 + W^2)} = \sqrt{(r\sin\beta)^2 + (l\sin\psi - r\cos\psi\cos\beta)^2} \tag{63}$$

Finally, the resulting output force $\vec{F}_{res}$ can be obtained as,

$$\vec{F}_{res} = \vec{F}_{red} + \vec{F}_{blue} \tag{64}$$

The modulus of the force $\vec{F}_{res}$ can be calculated as,

$$F_{res} = \sqrt{F_{red}^2 + F_{blue}^2} \tag{65}$$

As it was noted during the calculation, the force $F_{bA'f}$ and the force F_{bzP} generate a normal force F_n, which is the part of the friction force equation:

$$\vec{F}_n = -\left(\vec{F}_{bA'f} + \vec{F}_{bzf}\right) \tag{66}$$

$$\vec{F}_F = \vec{F}_n \mu_k, \tag{67}$$

where μ_k is a friction coefficient.

As F_{bzf} component is always perpendicular to plane A', where $F_{bA'f}$ acts, the scalar value of the friction force F_F can be found as,

$$F_F = -\left(F_{bA'f}^2 + F_{bzf}^2\right)^{0.5} \mu_k \tag{68}$$

The described method was applied to obtain the output force F_{res} plot (see Figure 80), the plots of the forces F_{red} and F_{blue} (see Figure 81), which compose it and the friction force F_F (see Figure 83). The forces were calculated for the next set of input parameters, presented in Table 3.

Table 3. Input parameters for the force transmission calculation.

Parameter	Value
Actuation torques (Nm)	3
Distance r_E (mm)	100
Crank radius r (mm)	12.68
Length l (mm)	27.19
Diameter of the central sphere (mm)	60

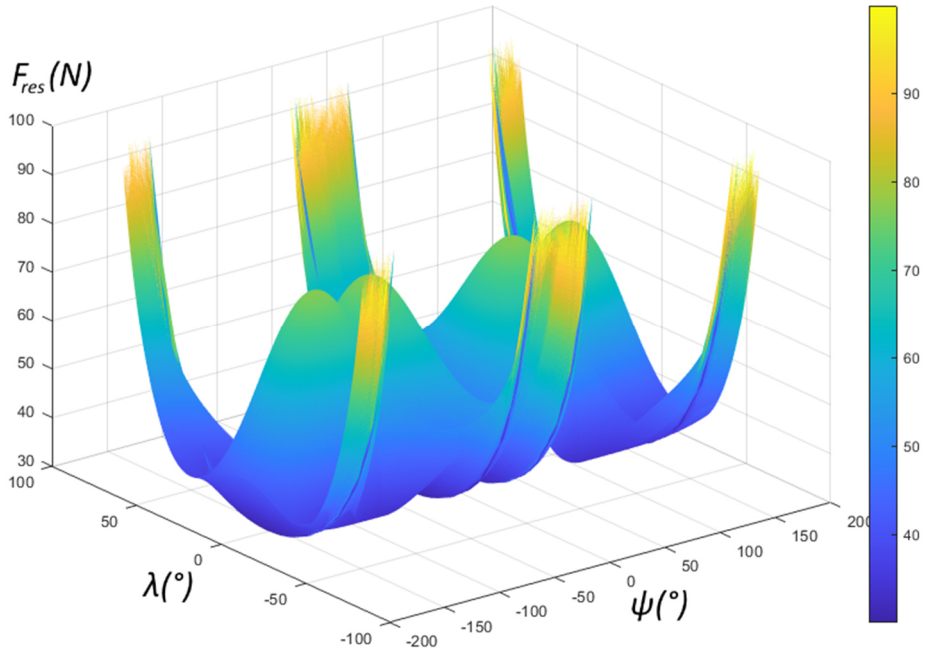

Figure 80. The output force F_{res} as a function of the output variables ψ and λ.

In Figure 80 and Figure 81a, the output variable $\lambda \in [-80°, 80°]$. The range was decreased for the better graphic representation, because when λ values are close to the borders of the range $[-90°, 90°]$, the red output force component F_{red} increases up to infinity due to a decreasing value of L_R (see equation (49)). The blue component of the output force, on the other hand, does not have any value in the singular positions, because the crank that stays in singular position cannot be actuated. In those parts of the plot, mainly F_{red} forms F_{res}.

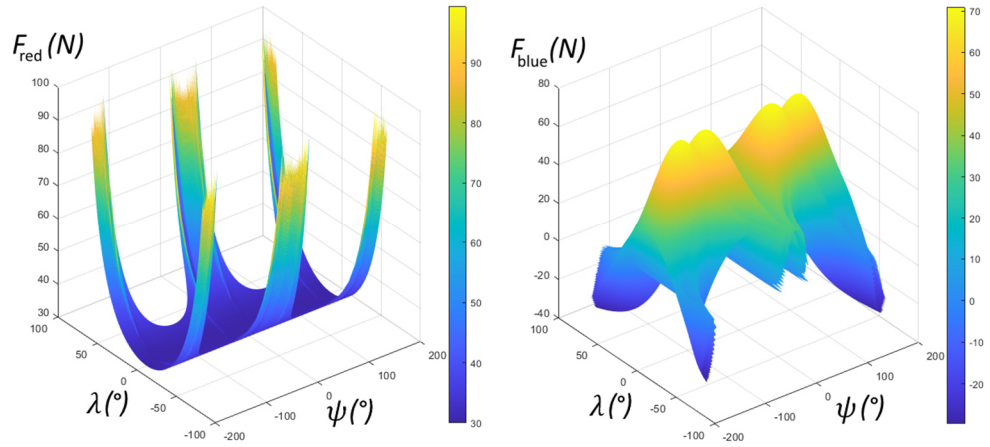

a) b)

Figure 81. The output force components: a) F_{red}; b) F_{blue}.

Considering the plot presented in Figure 80, the areas where both of the output components of the resulting force have similar values can be identified. This happens when $\psi \in [-150°, -40°]$ or $\psi \in [40°, 150°]$, and $\lambda \in [-30°, 30°]$. These areas provide the best force transmission quality. They also correspond to the areas of high dexterity on the KCI graph (see Figure 74). Unfortunately, most of these areas lay beyond the practical workspace of the proposed joint design. The output force values in the real workspace are presented in Figure 82.

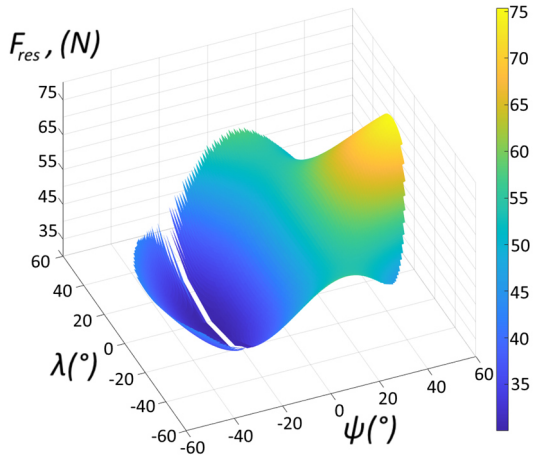

Figure 82. The output force F_{res} in the practical workspace of the joint.

Considering that the prototype of the joint was made of Acrylonitrile Butadiene Styrene (ABS), the friction coefficient $\mu_k = 0.3$ was used as an average value for ABS-to-ABS friction in order to obtain the friction plot, presented in Figure 83.

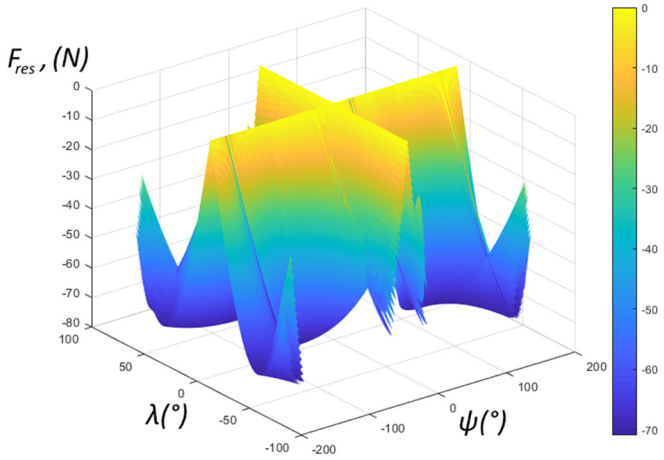

Figure 83. The resulting friction force in the mechanism along the workspace

It can be seen that the friction force equals zero when the joint's rod moves from the vertical position in the intervals $\psi \in [-180°, 180°], \lambda = 0°$ and $\lambda \in [-90°, 90°], \psi = 0°$.

In the first interval, $\beta = 0$ and β' =0, which makes the force F_{bz} zero, according to the equation (53). In this case, the F_{bzf} component of the friction force following the equation (55) is zero. In addition, in this range vectors F_{bt} and F_{bx} coincide, making angle $\delta = 0$, which according to the equation (57) make the second component of the friction force, $F_{bA'f}$, equal zero. In the second interval the plane A (see Figure 76) coincides with the plane ZX, the axis of the rotary pair, which is controlled by the blue actuator and the axis of the blue cranks also coincide. The force F_b can be directly projected to the plane A' and will have the same value as the force F_{bt}. Thus, the rotation is being directly transmitted and the components $F_{bA'f}$ and F_{bzf} equal zero. In other positions, when the plane A is inclined, these components are non-zero and tend to raise with the increase of $|\psi|$ within the range $\psi \in [-90°, 90°]$.

The friction forces in the joint can be decreased by selection of proper materials of the joint parts. The friction coefficient $\mu_k = 0.3$ is a high value, because the ABS-ABS is not a good friction pair and normally it is not being used in industrial applications. For example, if the base part would be made of Teflon or had a Teflon coating, and central sphere of the joint would be made of steel, the coefficient μ_k would be equal 0.04, which will produce almost ten times smaller friction force than for ABS-ABS pair.

3.1.4. Finite element analysis

In order to study the load distribution qualities of the proposed joint design, the finite element analysis was carried out in Ansys Workbench 18.0. During the calculation of the resulting force in the quasi-static static section, the highest force values in the mechanism were identified in the point P (force F_b). It derives from the small radius of the blue crank r. This fact along with the relatively small cross-section and surface area of the intermediate link, allows assuming that the most stressed part of the joint is the blue crank assembly.

For the analysis, the joint was located on the following position: $\alpha = \pm 25°$ and $\beta = 0°$. This position corresponds to the singular conditions, described by equations (42) and (43). In this position, only one of the blue cranks can participate in the joint actuation, thus being the most loaded.

In order to avoid the rigid body motion problem in Ansys Workbench, the CAD model of the joint was reduced to only crucial elements: the blue crank, the intermediate link and the central sphere. In order to fix the blue crank in space, its design was slightly modified by carving a pair of small cones on the ends of the longitudinal axis. It provided two necessary points for the displacement tool of Ansys Workbench. Similar operation was done for the central sphere, where the cones were added at the ends of the axis of a rotary pair, which coincides with the axis V in Figure 76. These actions ensured that the parts will remain in their places, but will freely rotate around their axes. Also, a frictionless support was added to the bottom surface of the sphere in order to release the stress from the points, fixed by the displacement tool and make simulation closer to real conditions. The connections between the elements were set as frictionless

contacts. The mesh was specified as uniform. It consisted of the tetrahedral shape elements with the quadratic displacement behavior (SOLID187) of 2 mm size.

The joint will be applied in haptic device, which will be considered in details in Section 0. According to this application, the joint will create the output force in the end of its rod, which will resist the force, applied by the human operator. In the current simulation it was decided to apply the force that operator creates to the end of the joint's rod and block the input shaft. The value of the force, applied to the rod of 0.1m, was chosen 34.426 N. For the given input conditions, this corresponds to the input torque of 1.89 Nm, which is the maximum holding torque of a stepper motor, used in the experimental setup. Preliminary tests with these parameters revealed that the most stressed part of the joint in this design is its rod. However, the rod can be quite easily modified in comparison to the inner parts of the joint. To omit the influence of the rod on the blue crank examination, the load settings were changed. The torque of 3.426 Nm was applied to the groove on the central sphere to emulate the proper force applied by the human operator. In this particular case, the quasi-static calculation is simplified. F_{bt} will be produced by the equivalent input torque T_i and it will be equal to the force F_b:

$$F_{bt} = \frac{T_i}{r_{lev}} = F_b \tag{69}$$

According to equation (51), the output blue torque T_b can be found as,

$$T_b = T_i \frac{r}{r_{lev}} \tag{70}$$

To find the output torque in Ansys, the moment probe tool was used. It was

applied to the fixed support on the end face of the blue crank. The value of the output torque, provided by the simulation is $T_b = 1.893$ Nm. This coincides with the input stepper motor torque with a small error of 0.106%. Therefore, the finite element model is verified. In Figure 84, the maximum principal stress is presented.

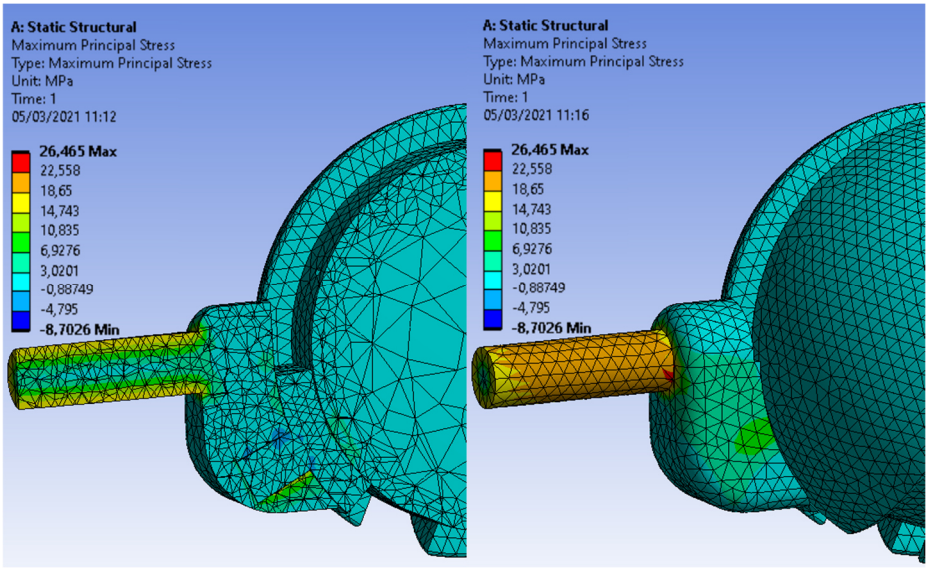

a) b)

Figure 84. The maximum principal stress in the joint (for the motor torque of 1.89 Nm): a) cross section; b) general view.

From Figure 84 it can be seen that the most stressed areas are located at the blue crank's shaft, at the intermediate link and at the part of the central sphere, which is connected to the intermediate link. The stress in the blue crank's shaft can be explained with high torsion load and small cross section of the element. The intermediate link has two contact areas, which are relatively stressed – with the blue crank and with the central sphere. The shaft of the link has relatively small cross section and surface area, which makes stresses there higher than in the

contact with the sphere, where the contact area is bigger. As it can be seen, the maximum stress in the simulation was 26.465 MPa. It is lower than 40 MPa which is specified for the ABS material, used to manufacture the prototype of the joint.

However, during the experimental tests (as it will be explained in Section 4.1.1.2), the design of the experimental setup was altered and the input motor torque increased up to 5.09 Nm. The simulation was rerun with the new value of the torque, applied to the central sphere grove, which equals 9.226 Nm. This torque is equivalent to the force of 92.26 N, which is the theoretical maximum that the setup can provide with Sanyo Denki 103h8222 stepper motors. The results of the simulation are presented in Figure 85.

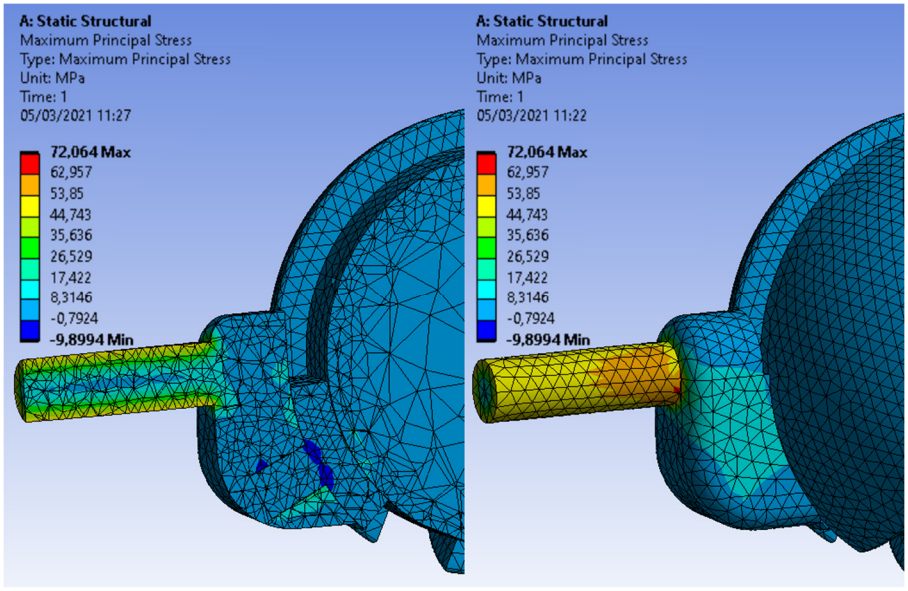

a) b)

Figure 85. The maximum principal stress in the joint (for the motor torque of 5.09 Nm): a) cross section; b) general view.

As it can be seen, the stress distribution repeats the previous simulation. The maximum stress is located in the intermediate link and equals 72.064 MPa. This value is much higher than in the previous simulation. It explains the failure of the intermediate link made of ABS. In the final variant of the experimental setup, the intermediate links were reprinted with Onyx – material, provided by Markforged Company. This material withstands the load of 71 MPa, which is lower than in the simulation, but the specified motor torque is a static holding torque, which is higher than a torque in motion that is mainly used in the haptic device force feedback system. That can explain the proper work of the mechanism during the test period.

Considering the results of both simulations, the necessity in the design improvement is well seen. The stress distribution can be improved by increasing the dimensions of the intermediate link and the blue crank. However, it should be done rationally as it can involve increasing the dimensions of the other parts and as a result, enlarging the joint itself.

3.2. Differential gear-based design

Following a similar procedure to the one associated to the joint active 2R spherical mechanism-based joint, now the kinematic analysis and quasi-static analysis of the joint differential gear-based design will be carried out.

3.2.1. Kinematic analysis of the joint

3.2.1.1. Direct position problem

The proposed joint has simple kinematics, which allows using rotation matrices in order to solve direct position problem. The design of the joint allows using only roll-pitch rotation, because the axis of rotation of the red part (see Figure 86) coincides with X axis.

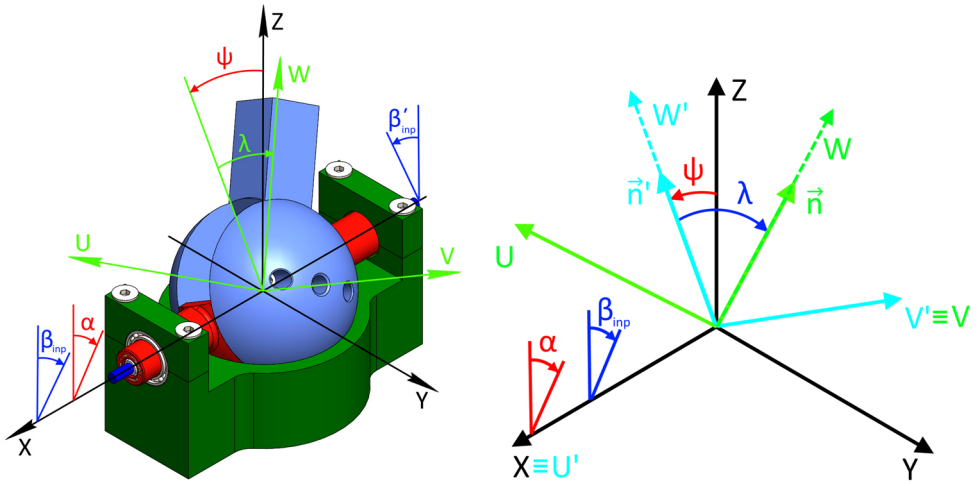

a) b)

Figure 86. Representation of the joint's rod location: a) in a CAD model; b) schematically, with the intermediate moving frame $U'V'W'$.

The rotation matrix is obtained as,

$$\boldsymbol{R}_{\alpha,U} \cdot \boldsymbol{R}_{\beta,V} = \begin{bmatrix} \cos\beta & 0 & \sin\beta \\ \sin\alpha\sin\beta & \cos\alpha & -\cos\beta\sin\alpha \\ -\cos\alpha\sin\beta & \sin\alpha & \cos\alpha\cos\beta \end{bmatrix} \tag{71}$$

The orientation of the joint's rod can be obtained by multiplying equation (71)

by the vector, representing initial vertical position of the rod:

$$[\boldsymbol{R}_{\alpha,U}][\boldsymbol{R}_{\beta,V}]\begin{Bmatrix}0\\0\\1\end{Bmatrix}=\begin{Bmatrix}\sin\beta\\-\cos\beta\sin\alpha\\\cos\alpha\sin\beta\end{Bmatrix} \tag{72}$$

It should be noted that in Eqs. (71) and (72), β is not the input angle of the actuators' shafts rotation. This angle is the angle of rotation of the rod around the *V'* axis of the moving frame. Due to the presence of the reduction gear in the joint design, angle β can be calculated as,

$$\beta=\left(\frac{Z_1}{Z_2}\right)(\beta_{inp}+\alpha) \tag{73}$$

where β_{inp} is the angle of rotation of the actuators' shafts, and Z_1 and Z_2 are the number of teeth in the pinion and in the gear, respectively. Because of the coaxial shafts, compensation of the input angle α, during the actuation of β_{inp} is necessary.

In order to obtain all the possible solutions, which are provided by the input variables, the input variables should be related to output variables.

The rod's orientation specified by the output variables can also be calculated by using the rotation matrix. As in the previous case, the first rotation occurs around the X-axis (output angle ψ, see Figure 86), then around V'-axis (output angle λ). The complete rotation matrix is,

$$\boldsymbol{R}_{\psi,U}\cdot\boldsymbol{R}_{\lambda,V}=\begin{bmatrix}\cos\lambda & 0 & \sin\lambda\\ \sin\psi\sin\lambda & \cos\psi & -\cos\lambda\sin\psi\\ -\cos\psi\sin\lambda & \sin\psi & \cos\psi\cos\lambda\end{bmatrix} \tag{74}$$

By multiplying the complete rotation matrix by the vector of the rod in its initial position, the position of the rod can be computed as follows,

$$[\boldsymbol{R}_{\psi,U}][\boldsymbol{R}_{\lambda,V}]\begin{Bmatrix}0\\0\\1\end{Bmatrix}=\begin{Bmatrix}\sin\lambda\\-\cos\lambda\sin\psi\\\cos\psi\sin\lambda\end{Bmatrix} \tag{75}$$

The relation between inputs (α, β) and outputs (λ, ψ) can be obtained using Eqs. (72) and (75):

$$n_x=\sin\lambda=\sin\beta \tag{76}$$

$$n_y=-\cos\lambda\sin\psi=-\cos\beta\sin\alpha \tag{77}$$

$$n_z=\cos\psi\sin\lambda=\cos\alpha\sin\beta \tag{78}$$

From these equations it can be seen that:

$$\psi=\alpha \tag{79}$$

$$\lambda=\beta \tag{80}$$

3.2.1.2. Inverse position problem

In order to simplify the solution of the inverse position problem, the equation (72) should be modified by dividing components of the vector $\boldsymbol{n}$ by the term $\cos\alpha\sin\beta$:

$$\boldsymbol{n}=\begin{Bmatrix}\sin\beta\\-\cos\beta\sin\alpha\\\cos\alpha\sin\beta\end{Bmatrix}=\begin{Bmatrix}\dfrac{1}{\cos\alpha}\\-\cot\beta\tan\alpha\\1\end{Bmatrix} \tag{81}$$

Now, vector we can consider vector $\boldsymbol{n}$ as $\boldsymbol{n} = \{u \quad v \quad 1\}^T$. The inputs α, β can be obtained as,

$$\alpha = \cos^{-1}\left(\frac{1}{u}\right) \tag{82}$$

$$\beta = \cot^{-1}\left(\frac{v}{\tan\alpha}\right) \tag{83}$$

From where the value of angle β_{input} can be calculated according to the equation (73).

3.2.2. Velocity equations and the workspace characterization

3.2.2.1. Kinematic Jacobians and singularities

In order to assess the workspace of the joint, the Jacobians should be obtained and investigated for the singularity conditions. Deriving the Eqs. (79) and (80) with respect to time, the velocity equations can be written as,

$$\dot{\psi} = \dot{\alpha} \tag{84}$$

$$\dot{\lambda} = \dot{\beta} \tag{85}$$

Being put into the matrix form,

$$\begin{bmatrix} 1 & 0 \\ 0 & 1 \end{bmatrix} \begin{Bmatrix} \dot{\psi} \\ \dot{\lambda} \end{Bmatrix} = \begin{bmatrix} 1 & 0 \\ 0 & 1 \end{bmatrix} \begin{Bmatrix} \dot{\alpha} \\ \dot{\beta} \end{Bmatrix} \tag{86}$$

From the equation (86) it is obvious that the Jacobian matrices are both the identity matrix, and thus, the determinant will be always one. Hence, in

theoretical workspace neither direct nor inverse singularity can exist. Therefore, the joint can move freely along the whole workspace, and this workspace will be only limited in practice by the physical constraints imposed by the geometric features of the joint's design.

3.2.2.2. Performance indices: Kinematic Conditioning Index and Global Conditioning Index

As it was done for the first joint design, the workspace of the joint was assessed making use of KCI. Due to the simplicity of the direct and inverse Jacobians of the joint, KCI equals 1 along the whole workspace, demonstrating maximum possible mobility.

As GCI is an average value of KCI along the workspace, it also equals 1.

3.2.3. The quasi-static analysis

The proposed joint has simple kinematics, which provides linear relations between input torques and output forces. The output force, induced by the red actuator can be obtained as,

$$F_r = \frac{T_r}{d_r} \tag{87}$$

where d_r is the distance between the point E (see Figure 87), and the axis of rotation of red input. d_r can be found as,

$$d_r = D_E \cos\beta \tag{88}$$

being, D_E the distance between the point E and the center of the sphere.

The output force, produced by the blue actuator, can be found as,

$$F_b = \left(\frac{Z_2}{Z_1}\right) T_b D_E \tag{89}$$

The gears, used in the joint design provide force amplification, proportional to the gear ratio, which can be profitable for highly loaded applications.

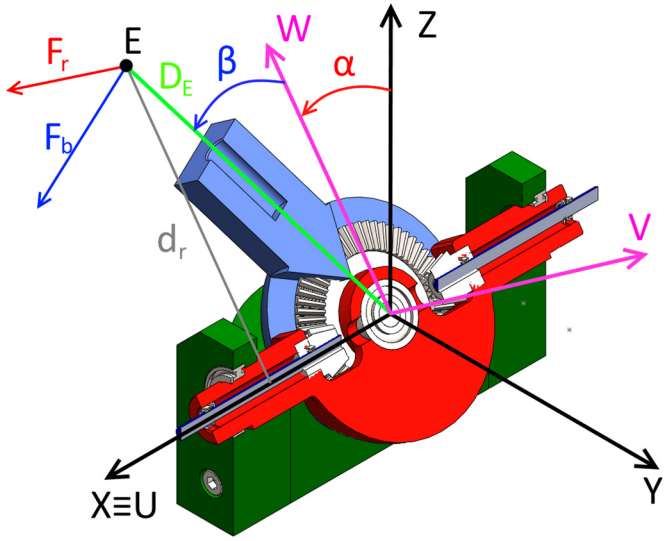

Figure 87. Force transmission in the joint.

As the two output forces are perpendicular to each other, the scalar value of the resulting force yields:

$$F = \sqrt{F_r^2 + F_b^2} \tag{90}$$

In order to identify the most loaded area in this joint, let us consider the bevel gears. It can be seen from Figure 87 that in order to place the bevel gear inside the central sphere, the gear should have relatively small module (0.5-1). It causes

the gear teeth being small and having little cross-section area, which makes it one on of the most loaded parts in the joint. From the equation (89) it can be seen that one of the force components depends mostly on the gear ratio. In theory, depending on the chosen gear ratio, the most loaded gear can be different, but in this design, the gears that are placed on the blue input shafts will always be smaller than the gear of the central sphere. It is clear that the smaller is the radius of the gear, the bigger is the force that it transmits through its teeth with the same value of torque. Thus, in this joint, the most loaded area is the teeth of the blue input shaft gears.

It can be seen from the calculation that there are no force components generated by the actuators that affect the friction force in this joint, thus it will depend only on the vector of load force $\vec{F}_L$. The friction force can be found using equation (67), where the normal force $\vec{F}_n = -\vec{F}_L$.

3.2.4. Finite element analysis

Similar to the active 2R spherical mechanism-based joint, Ansys Workbench 18.0 was used to study the load distribution qualities. As it was indicated in the previous Section, in the current design, the most loaded parts of the joint are the bevel gears, as their teeth are subjected to the high motor torque and have very compact dimensions. In addition, the teeth interact with each other along the contact line, which provides very little contact area and as a result, high pressure.

In order to simplify and speed up the simulation, only a gear and a pinion was tested. The CAD model was generated in SolidWorks 18 from the standard ISO library. The gear parameters were the set the same as the ones used for the haptic

device experimental setup, presented in Section 4.1.2.3 (module 1.5, $Z_1 = 15$, $Z_2 = 30$). Next, CAD model was imported to Ansys Workbench 18.0. The material of both gears is S45C steel, its' main parameters are presented in Table 4.

Table 4. Main parameters of the S45C steel

Mechanical Properties	Parameter value
Density	7870 kg/m^3
Tensile Strength, Ultimate	565 MPa
Tensile Strength, Yield	310 MPa
Modulus of Elasticity	200 GPa
Bulk Modulus	140 GPa
Poisson's Ratio	0.290
Shear Modulus	80 GPa

In the experimental prototype, which will be detailed in Section 4.1.2.3, the gear (Z2 = 30) is glued to the central sphere of the joint by the bottom surface and the hub. These surfaces were specified as fixed supports. The pinion (Z1 = 15) is fixed on the input shaft, which is specified as frictionless support in the simulation. The input torque of 5.09 Nm was applied to the same surface. The contact between the gears was specified as "no separation", as it is the most appropriate type of contact for the sliding surfaces. The mesh was generated with the default parameters. In the solution part, the maximum principal stress and the moment probe were selected as the examination characteristics. The moment probe is necessary to verify the simulation, as the output torque in the gear can be easily calculated as:

$$T_{out} = \frac{Z_2}{Z_1} \cdot T_{in} = 10.18\ (Nm) \tag{91}$$

The simulation provided the torque value equal 10.506 Nm, which is close to the expected value, thus the simulation should be considered as valid.

The stress distribution in the gears is presented in Figure 88.

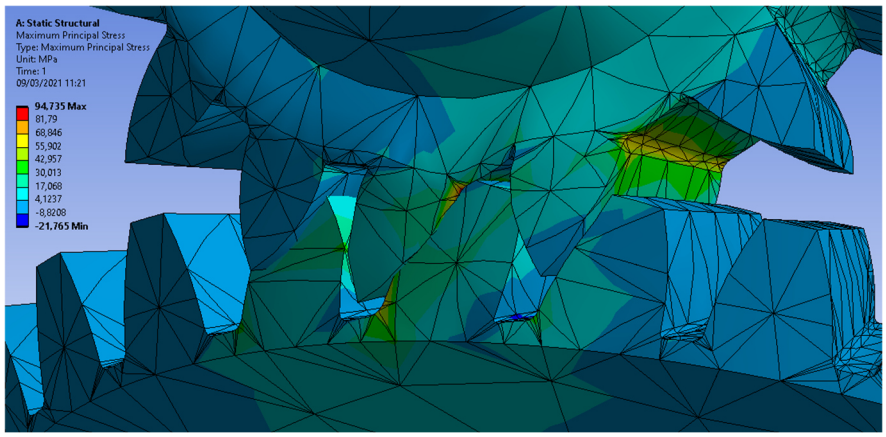

Figure 88. Maximum principal stress in the bevel gears or the joint.

According to the simulation, the maximum stress value equals 94.735 MPa. It is located in the base of the pinion's tooth. The maximum stress obtained by the simulation is significantly smaller than the maximum limit specified for S45C steel. The gears have satisfactory safety margin for the current conditions and will safely work in the haptic device prototype.

If the joint will be applied in other applications, which are subjected to a higher load, the material of the gears can be replaced or the gear module can be changed in order to improve the performance. However, increasing the gear module affects the dimensions of the elements of the joint and can lead to an increase of the joint dimensions and inertial forces.

4. Experimental setup design

In previous chapters, the most promising joint designs were chosen and their theoretical characteristics were considered. In order to evaluate their practical performance features and compare them with the theoretical ones a series of experiments should be carried out. This Chapter provides the information on the design of the experimental setups for the joint comparison. It includes the development of mechanical design, electronic hardware and software that will be used in Chapter 5 to obtain experimental data.

4.1. Experimental setup of the active 2R spherical mechanism-based joint

4.1.1. Mechanical design development

4.1.1.1. Functionality testing

In order to examine the physical characteristics of the joint, the first prototype was manufactured by 3D printing with fused deposition modeling technology (FDM) (see Figure 89a). The prototype was printed with Stratasys Dimension 1200 SST machine, produced by Stratasys. This printer uses ABS plastic with good mechanical properties. However, the precise part manufacturing is impossible with FDM technology and requires manual finishing. The clearances, which appeared during the finishing process, limited the joint application primarily to demonstrative purposes and concept testing.

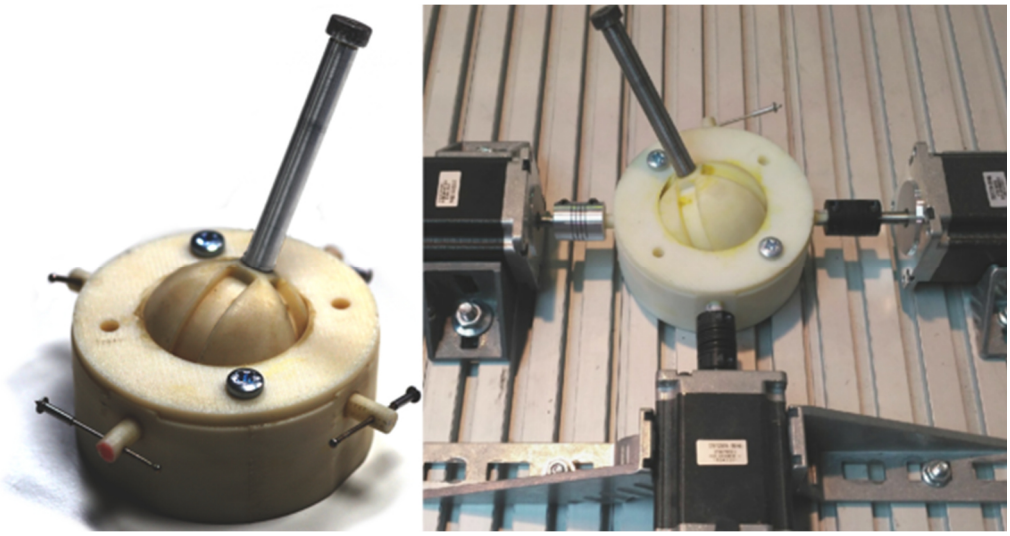

a) b)

Figure 89. Active 2R spherical mechanism-based joint prototype.

First, the joint performance was tested. In order to do that, a simple experimental setup, presented in Figure 89b, was assembled. Three Nema 23 stepper motors were used as actuators, two of which were actuating the blue cranks. In order to simplify the setup, only one motor was used for the red input actuation (the central motor). However, the actuation of both blue cranks is necessary in order to keep the mechanism under control in case it goes through the singularity position, described in Section 3.1.2.1.

4.1.1.2. Haptic device application

In order to adapt the prototype, presented in Figure 89a for haptic device application, several design modifications had to be made. The functionality testing indicated that the plastic shafts of the cranks were significantly deformed in the places where they were connected to the motors. When the joint will be

used with the force feedback, it will be exposed to high torque and proper connection of the actuators to the joint inputs will be very important. For this reason, the design of the cranks was modified, so they had 3D printed plastic body with the metal shaft connected to it (see Figure 90).

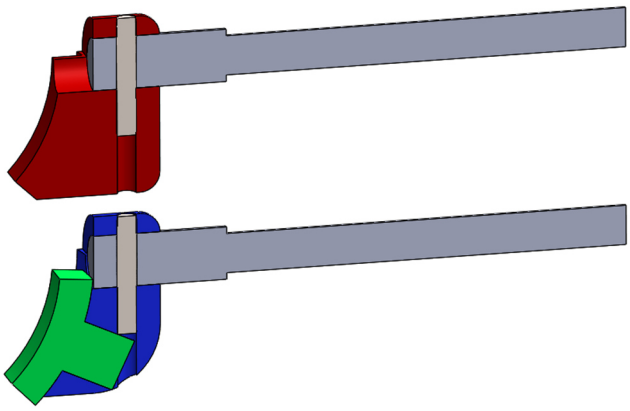

Figure 90. Modified cranks.

The modified shafts provided reliable connection and torque transmission from the actuators to the cranks. Three cranks were replaced (two blue cranks and one red crank) in order to build the haptic device experimental setup, which is schematically represented in Figure 91a. The joint 1 was placed in the center of the setup, its input shafts were connected to the absolute encoder sensors (working as potentiometers) 2 through rigid bushings. These encoders were providing the data about the input shafts angle of rotation. Special bushings 3, which were fixed on the encoder shafts, served the purpose of step-to-torque transformation and torque transmission from the stepper motors of the blue 4 and red 5 inputs through the belt drives 6. Clamp 7 is used to lock one DOF of the joint, implementing the reconfigurability in this haptic device.

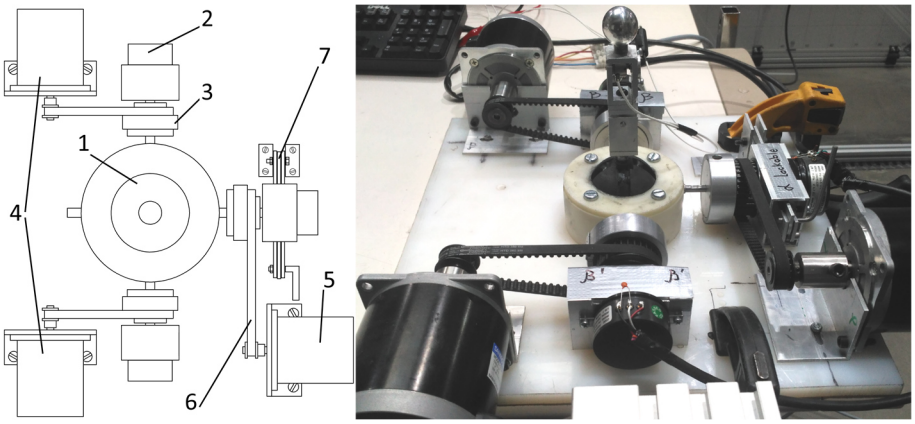

a) b)

Figure 91. Experimental setup: a) general scheme; b) practical implementation.

In order to provide the force feedback for the haptic device, the special bushings (4 in Figure 91a) that transform the steps of the stepper motor into torque were designed. Their design is presented in Figure 92. The bushing consists of outer 1 and inner 2 drums. The pulley 3, which receives the input torque from the stepper, is fixed to the outer drum. The drum also has a slot, in which a partition 4 is installed and fixed with the screw. This partition separates and supports the springs 5 that are pressing the inner drum with their other ends.

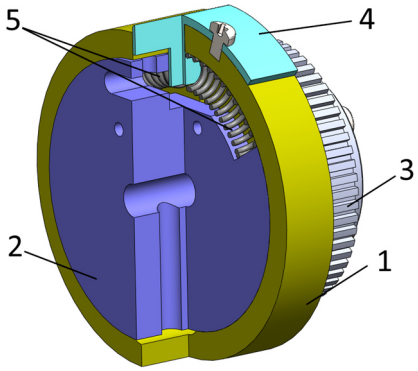

Figure 92. Steps to torque transforming bushing.

The bushing is connected to the motor (through the belt drive) from one side and to the input shaft of the joint with the other side. When the motor is rotating and the handle of the joint is fixed (the operator holds it still), the drums of the bushing start rotating with respect to each other. It leads to compression of one of the springs, which is placed between the drums. The spring creates the force that is being transmitted through the mechanism to the handle, where it is measured by the sensors and perceived by the operator.

To measure the force, generated by the force feedback system, it was decided to use ELAF-T1M-250N sensors. The range of these sensors is 0-250 N, the sensors come with built in amplifier modules, that provide output voltage 0-5V. This output range is convenient for connecting it directly to analog input pins of the Arduino board. However, the sensors can be subjected only to axial load, as the other kind of loading can lead to failure. This feature was taken into account when the design of the handle was created (see Figure 92).

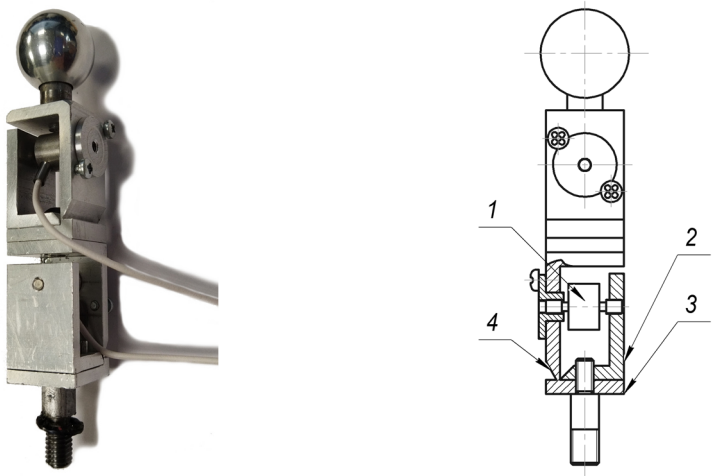

Figure 93. Handle design: a) manufactured prototype; b) blueprints.

The handle consists of two equal blocks that contain the sensors. Each block consists of two parts that are connected to the sensor 1: L-shaped 2 and Π-shaped 3. The groove 4 that is made in the Π-shaped part allows it to act as a revolute joint and at the same provides the rigidity of the structure without any clearances that can cause sensor failure. The blocks are arranged in a way that the sensors axes are perpendicular to each other.

In the initial configuration of the setup, Nema 23 motors with the maximum holding torque of 1.89 Nm were used. Considering the belt drive ratio of 1:3, the output force in the haptic device handle of 10 cm long is 56.7 N. However, the dynamic torque is typically smaller than the holding torque and depends on the settings of the motor driver. When the preliminary software was developed and force feedback tests started, it appeared that stepper motors loose steps, when the force is high. Decreasing the maximum force did not give satisfactory results. The small force is uninformative and sometimes can be confused with the friction force caused by manufacturing imperfections. In order to solve this problem, the Nema 23 stepper motors were replaced with Nema 32 Sanyo Denki 103h8222 stepper motors; with the maximum holding torque equal 5.09 Nm (measured for 6A current).

The problem of losing steps was solved, but the increased torque caused several mechanical problems and failures in the mechanism, which will be explained subsequently.

The first problem was related to the belt drive. Initially, the drive contained pulleys and belts with the T2.5 profile. It appeared that with the new torque, the belts were jumping over the teeth of the pulleys due to the flexibility of the setup or the lack of tension. It was decided to replace the belt drive with the one that

would have bigger belt profile. Considering the diameters of the shafts and the size of the original pulleys, 5M profile was chosen. The ratio of the belt transmission has changed from 1:3 to 1:2; corresponding changes were made in the software part. The new belt drive ensured stable torque transmission even with the low belt tension.

The second problem was destruction of one of the intermediate links caused by the shear force. It was cut in two pieces, one of which remained in the crank and the other one stayed in the central sphere groove (see Figure 94a). In Section 3.1.4 it was indicated, that for the initial variant of the setup, the intermediate links made of ABS have a safety margin, but in the new conditions the load is significantly increased and the failure is logical.

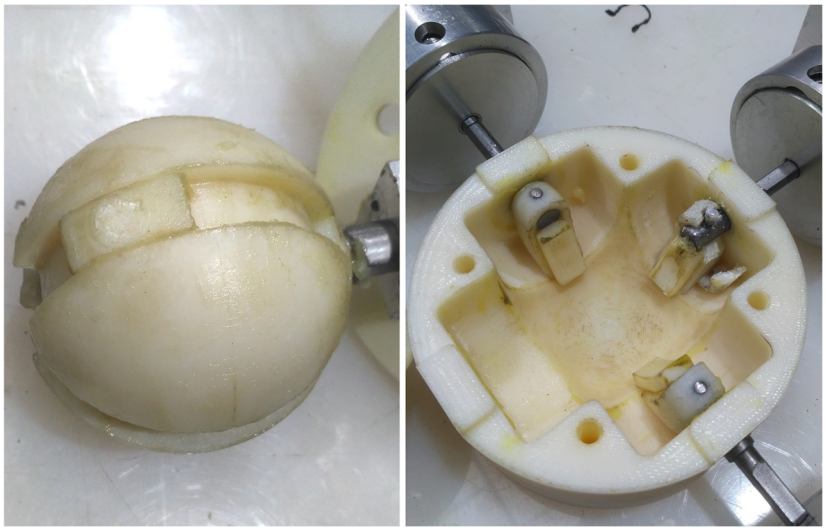

a) b)

Figure 94. Mechanical failure of the parts: a) connecting link failure; b) red input crank failure.

To solve this problem, the replacement parts were manufactured with

Markforged Mark Two 3D printer using Onyx material, which provides better mechanical properties than ABS. In addition, Markforged 3D printer provides thinner layers of material then the Stratasys printer that was used for the joint manufacturing. This feature decreases the anisotropy of the mechanical properties of the printed part.

Next, the red input crank failed in the place where the metal shaft was connected to the plastic crank body (see Figure 94b). In order to solve this problem, an aluminum replacement part was manufactured (see Figure 95).

Figure 95. Red crank replacement.

The design of the metal crank is the same as the plastic one, with the only difference that it is fixed to the shaft without gluing. This design, however, had to be modified as when it was installed, the sharp edges of the crank started cutting central sphere, which was made of much softer ABS plastic. The small chamfers, which were made initially, were not sufficient and had to be improved. After several iterations, the chamfers were replaced by filets with the radius of 1.5-2 mm, which were made manually with files and sand paper.

After the red crank replacement was installed, the tests and development of the software part was continued. After several trial runs with the force feedback turned on, one of the revolute joints, which the mechanism contained, started to

jam when handle was moved in horizontal direction towards positive side. When the joint was disassembled, it was found that the groove of the central sphere, which forms a sliding contact with red crank, was deformed (see Figure 96).

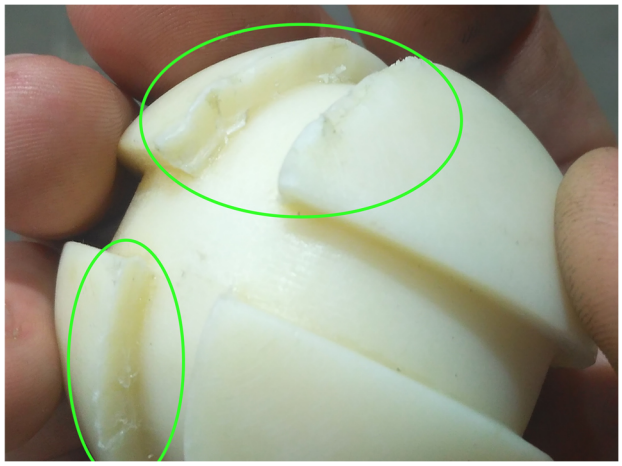

Figure 96. Central sphere deformations.

The deformations were caused by indentation of the aluminum red crank into the central sphere material, when the force feedback is on. As it can be seen, the biggest deformations are located near the place, where the groves cross. When the red crank pass that place, the contact area between the groove and the crank decreases, and the pressure rises. The aluminum crank is harder than ABS body of the central sphere, thus it deforms the surface of the groove and makes a step, which prevents the crank from sliding further and causes jamming. The solution of this problem was changing the material of the central sphere to Onyx, which has better mechanical properties.

After the central sphere replacement, the haptic device performance was satisfactory during the whole test period. The last thing added to the design was a clamp that locks the vertical direction of the handle motion. This clamp was

necessary to test the reconfigurability of the joint in the haptic device application. It provides the ability of precise pure horizontal motion. The mechanism of the clamp is presented in Figure 97.

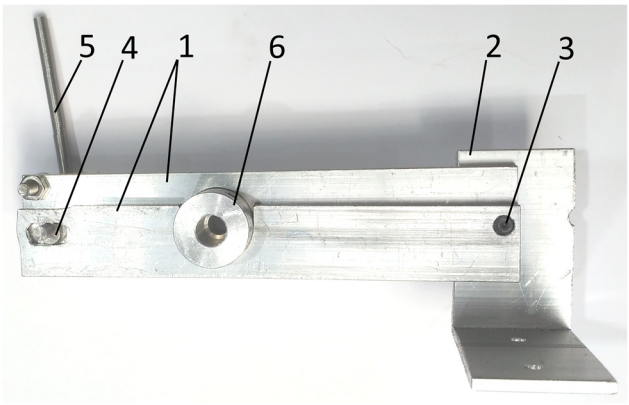

Figure 97. The clamping mechanism.

The clamp consists of three flat aluminum beams 1 (in the Figure 97 the top beam is removed) attached from one side to the L-shaped base 2 with the axle 3 and on the other side to the eccentric 4, connected to the handle 5. In the center of the beams, there is an opening for the bushing 6. This bushing connects the output shaft of the joint with the revolute encoder. The clamp is manually driven. In order to lock the vertical DOF, the handle 5 should be moved either to the left or to the right. The motion of the handle causes the eccentric 4 to turn and push the central aluminum beam towards the bushing 6. The friction between the bushing and the aluminum beams prevents the output shaft of the joint from rotation, thus locking the vertical DOF.

The completely finished experimental setup is presented in Figure 98.

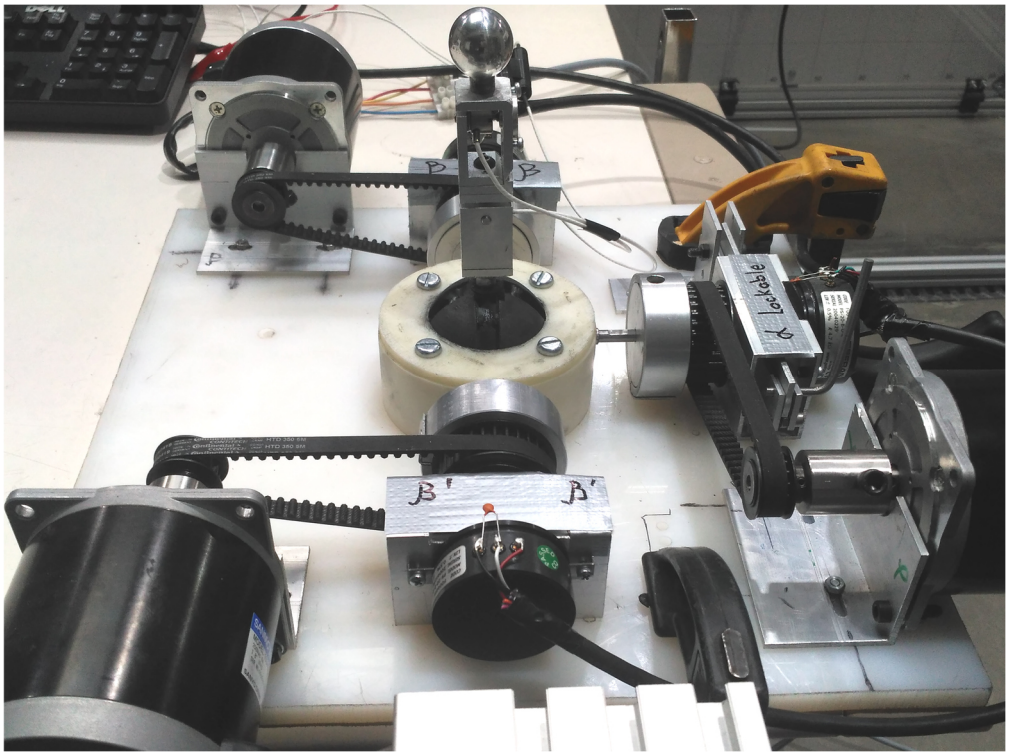

Figure 98. The compete experimental setup.

4.1.2. Software and electronic hardware development

The control of the setup was implemented with Robot Operating System (ROS) Melodic Morenia, running on Xubuntu 18.04 LTS. ROS is a modular system, which allows building custom structures from programs, called “nodes”, which communicate with each other using special protocols called “topics”. In these topics, the programs exchange messages, which carry certain information, necessary for the system to work properly.

The hardware part of the control system contained a Raspberry Pi 3B, with Xubuntu and ROS installed, and two Arduino Due boards. One of the boards was

used as a low-level controller for the stepper motors, the other one processed data from Gefran PS-20 absolute rotary encoders and the ELAF-T1M-250N force sensors. Three Geckodrive G201X stepper motor drivers drove the Nema 32 stepper motors. The drivers were powered with a 24 V 10 A power supply.

4.1.2.1. Functionality testing

To test the joint functionality, the software that was developed in the COMPMECH research group for the prototype testing was used. This software consists of two ROS nodes, one of which runs on Raspberry Pi, and the other one – on Arduino. The Raspberry Pi part has graphic user interface (GUI) (see Figure 99) and is able to execute trajectories consisting of the discrete points by reading them from *.xls file. This feature makes this ROS node reusable, as the main relationships are always contained *.xls file, which should be prepared for each particular prototype. This ROS node only sends the messages to Arduino and receives the reply about the task execution. The Arduino part receives the commands from the Raspberry Pi node, which contain the information about the steps and direction of rotation of the stepper motors. Then it executes the command (runs the steppers) and sends a message when the motors finish rotating. After that, if *.xls file contains another point of the trajectory, the next message to Arduino is sent and the cycle runs one more time. In addition, the commanding node is able to send messages manually through the graphic interface.

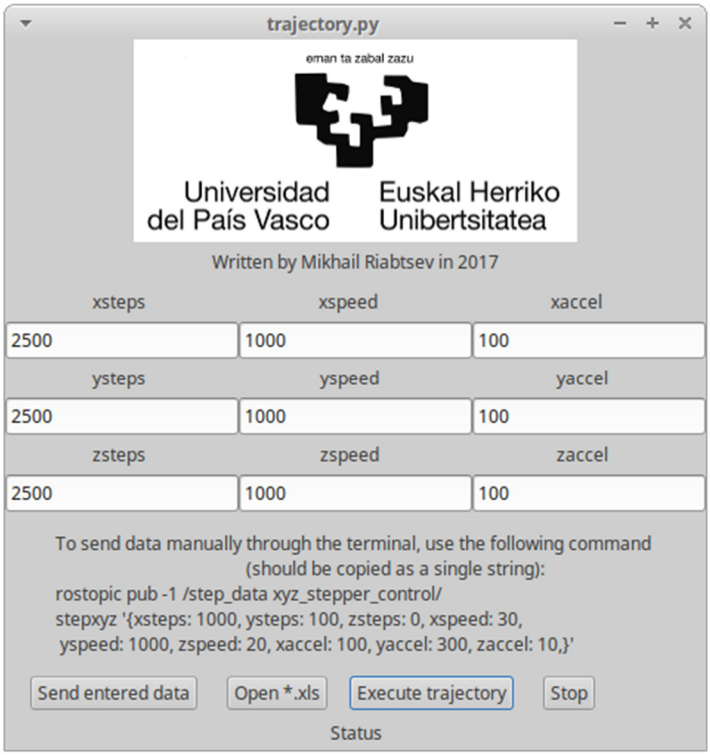

Figure 99. Graphic user interface of the commanding ROS node.

All the components of commanding ROS node were written in Python language. Glade software was used to create GUI.

4.1.2.2. Haptic device application

The haptic device application required more complex software structure, thus, special set of ROS nodes was developed. The structure of the created system is presented in Figure 100.

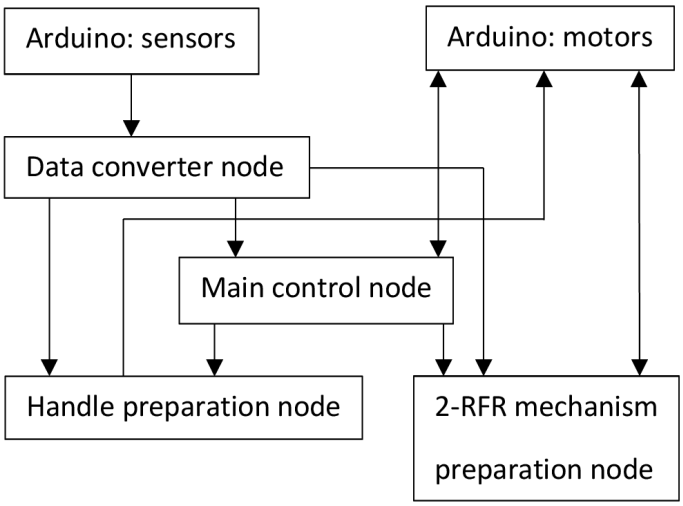

Figure 100. System structure: nodes and their connections.

The system consists of six nodes, which communicate with each other using several topics. The main node is responsible for the 2-RFR mechanism control and the haptic device operation. There is a set of nodes that serve auxiliary purposes, as transforming data (*data converter node*), preparation of the haptic device for the test (*handle preparation node*), and returning the end-effector of the controlled mechanism to the initial position (*2-RFR mechanism preparation node*). Two nodes work on Arduino: one is responsible for the sensor readings (*Arduino: sensors*) and another one for the motor control (*Arduino: motors*). Two separate Arduino Due boards are used to improve the speed of the system as the initial tests with one and subsequently two Arduino Mega boards provided unsatisfactory results. The analog-to-digital conversion process, which is used to obtain the sensor readings, is slow and limits the maximum speed of the stepper motors.

4.2. Experimental setup of the differential gear-based design

4.2.1. Mechanical design development

4.2.1.1. Functionality testing

In order to test the joint's performance, several prototypes were built. The first prototype (see Figure 101), which served mainly for demonstration purposes was manufactured using 3D printing with FDM technology. The main parts, such as the base, the sphere and the red input part, were printed with Stratasys Dimension 1200 SST. The gears of module 1 were printed with Markforged Mark Two 3D printer as it is more precise and provides better surface finish. For the blue input metal shafts were used. The pinions were fixed on the shafts with the glue and a metal pin.

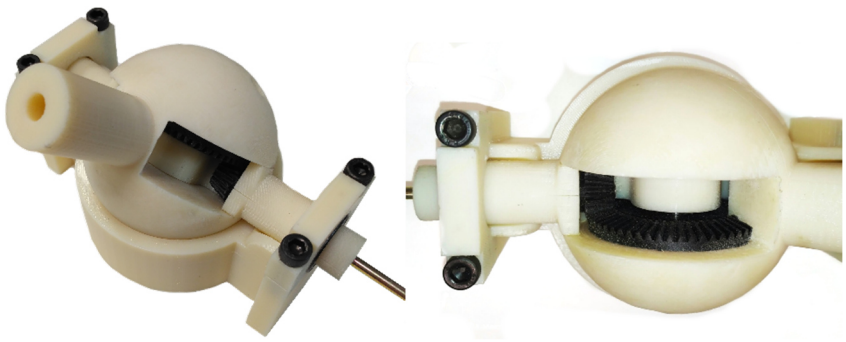

Figure 101. Demonstrative prototype.

This prototype was not intended to be applied in any mechanism, due to the mechanical properties of the printed parts. The anisotropy of the parts, in

particular the pinions can cause cracks and breakages under load or even during the assembly. However, this initial prototype served as a demonstrative one, and gave us ideas on how to achieve a functional prototype. Its experimental setup is presented in Figure 102.

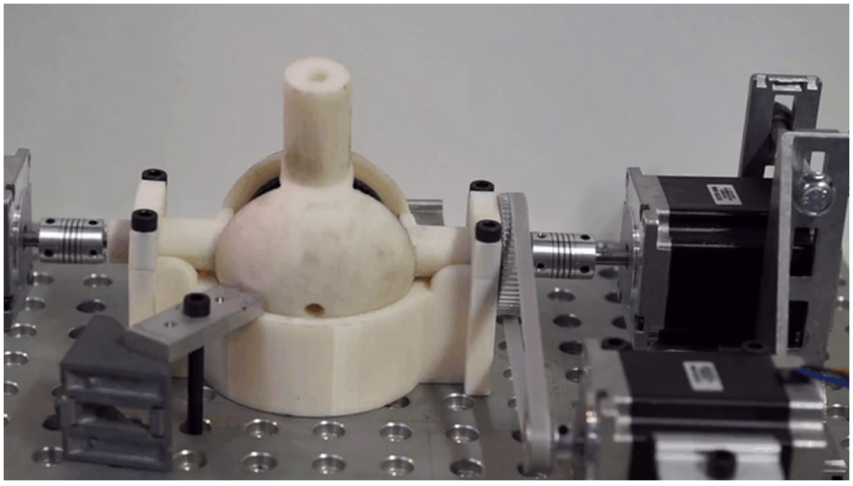

Figure 102. Experimental setup for the functionality testing.

Due to the lack of precision caused by the manufacturing approach and the manual finishing of the parts, the investigation of precision properties of the joint with this prototype is problematic. In this setup, the base part was fixed to the aluminum table and the inputs were actuated with three Nema 23 stepper motors. The blue inputs were connected directly to the stepper motor through the flexible bushing, and the red input was connected to its motor with the belt.

The electrical and software part used in the setup was the same as described in Sections 4.1.2 and 4.1.2.1.

4.1.2.3. Haptic device application

The prototype, which was made for the functionality testing, was not suitable for the haptic device application due to the problems cause by plastic gears. Considering the results of the finite element analysis, presented in Section 3.2.4, the gears of joint should be manufactured from metal. In order to speed up the design process, it was decided to use commercially available gears. In the new design, the bevel gears of the module 1.5 with $Z_1 = 15$ and $Z_2 = 30$, proposed by RS Components were applied. The elements of the joint were redesigned according to the dimensions of the new gears. The new design of the joint is presented in Figure 103.

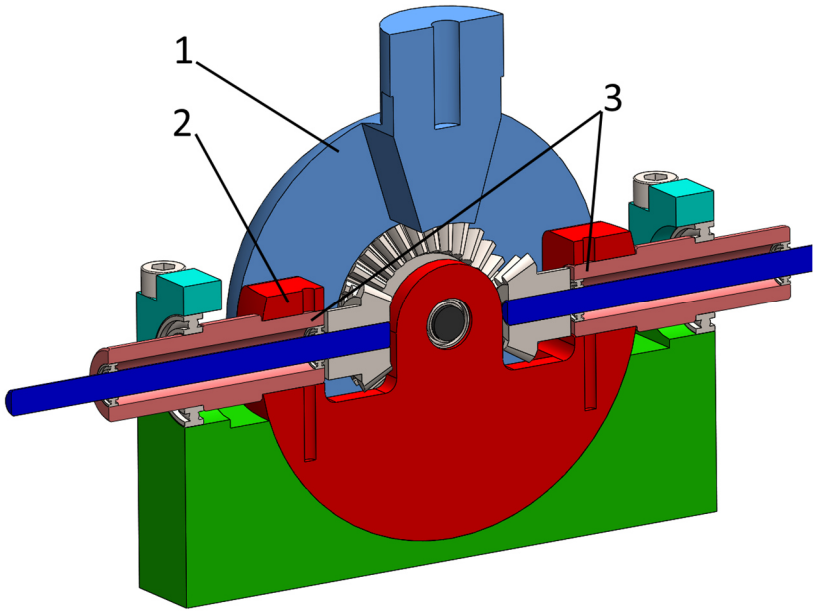

Figure 103. The joint design for the haptic device application.

The diameter of the central sphere 1 was increased to fit the gears with bigger module. The red part now consists of a 3D printed central part 2 and the hollow

shafts 3 machined from aluminum. During the assembly, the red part was broken near the bearing location (see Figure 104). The bearings were replaced with a slider bushing and the aluminum cap was machined to replace the broken fragment. The cap was fixed with epoxy and two M6 screws.

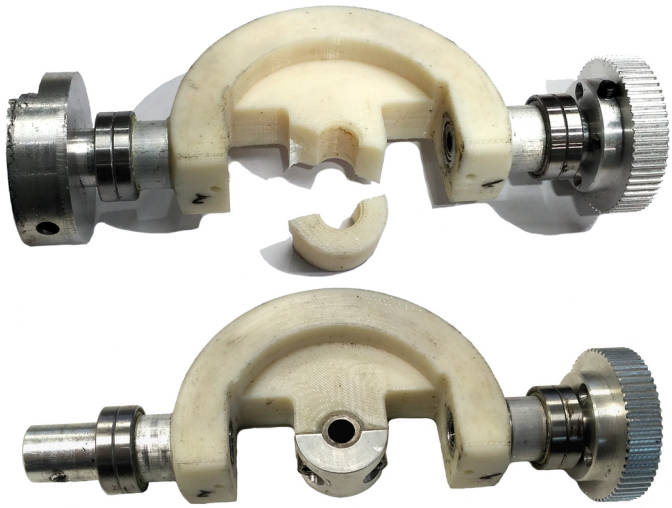

Figure 104. The part of the central sphere: broken (on top); fixed (at the bottom).

The next step was to assembly the haptic device experimental setup. The final setup is presented in Figure 105.

The setup is placed on a base of two wooden panels. In this joint, the output shafts are located higher than in the previous setup, so the joint had to be placed deeper in order to use the parts from the previous configuration. The motors of the haptic device were placed on the left side of the setup and the absolute encoders – on the right side. Both encoders were belt driven. One of the spring bushings had to be adapted to a 17 mm diameter output hollow shaft. The locking mechanism was placed in the same hollow shaft, where the actuator is attached.

The base of the setup was clamped to the table in order to prevent it from moving during the tests.

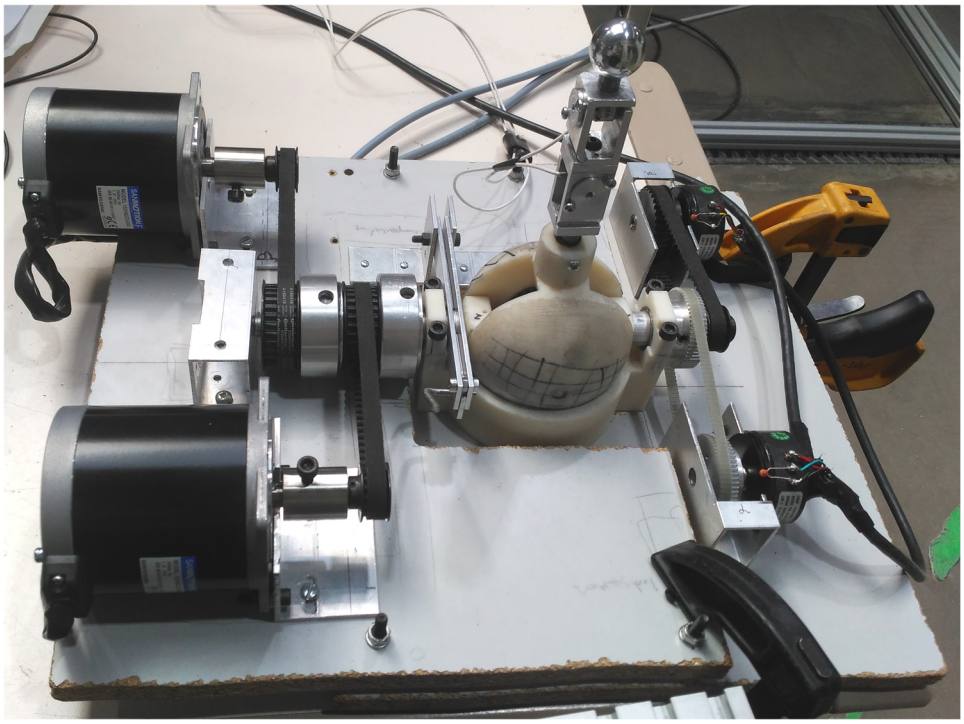

Figure 105. The haptic device experimental setup.

4.1.3. Software and electronic hardware development

For the functionality test of the haptic device in the second configuration, the same software was used. The only difference was the MS Excel file, where the trajectory was taken from. The ROS packages (see Figure 100) for the haptic device were modified according to the new configuration. The changes, which were made, were related to the joint kinematics. The main working principles remained the same.

5. Experiment and discussion

This Chapter provides methodology for the experimental comparison of the proposed joints, the experimental results, their interpretation and discussion.

The experimental part is divided into the functionality testing and the haptic device testing. The main goal of the functionality tests is the proof of concept. In these tests, the possibility of joint manufacturing, assembly and control is verified. In addition, the practical clearance compensation ability was tested. Another goal is to test the design solutions and develop better joint designs for the haptic device application tests.

Haptic device testing is intended to investigate the performance of the joints in a real application. These tests should provide objective and subjective data that will be able to identify the best joint design and the most appropriate control mode for it.

5.1. Methodology of the experiment

5.1.1. Functionality testing

Functionality testing consist of the trajectory test and the clearance compensation test.

In the trajectory test, a simple trajectory is defined for the two joint prototypes (see Table 5). It starts and ends in the vertical position, so it would be easy to make several runs in a row.

Table 5. Trajectory of the joint's rod.

Position number	1	2	3	4	5	6
Value of ψ (°)	0	0	-45	45	0	0
Value of λ (°)	0	-45	-45	45	45	0

This test is intended to verify the functionality and controllability of the joint prototype in active mode. The measurements were obtained with the Rotating Sphere Inclinometer application, which was installed on the Xiaomi Redmi 3 Pro mobile phone. This application utilizes the accelerometer of the phone to provide the information about its orientation in space. When the joint rod was in the desired position, the phone was attached to it to measure the inclination. The results will be presented in Sections 5.3.1.1 and 5.3.1.2.

The other part of the test was to check the clearance compensation ability. In active 2R spherical mechanism-based joint, the most complex task is to compensate angle λ, due to the kinematics of blue actuators. The experimental setup described in Section 4.1.1.1 allows testing of angle λ. In order to do that, the joint needs to be stopped in a certain position. The clearance is compensated by sending a command to the actuator, which is the closest to its singular position (see Section 3.1.2.1). This causes the small motion of the crank that should be enough to compensate the clearance of the mechanism. Even if the compensating actuator is in a singular position, this small motion should be able to compensate the clearance.

The clearance compensation in the differential gear-based design 3rd concept joint prototype was implemented by means of pretension in the gears. This joint can provide dynamic clearance compensation. In order to do that, before the

operation, the stepper motors of the setup were given the commands to turn to a small angle in order to eliminate the clearance between the bevel gears and create the pretension conditioned by the elastic deformation of the joint elements. After this procedure, the joint should keep the pretension in any position of the joint rod.

5.1.2. Haptic device testing

As it was presented in Section 1.2.2, 2R joints have been applied in serial haptic devices, such as those in [68]. In this case, the joints are used as part of a passive system, in which the user moves the end-effector of the serial structure [68], [69], or the end of the rod of the single joint [63]. The proposed joint designs can be applied as a haptic device, similar to the designs presented in previous references [63], [69], but with the additional advantage of reconfigurability by locking one of the joint's DOFs. This feature can provide precise motion of the remaining DOF, which in a real application can be represented as following the straight line without trajectory deviations.

In this dissertation, the haptic device based on the reconfigurable joint was developed. The device uses the joint as a "joystick" with the force feedback system. This device was used to move planar flexible 2-RFR manipulator, designed by our COMPMECH research group (http://www.ehu.eus/compmech). The base of the manipulator (see Figure 106) is a square frame made of aluminum profile with the side of 2 m. A white acrylic sheet with the coordinate mesh covers the backside of the frame. One of the actuators is located on it. The front side consists of two transparent acrylic covers that can be opened for maintenance purposes and the middle acrylic segment, to which another actuator

is attached. The manipulator has two flexible nylon rods connected to the actuators on one side and to the end-effector on the other side. Each flexible nylon bar is equivalent to two bar limbs of the common five-bar mechanism. This ultraflexible manipulator is intended to be safer for applications that involve human-robot interaction.

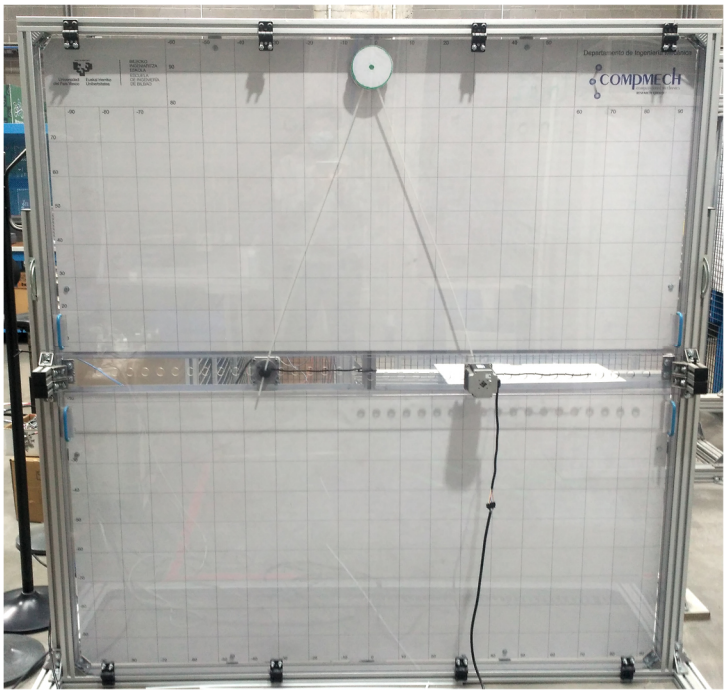

Figure 106. The planar ultraflexible 2-RFR manipulator (COMPMECH Group).

The main target is to evaluate the feasibility of using the proposed joints as a haptic device equipped with force feedback, which helps to indicate some particularly undesirable positions of the ultraflexible manipulator [109]. In this system, the actuators were attached to the red and blue cranks together with the revolute encoders in order to provide feedback in the form of counteracting forces. This feedback is necessary to control this kind of manipulator; apart from

conventional singularities, this mechanism has special positions that are caused by the flexibility of its bars. The bars accumulate mechanical energy while bending and, at some moment, this energy can be released in an uncontrollable way. The exact moment of the accumulated energy release cannot be visually predicted and needs to be previously indicated. When the mechanism approaches one of these positions, the forces created by the actuators (that resist the attempts of the operator to move the rod of the joint further) get higher.

Two mechanism control scenarios were considered: direct position control, and velocity control. In the direct position control scenario, the position of the rod of the joint directly corresponds to the position of the end-effector of the manipulator. This control scenario is intuitive for the operator, however, the resolution in this mode would be highly influenced by the operator's skills and abilities. The second scenario is to control the velocity of the end-effector in a certain range. In this case, the operator controls the velocity components (X, Y) by the inclination of the rod in a proper direction. This scenario provides an improved accuracy because it does not require high precision and sensitivity from the operator.

5.1.2.1. Experimental tasks planning

The ability to control a haptic device is subjective and depends on the variety of skills and personal qualities of the operator. In order to minimize the influence of each particular person, normally haptic device evaluation involves participation of a large number of people. In different research, the number of subjects varies from 10 [110] to more than 50 [111]. The participants are asked to perform objective and subjective tests [112]. The objective tests typically are

related to the parameters which are convenient for the numerical assessment. The example of such tasks can be repeating the trajectory and following some "leader". In these tasks, the evaluation criteria can be the accuracy of displacement (deviation from the desired parameters), velocity and time. The subjective tests involve using questionnaires in order to register the personal experience of testing the device for each of the participant. In research dedicated to haptic devices such well-known tools as National Aeronautics and Space Administration Task Load Index Assessment (NASA TLX) [113] and After-Scenario Questionnaire – International Business Machines (ASQ IBM) [114] are used. In these tools, the test subjects are asked to fill a form, which contains several questions. To do this, the person should mark the appropriate part of the scale (from positive to negative), which represents the question. The result of these tests is quantitative and it is easy to analyze with any mathematical approach. For both objective and subjective results, different ways of statistical analysis were proposed. The most used methods are Analysis of Variance (ANOVA) [115]–[123], Mann–Whitney U [116], [124]–[127] and Friedman [128], [129].

Based on this information, the arrangement of the experiment can be made. The test group should involve from 15 to 20 subjects, who will be asked to control 2-RFR ultraflexible mechanism using two modes: position control and velocity control. The testers should be asked to fill NASA TLX questionnaire, as it is more informative than the ASQ. ASQ contains only three general questions, while NASA TLX contains six more specific questions that can indicate the hardest part of the task.

For each of the modes the following tasks should be executed:

Task 1: Finding the workspace borders and singular positions with the force feedback turned off.

Task 2: Finding the workspace borders and singular positions with the force feedback turned on.

Task 3: Execution of the defined trajectory.

Task 4: Following the leading object within a defined distance.

In order to perform the four main tasks, the experimental setup was equipped with a projector, which projected an image on the mechanism. The scheme of the setup and its practical implementation are presented in Figure 107. The tester 1 is holding the handle of the haptic device 2 and is looking at the ultraflexible 2-RFR mechanism 3, where the projector 4 projects the image, corresponding to the current task (the projector was not used in a trial run shown in Figure 107b).

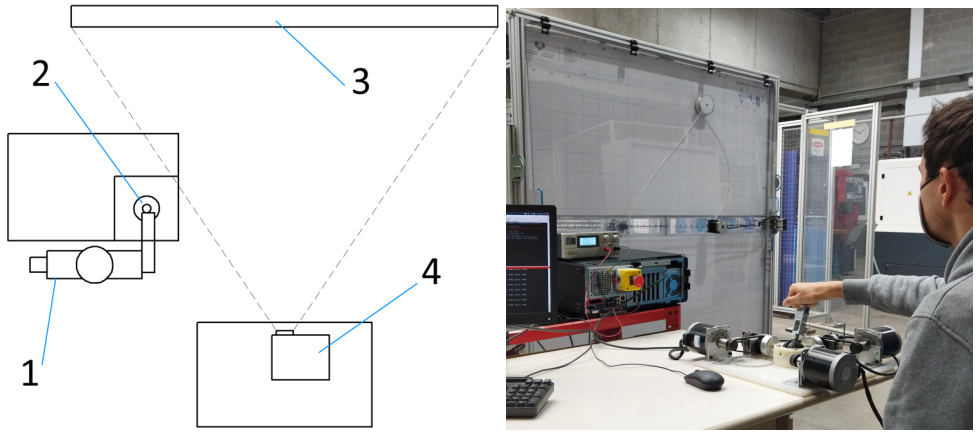

a) b)

Figure 107. The experimental arrangement: a) a scheme of the setup (top view); b) practical implementation.

The first and the second tests are intended to evaluate the efficiency of the force feedback system, in order to understand how much help it can provide to the human operator. In this task, the tester is asked to reach the workspace limits, at first using visual feedback and intuition, then using force feedback system. In order to decrease the amount of time needed for these tests (as the workspace in theory has infinite amount of positions), several directions of motion are proposed to the operator (see Figure 108). The tester has to choose one of the blue lines and one of the red lines and move the end-effector along them until it reaches the border of the workspace (the end-effector will stop). After reaching the border, the operator should move the end-effector in an opposite way, following the same line. When the border will be reached, the line should be changed, or, if both lines were passed, the test is finished. The tester is asked to report how successful he/she was in predicting the border of the workspace. The grade should be put in the "Performance" part of the NASA TLX form.

The other purpose of these tasks is getting used to the haptic device controls before more complex tasks 3 and 4, which require precise or/and fast actions of the operator.

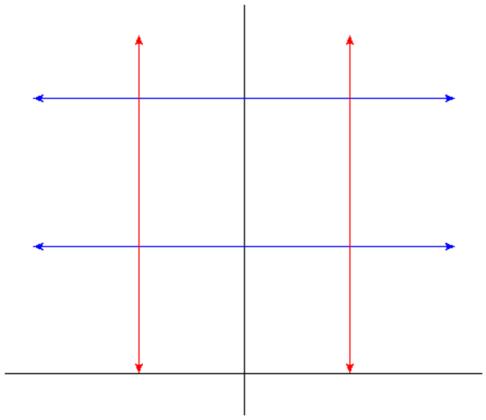

Figure 108. The image projected on the mechanism during the first test.

During the third task, the main target is to evaluate the accuracy of the system. The tester was asked to follow the trajectory, which was projected on the backside frame of the mechanism (see Figure 109).

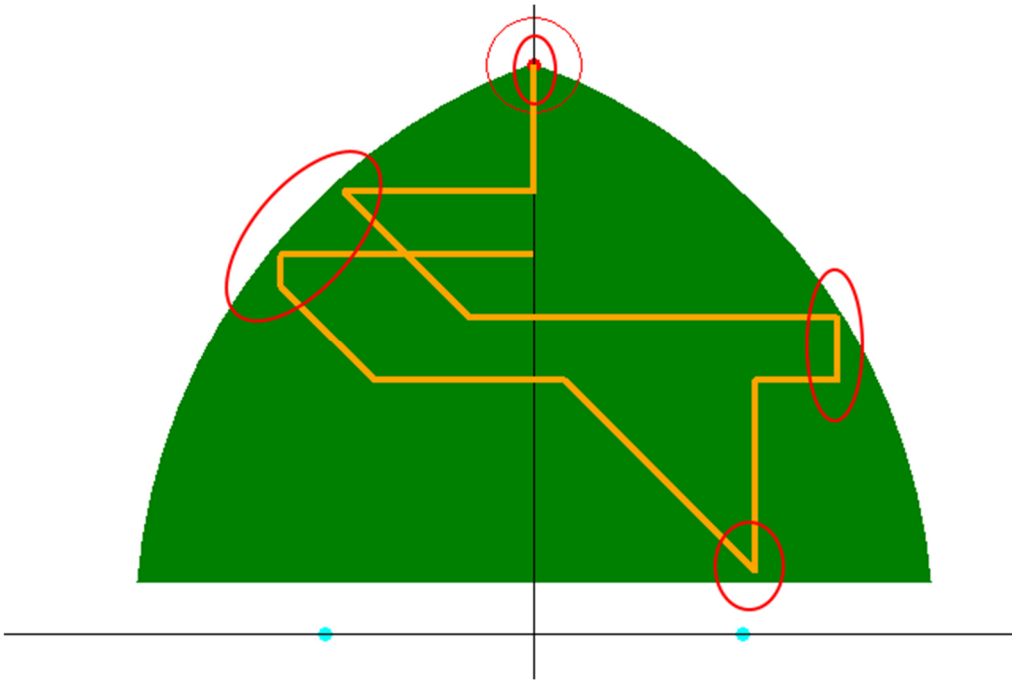

Figure 109. The trajectory (in orange), corresponding to the task three.

In Figure 109 the trajectory is represented in orange; the workspace (in green) is not shown during the test, so the parts of the trajectory, which were close to the border (indicated with red ovals), were indicated only with the force feedback. The trajectory starts from the initial position (0, 90) cm and finishes at (0, 60) cm. The tester is asked to follow the trajectory as precise as possible, the time is not measured. The task was filmed in order to grade it later. If the end-effector of the 2-RFR ultraflexible mechanism was moving more than 6 cm away from the trajectory line, it was considered as a trajectory deviation. In addition, if the tester was going through the “shortcuts” near the angles of the trajectory, it also

was counted as a deviation. During the grading, the amount of trajectory deviations was counted and put in a data table, which later was used in statistical analysis.

In the fourth task, the operator was asked to follow a leading object within a certain distance. This test is intended to estimate the ability to respond to variable environment. The precision is the main criterion of the assessment. The leading object in this task was a red dot, surrounded by the red circle, which was moving along the trajectory, presented in Figure 110 in orange.

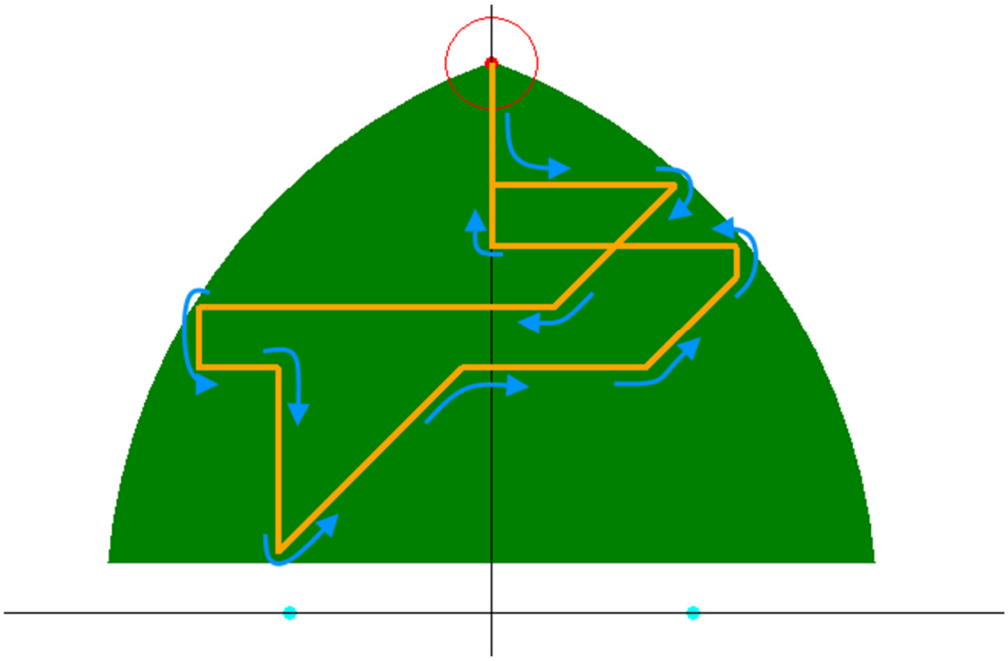

Figure 110. The trajectory of the leading object (in orange), corresponding to the task four.

The trajectory in this task is the same as in the task three, but mirrored around the Y-axis. The trajectory was altered, so the testers will not be able to memorize it. When the test is running, the operator cannot see neither the trajectory, nor the

workspace. The goal of the task is to keep the center of the end-effector within the red circle of the leading object. The radius of the circle is 10 cm. The leading object can move with different velocity (1-4 cm/s), which is always smaller than the maximum velocity on the particular part of the trajectory (in the velocity control mode). For instance, the leading object cannot move along the diagonal parts of the trajectory faster than 2 cm/s, because due to the joint workspace restrictions, the maximum speed of the end-effector in these parts can be only 3 cm/s. The starting and ending points of the trajectory are the same – (0, 90) cm. The direction of motion is indicated in Figure 110 with cyan arrows.

As in the task three, this task was filmed for further grading. Here the number of times, when the end-effector left the red circle was counted. The results were put in data table for further study.

In a perfect case, there should not be any deviations in the Tasks 3 and 4. The more the deviation number is, the worse the corresponding task is executed. In order to standardize the results, it was decided, that as in the NASA TLX form, the maximum score of the Tasks 3 and 4 would be equal 20, which is considered as a complete failure. This score was also put in the cases when the number of deviations exceeds 20.

The tasks 3 and 4 provide the most complete information on the performance of haptic device designs as they are testing the setup with exercises that correspond to practical tasks. They are executed with the force feedback and present its performance in complex environmental conditions. Thus, these tasks are the most representative and they will be used for joint performance comparison.

Aside of these tasks, the possibility of locking one DOF of the joint and using it

for the precise straight motion was tested. However, this test does not require a test group, as it gives a definite result (positive or negative), thus it was not included in the list of tasks and was carried out separately.

5.1.2.2. Statistical tools

The haptic device testing produces significant amount of data. For instance, NASA TLX form contains six different parameters, thus assuming that we have 17 testers doing 4 tasks in two control modes, the full set of data for one joint test will be: $6 \times 17 \times 4 \times 2 = 816$. This would be the full number of different values that have to be processed. In order to process this data set and obtain a definite result, statistical analysis was used. The statistical analysis should be used because we cannot rely only on sample mean to assess the test results. The data sample in our case is the outcome (the set of values of a selected parameter) of the particular task of the whole group of testers. The mean value does not provide enough information about the sample. One of the samples (especially in case of the small sample sizes) can have bigger mean than the other one because of a couple of accidental outlying values. The statistical tools can verify if there is a real significant difference between the sample means, or it is just an error caused by chance.

First, it is necessary to identify if the studied samples are normally distributed or not. Depending on the result, parametric or non-parametric statistical tools should be applied. There are two main ways to identify if the data sample is normally distributed: graphical and numerical. The simplest way to check the data is to build an actual distribution graph, and then visually compare it with a normal distribution curve. However, on a small sample sometimes it can be hard

to identify if the actual distribution curve is similar to a normal one. In this case, a numerical approach can be used. One of the most widely used is Kolmogorov–Smirnov test (KS-test) [130]. However, some sources [131], [132] recommend using the Shapiro-Wilk test as the one providing the biggest statistical power. In this dissertation, the Shapiro-Wilk test was used. In this test, the null hypothesis is that the data sample is normally distributed. The test is defined as,

$$W = \frac{\left(\sum_{i=1}^{n} a_i x_{(i)}\right)^2}{\sum_{i=1}^{n}(x_i - \bar{x})^2} \tag{92}$$

where: $x_{(i)}$ is the i-th smallest value of the sample (not to confuse with x_i, the i-th value of the sample); a_i is a coefficient, normally taken from the statistical tables; $\bar{x}$ is the sample mean.

If the obtained value W is bigger than the critical value for this sample size, the null hypothesis is rejected and the sample is considered not being normally distributed.

The calculations related to Shapiro-Wilk test were done in Microsoft Excel and later verified using the www.statskingdom.com website, Shapiro-Wilk test section [133].

After the normality check, the proper statistical tools can be identified (see Table 6).

Table 6. Analog of Parametric and Nonparametric Tests [134].

Number of samples	Parametric tests	Non-parametric tests
One sample	One sample T-test	Sign test Wilcoxon's signed rank test
Two-sample	Paired T-test	Sign test Wilcoxon's signed rank test
	Unpaired T-Test	Mann-Whitney test Kolmogorov–Smirnov test
K-sample	Analysis of variance	Kruskal-Wallis tests Jonckheer test
	Two way analysis of variance	Friedman test

According to the tasks and goals presented in Chapter 5, we need to compare the data produced by tasks one and two, in order to assess the performance of the force feedback system of the haptic device. This implies comparison of two data samples provided by the same testers. In this case, according to the table 6, depending on the sample distribution, paired T-test or Wilcoxon's signed rank test should be used. The same type of tests should be used for identifying the best control mode, as there are two samples (we are considering tasks with different control modes in pairs), and the data samples are connected with each other by the testers. For the identification of the best joint design, the results of tasks shall also be analyzed in pairs, but there will be no connection between the samples, as different people passed the tests. In this case, unpaired T-test and Mann-Whitney test should be used.

5.1.2.2.1. Paired T-test

In case the data sample is normally distributed, a paired (dependent) or unpaired (independent) T-test is used. Both types of the T-test compare the mean values of two data samples in order to define if there is a significant difference between them. The null hypothesis in the T-test is that there is no difference between the samples. It can be rejected if the result, provided by the T-test is less than a value, obtained for a certain probability number α. The conventional value of α is 0.05 [135] is considered to be small enough to define statistical significance.

In order to obtain the result of a paired T-test, several calculations should be carried out. First, the difference of each paired data (x_i and y_i) should be found:

$$d_i = x_i - y_i \tag{93}$$

Next step is calculating the mean of the difference, $\bar{d}$ and the standard deviation of the differences, S_d:

$$S_d = \sqrt{\frac{\sum |d_i - \bar{d}|^2}{n}} \tag{94}$$

where, n is the sample size.

After that, the standard error can be obtained as follows:

$$SE(\bar{d}) = \frac{S_d}{\sqrt{n}} \tag{95}$$

Finally, the T value can be calculated as,

$$T = \frac{\bar{d}}{SE(\bar{d})} \tag{96}$$

Knowing the degree of freedom of the sample $(n-1)$ and the probability value $\alpha = 0.05$, it is possible to find the critical value using statistic tables. If this value is bigger than T, the null hypothesis can be rejected.

5.1.2.2.2. The unpaired T-test

The unpaired T-test can compare samples that have different sizes. For both samples the means ($\bar{x}_1$, $\bar{x}_2$) and the standard deviations should be calculated:

$$S_1 = \sqrt{\frac{\sum|x_{1i} - \bar{x}_1|^2}{n_1}} \tag{97}$$

$$S_2 = \sqrt{\frac{\sum|x_{2i} - \bar{x}_2|^2}{n_2}} \tag{98}$$

Next, pooled standard deviation should be calculated as,

$$S_p = \sqrt{\frac{(n_1 - 1)s_1^2 + (n_2 - 1)s_2^2}{n_1 + n_2 - 2}} \tag{99}$$

The standard error can be calculated as follows,

$$SE(\bar{x}_1 - \bar{x}_2) = S_p \sqrt{\frac{1}{n_1} + \frac{1}{n_2}} \tag{100}$$

Finally, it is possible to calculate T-statistics:

$$T = \frac{\bar{x}_1 - \bar{x}_2}{SE(\bar{x}_1 - \bar{x}_2)} \tag{101}$$

As in the paired T-test, the obtained T value should be compared with the critical value from the statistic tables. If T is less than the critical value, the null hypothesis is rejected and there is a significant difference between the samples.

In order to calculate the T-test, Microsoft Excel was used. It has a built in function *T.TEST(array1,array2,tails,type)*, which can calculate both paired and unpaired T-test. The function provides the result as a probability, which can be directly compared with $\alpha = 0.05$. If the result is smaller than α, the null hypothesis is rejected. In order to verify the result of the calculation, the T-tests were also calculated online, using the Statistics Kingdom website in the paired and unpaired T-test sections [136], [137].

5.1.2.2.3. Wilcoxon's signed rank test

Wilcoxon's signed rank test is a non-parametric alternative to the paired T-test. Similar to the T-test, it compares the means of the samples with the null hypothesis that there is no significant difference between the means. In order to obtain the result, several calculations should be carried out. First, the difference d_i and the difference sign sd_i should be obtained as,

$$d_i = |x_{2i} - x_{1i}| \tag{102}$$

$$sd_i = sgn(x_{2i} - x_{1i}) \tag{103}$$

where, x_{1i} and x_{2i} are the paired sample data, and sgn is the sign function, which

returns 1 or -1. If the difference equals zero, the data pair should be excluded from the calculation. After that, the data pairs should be arranged in ascending order to assign rank R_i to each pair. The rank "1" is assigned to the pair with the smallest difference d_i. The next ranks are assigned in ascending order with the step of one. If several data pairs have the same values of d_i, they share the average rank. Then, the W^+ and W^- parameters should be calculated as,

$$W^+ = \left| \sum_{d>0} d_i \cdot R_i \right| \tag{104}$$

$$W^- = \left| \sum_{d<0} d_i \cdot R_i \right| \tag{105}$$

Knowing the size of the sample n, and the desired probability α, it is possible to find a critical value for the current test. After that, the smallest W value should be compared with the critical value. If the obtained W value is smaller than the critical value, the null hypothesis can be rejected.

The calculations of the Wilcoxon's signed rank test were made in Microsoft Excel, as it is provides convenient data arrangement and has built in ranking function (*RANK.AVG (number, ref, [order])*). The results of the calculations were verified with the Statistics Kingdom website in the Wilcoxon's signed rank test section [138].

5.1.2.2.4. The Mann-Whitney U-test

The Mann-Whitney U-test is a non-parametric analog to the unpaired T-test. Its null hypothesis is that the two data samples were taken from the same

population. To carry out the test, a sequence of manipulations with the data should be done.

First, the data of both data samples should be put together and arranged in ascending order. While doing this, it is important to mark the data, so it will be possible to know to which sample it belongs. Next, as in Wilcoxon's signed rank test, the data should be ranked. After that the U values can be calculated for both samples as follows,

$$U_1 = R_1 - \frac{n_1(n_1 + 1)}{2} \tag{106}$$

$$U_2 = R_2 - \frac{n_2(n_2 + 1)}{2} \tag{107}$$

Knowing the size of two samples (n_1, n_2) and the probability α, a critical value can be found in the statistical tables. It should be compared with the smallest of the U values, and if the U value is smaller than the critical value, the null hypothesis can be rejected.

The same as in Wilcoxon's signed rank test, Microsoft Excel was used to carry out the calculations. The verification of the results was made using the Statistics Kingdom website, in the Mann-Whitney U-test section [139].

5.2. Experimental progress

Due to the COVID-19 restrictions, the amount of participants in the haptic device testing was limited. In active 2R spherical mechanism-based joint tests the tester group consisted of 17 participants and in differential gear-based design test the

amount of testers was 19. It also should be noted that nine people have participated in both tests. Most of the testers were students and professors from the Mechanical Engineering Department of the University of Basque Country UPV/EHU.

The single test normally took 45 ± 10 minutes, including the instructions. Before the beginning of the test, the people were asked to sign up in the list of participants, and after the test, they had to give the feedback about the control mode that they preferred. After the differential gear-based design testing, the haptic device operators were also asked to give a personal feedback about the joints, selecting the one they preferred in the case they have been involved in both experiments.

The tasks 3 and 4 of each control mode were filmed. The testers did not appear in the video in order to keep anonymity. In order to differentiate the videos later, the notes with the number of the task, the name of the control mode and the number of the participant were placed on 2-RFR ultraflexible mechanism.

After each test, the handle of the haptic device and the surfaces, which were in contact with the testers hands were treated with 70% alcohol spray in order to prevent spreading of COVID-19. The testers also were provided with the disinfecting gel for the hand treatment.

During the tests, there were no major failures in the haptic device or the 2-RFR ultra flexible mechanism. The most common problem was detachment of a flexible bar from the end-effector of the mechanism, which occurred in some cases during the operation in the position control mode. There are two reasons for that. First, the bars did not have rigid fixation in the end-effector; they were

fixed mainly with high friction. The second reason is the high speed of the end-effector in the position mode and the inertia of the end-effector. As a result, in some cases the inertia forces overcame the friction forces in the bar fixation and it led to the bar detachment. Another problem was going beyond the workspace in the task 1 of the position mode in both joints. It is also caused by inertia of the end-effector, when it moves down rapidly. In these cases, the force feedback is disabled and it cannot help decelerating the handle near the workspace border. Thus, the end-effector goes in the lower part (negative Y) of the 2-RFR ultra flexible mechanism.

After finishing both joint tests, the experimental program was considered to be successfully completed. Subsequently, the results from this testing will be exposed and discussed.

5.3. Experimental results and discussion

5.3.1. Functionality testing results

5.3.1.1. Active 2R spherical mechanism-based joint

At first, the joint prototype was subjected to the repeatability test, described in Section 5.1.1. The average deviation from the trajectory, presented in Table 5 was $\pm 3°$. However, the measurements with the phone gyroscope are not very precise and depend on how the phone is attached to the rod, when each measurement is made. In addition, minor deviations can be considered satisfactory for the prototype, which was manufactured with 3D printing. Taking into account the error, caused by measurement method, it can be said that the

controllability of the joint within its practical workspace was confirmed. The duplication of the blue cranks ensures the workability in the singular positions, described by the equations (43) and (44). However, the clearances, caused by manual part finishing, influence the repeatability of the joint rod positions.

In order to compensate the clearances, this joint should have four actuators and dynamic clearance control. In this setup, only three motors were used along with the simple test software, which made continuous clearance compensation impossible. However, discrete clearance compensation is available with blue cranks in manual control mode. In order to do that, the joint needs to be stopped in a certain position. As it was described in Section 3.1.2.1, there is one singular position for each of the blue actuators. When the joint is actuated, one actuator always stays in control and the other one follows it, as it is approaching to the singular position. The clearance is compensated by sending a command to the actuator, which is following the main one. This causes the small motion of the crank that is enough to compensate the clearance of the mechanism. Several tests have indicated that this method is valid for the different positions, including the singular ones. However, the control command, which was sent to the compensating actuator was different in every position and had to be adjusted manually. The difference in the compensation command could be caused by the manufacturing method, as manual finishing cannot provide uniform surface shape, and the clearances in the different parts of the mechanism become unpredictable. In addition, the clearance in the red crank remained uncompensated, because only one motor was used to actuate the red crank.

As a conclusion, it can be said that the tests of the prototype have completely proved the functionality of the joint in functionality testing. Nevertheless, it

should be noticed that, if a higher load is applied, then the design should be optimized. During the test, it was found that the plastic input shafts have been deformed in the place of connection with the flexible metal bushings. The results of the finite element analysis calculation, presented in Section 3.1.4, did not present significant deformation of the input shaft. However, the real attachment of the shaft is different from the idealized version that was specified in the simulation. Considering the small load on the joint during the functionality tests, the shafts should be redesigned using stronger material, as the loads in the haptic device application will be much bigger.

5.3.1.2. Differential gear-based design

At first, the prototype of the proposed joint was subjected to a clearance compensation procedure, described in Section 5.1.1. It was done in order to carry out the repeatability test with the compensated gear clearance for more precise results. Following the proposed trajectory, the joint rod average deviation was $\pm 2°$. These results do not differ much from the ones obtained by the previous joint. The possible cause is the measurement error, as the phone was not fixed on the rod, but was attached there only to make a measurement. In addition, the clearance was still present in some positions due to manufacturing defects of 3D printed bevel gears. The gear module appeared to be too small to provide satisfactory gear quality. It was decided that for the haptic device prototype, the gear should be replaced with the metal one in order to provide uniform contact between the pinions and ensure the joint reliability. In addition, according to the results of the finite element analysis, presented in Section 3.2.4, maximum stress in the gear is 94.735 MPa, which exceeds the maximum stress, specified for Onyx material (71 MPa). Thus, the gear had to be replaced in order to work

properly in the haptic device testing.

The functionality testing have verified the concept of differential gear-based design joint controllability and clearance compensation ability. However, the design should be adapted for using metal gears for uniform clearance compensation and withstanding higher loads.

5.3.2. Haptic device test results

After the tests, the NASA TLX forms were processed and data was transferred into Microsoft Excel tables to be able to carry out proper data analysis. In Appendix A of this Thesis, the data from NASA TLX forms are presented. In Appendix B, task 3 and 4 score is presented. The tester comments are placed in Appendix C, and in Appendix D, the distribution graphs are introduced.

5.3.2.1. Reconfigurability test results

Aside of the tester tasks, the reconfiguration ability was tested on both joints in both control modes. The red actuator was disabled and the red input shaft was locked with the special clamp (see Section 4.1.1.2). This feature provided the ability of a precise motion along the horizontal axis. The test started in a normal position (end effector at (0, 90) cm). Then, the end-effector of the controlled mechanism was moved lower to a random position, where the clamp was locked. In this position, the end-effector was moved in a horizontal direction at first towards one border of the workspace, then to other. Such functionality was tested both with and without the force feedback. In all cases, the clamp provided successful fixation of the shaft, making the handle move straight with no

disturbances. The precision of the motion was confirmed by both visual observation and logs of the topic provided by *data converter node* of ROS (see Figure 100). In that topic, the coordinates of the end-effector are published and it is possible to see, if Y component is constant. The performance of the reconfigurability function was tested both in velocity and position control mode. The results did not indicate any significant difference aside the distinctions in the working modes themselves that will be described in subsequent sections.

5.3.2.2. Normality check results

Based on the results, presented in Appendix A, the distribution graphs were created for visual sample normality check. Some of the graphs present clearly normal distribution; an example is presented in Figure 111.

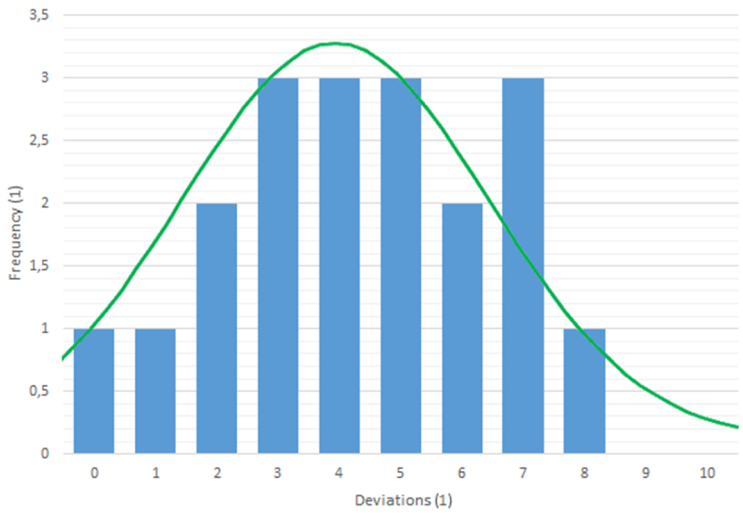

Figure 111. Distribution of the deviation numbers (in blue), velocity control mode, task 4, Differential gear-based design joint; normal distribution curve (in green).

Other sample distributions are obviously, not normal, see example in Figure 112.

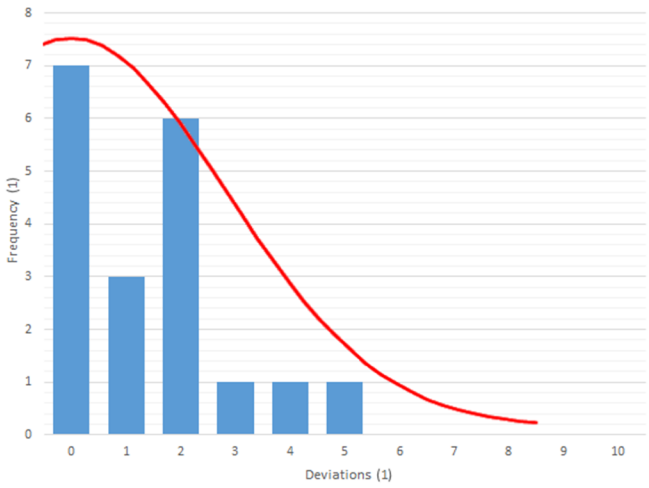

Figure 112. Distribution of the deviation numbers (in blue), velocity control mode, task 3, Differential gear-based design joint; normal distribution curve (in red).

However, there are also samples, which graphs cannot be clearly identified. An example is presented in Figure 113.

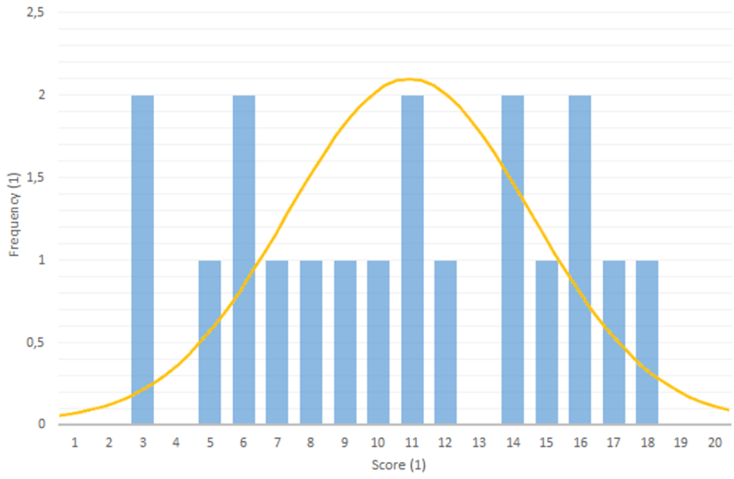

Figure 113. Score distribution (in blue), position control mode, task 1, Differential gear-based design joint; normal distribution curve (in yellow).

In order to identify the distribution type of every sample, Shapiro-Wilk normality test was used. The results of the test are presented in Tables 7 and 8.

Table 7. Active 2R spherical mechanism-based joint sample distributions

	Velocity control mode				Position control mode			
Task	1	2	3	4	1	2	3	4
Distribution type	Normal	Normal	Not normal	Normal	Normal	Not normal	Not normal	Not normal

Table 8. Differential gear-based design joint sample distributions

	Velocity control mode				Position control mode			
Task	1	2	3	4	1	2	3	4
Distribution type	Normal	Not normal	Not normal	Normal	Normal	Normal	Normal	Not normal

These results correlate with the graphs, whose distribution was obvious and provide definite distribution types for the other samples. Now it is possible to choose the statistical analysis tools for experimental data processing. The tests that were used to evaluate the force feedback system are presented in Table 9. The tests for joint modes comparison are presented in Table 10. The tests for joint assessment are presented in Table 11.

Table 9. Statistic tests for the force feedback system evaluation.

Joint	Active 2R spherical mechanism-based joint				Differential gear-based design			
Mode	Velocity control		Position control		Velocity control		Position control	
Task	1	2	1	2	1	2	1	2
Test	Paired T-test		Wilcoxon's signed rank test		Wilcoxon's signed rank test		Paired T-test	

Table 10. Tests for control modes assessment.

Joint	Active 2R spherical mechanism-based joint			Differential gear-based design		
Task	2	3	4	2	3	4
Test	Wilcoxon's signed rank test			Wilcoxon's signed rank test		

Table 11. Tests to compare the performance of the joints.

Mode	Velocity control			Position control		
Task	2	3	4	2	3	4
Test	Mann-Whitney U-test		Unpaired T-test	Mann-Whitney U-test		

5.3.2.3. Statistical test results

The results of the statistical tests are presented in Tables 12-14.

Table 12. Results of the force feedback system comparison tests.

Joint	Active 2R spherical mechanism-based joint				Differential gear-based design			
Mode	Velocity control		Position control		Velocity control		Position control	
Task	1	2	1	2	1	2	1	2
Result	No significant difference		No significant difference		No significant difference		No significant difference	

Table 13. Results of the control modes comparison tests.

Joint	Active 2R spherical mechanism-based joint			Differential gear-based design		
Task	2	3	4	2	3	4
Result	Significant difference	Significant difference	Significant difference	Significant difference	Significant difference	Significant difference

Table 14. Results of the joint performance comparison tests.

Mode	Velocity control		Position control	
Task	3	4	3	4
Result	No significant difference	No significant difference	Significant difference	Significant difference

5.3.3. Discussion on haptic device test results

5.3.3.1. Force feedback system evaluation

From Table 12 it can be seen that there is no significant difference between task 1 and 2 in both velocity and position control mode for both joints. This fact indicates that the joints have common problems, related to force feedback system. There are several possible reasons that could cause such result.

One of the main reasons is that some testers did not understand correctly how they should grade the task. It can be seen from a written feedback that some testers claim that force feedback helps, and execution of the task 2 is easier than the task 1, but it contradicts to the grades that they have left. For instance, Tester 13 (Active 2R spherical mechanism-based joint) after accomplishing task 1 wrote: “It is complex to predict the end of the border”. His/her score in this task was 15. After the second task, the comment was the following: “I feel more comfortable in the second task because I know better how does it work and the force feedback helps too”. Nonetheless, his/her score for this task was 17, which is worse. It could happen because of the logical error. In NASA TLX form, the score increases from left to right and is duplicated buy the notes low, medium and high. However, the Performance scale starts with success and ends with a complete failure, which can confuse people, who identify big score with a good result. However, in this case, the bigger the score is, the worse is the quality of the system. Thus, people could put the mark in the wrong side of the scale. Though it is possible to omit the data, which are produced by people who clearly had a misunderstanding, we cannot be completely sure that other people understood the grading correctly, because they have not left any additional

feedback, or they have not written anything, regarding this issue. Thus, it was decided to leave the data complete.

The second reason is the high value of the force feedback. The level of the physical demand and effort can indicate that it is hard to perform the task 2, when the force feedback is on. An example, presenting the score comparison for the tasks 1 and 2 of active 2R spherical mechanism-based joint is presented in Figure 114.

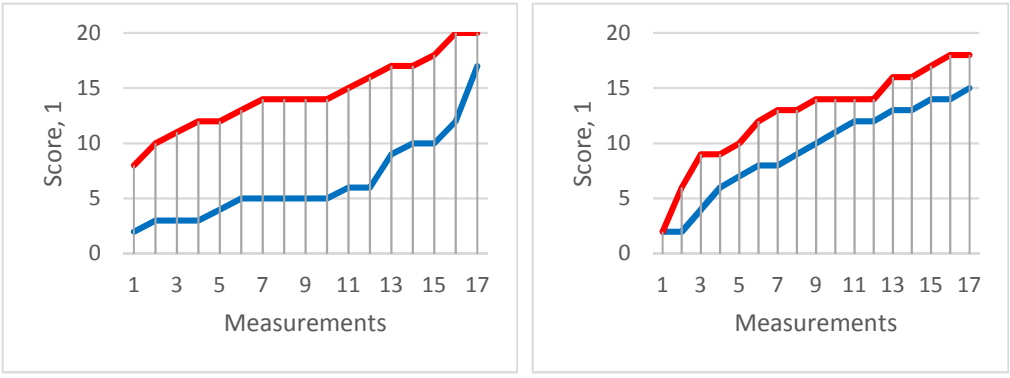

a) b)

Figure 114. Active 2R spherical mechanism-based joint testing scores: a) physical demand; b) effort. Task 1 in blue, task 2 in red. The data is arranged in ascending order.

In this Figure, the data are arranged in ascending order, so it can be clearly seen that the scores of the task 2 are higher than the task 1. In appendix A, it can be seen that the score means of all parameters, which can be related to physical efforts (and even the frustration field) are significantly higher for task 2 in both control modes. Nevertheless, it should be noted that these data were not processed by statistical analysis and are used only for illustrative purpose.

The value of the feedback was made high in order to make it distinctive from the

friction forces, which act in the mechanism of the joint. However, for the majority of the testers the value of the force feedback was uncomfortable and affected the execution of the tasks. This also can be seen from the feedbacks, written by several testers. For instance: “The force is very high to control it”, “The force is too strong” (Tester 6); “When you are reaching the limits, the feedback is a bit rough.” (Tester 14).

Active 2R spherical mechanism-based joint has one more possible cause why the force feedback system performance is not satisfactory. This joint has complex kinematics. The necessity in switching the actuators when passing zero affects the precision and the general performance of the mechanism. The clearances that cannot be compensated in the passive joint mode and the force oscillations, caused by the actuator switching make mechanism control very complex.

Considering the obtained data, it can be said that that the force feedback system works successfully and helps indicating the workspace borders. Its performance can be improved by manufacturing the prototypes with conventional technologies to decrease the internal friction forces that condition the high values of the force generated by the system. In addition, in further studies, more attention should be paid to initial instructions given to the testers in order to avoid confusions and misunderstandings.

5.3.3.2. Control modes comparison and evaluation

As it can be seen from Table 13, there is a significant difference between the velocity and the position control modes in all the tasks for both joints. It means that now we can operate with the mean values directly in order to define the best control mode. The score means are presented in Table 15.

Table 15. Score means (control mode evaluation).

Joint	Active 2R spherical mechanism-based joint			Differential gear-based design		
Task / Control mode	2	3	4	2	3	4
Velocity (means)	9.53	1.82	5.53	6.16	1.42	4.32
Position (means)	13.65	20	20	11.37	10.16	14.84

It can be seen, that the velocity control mode provides better results in all the tasks. The main reason is that in velocity mode, the mechanism is less sensitive to the handle position and it is easier to achieve precise motion of the mechanism's end-effector. In the position control mode, on the contrary, the mechanism becomes sensitive to any small handle motion. The person, who operates the mechanism, sometimes cannot sense the change in the handle position that causes the end-effector motion. In addition, the clearances of the joint, caused by the manufacturing method, make the control in the position mode harder. In the haptic device application, the clearances cannot be compensated, as the joint is used in a passive way. The active 2R spherical mechanism-based joint is more influenced by the clearances, because it has more parts that have sliding contacts and its kinematics is more complex. The differential gear-based design joint prototype is less affected by it, because the only clearance that affects the haptic device precision is in the gear, that controls angle λ. However, angle ψ is free from clearances due to the features of the setup design.

After the tests, the operators were asked to share their experience and tell which control mode they prefer. The results of this survey are presented in Table 16.

Table 16. The best control mode by testers' opinion.

Active 2R spherical mechanism-based joint		Differential gear-based design	
Tester №	The best control mode	Tester №	The best control mode
1	-	1	Velocity mode
2	Velocity mode	2	Velocity mode
3	Velocity mode	3	Velocity mode
4	Velocity mode	4	Velocity mode
5	Velocity mode	5	Velocity mode
6	Velocity mode	6	Velocity mode
7	Position mode	7	Velocity mode
8	Velocity mode	8	Velocity mode
9	Velocity mode	9	Velocity mode
10	Velocity mode	10	Velocity mode
11	Velocity mode	11	Velocity mode
12	Velocity mode	12	Velocity mode
13	Position mode	13	Position mode
14	Position mode	14	Velocity mode
15	Velocity mode	15	Velocity mode
16	Velocity mode	16	Velocity mode
17	Velocity mode	17	Velocity mode
		18	Velocity mode
		19	Velocity mode

These results confirm the ones obtained with the statistical analysis. In addition, it can be seen in Appendix C, that most of the comments related to the control mode state that the position mode is much harder. Only few people state that it is better because it is "more intuitive".

Basing on the statistical analysis results and feedback from the testers it can be

said with confidence that velocity control mode is the most suitable for current haptic device as, on the one hand, it has been demonstrated that its performance is better, and, on the other hand, most of the testers conclude that is use is much easier.

5.3.3.3. Joint designs evaluation

As in the control mode comparison, we can now operate directly with the sample means. The means are presented in Table 17.

Table 17. Score means in position control mode (joint performance evaluation).

Joint	Task 3	Task 4
Active 2R spherical mechanism-based joint (mean)	20	20
Differential gear-based design (mean)	10.16	14.84

In Table 17, it can be seen that the tasks 3 and 4 of the position control mode have a very big difference in means. The differential gear-based design provides much better performance in this control mode. As it was mentioned before, active 2R spherical mechanism-based joint has more complex kinematics, which requires more complex control system. As it was described in Section 4.1.2.2, the controlling software needs to switch between the β-encoders, depending on the value of angle α. The problem is that the value of λ, calculated based on β is always different than λ, calculated based on β'. It was caused by the clearances between the cranks and other joint components. The difference during the experiments reached $3° - 5°$. Taking into account that in the position control mode, the handle of the joint is very sensitive to any small motion, this "virtual" motion caused big leaps of the end-effector of the 2-RFR mechanism. Another

problem related to the kinematics of this joint was a tendency to jam in certain positions. When angle α was around $\pm 25° - \pm 35°$ and angle β or β' reached $\pm 90°$, the friction between the connection links and the central sphere of the joint becomes too high and makes impossible for the red actuator to create the proper force feedback. It also creates a problem for the tester to move the handle in the vertical direction. It is especially important for the task 4 of the position control mode, where the speed of reaction is required. The kinematics of the differential gear-based design is significantly simpler and it provides better control on the 2-RFR mechanism in the position control mode.

Aside of the statistical analysis, the testers that participated in the both experiments were asked to choose the best joint. The differential gear-based design was chosen in 100% of cases. This fact supports the results of the statistical analysis.

Considering all presented information, it can be said that in the velocity control mode, both joints present similar performance, but in the position control mode the differential gear-based design demonstrates significantly improved results. This makes this joint's application more versatile and characterizes it like more reliable.

5.4. Summary

The functionality testing demonstrated that both joint concepts are functional and can be used in practical applications with minor design modifications. The possibility of clearance compensation was confirmed for both joint designs.

The reconfiguration ability of the joints was tested successfully. Both joint

prototypes could provide steady and precise motion of the end-effector along the horizontal axis. This feature was tested both with and without the force feedback.

Two groups of participants have tested the haptic device designs in two control modes. The tasks 1 and 2 have revealed that the force feedback system was successful and functional. However, it is possible to improve its qualities by manufacturing joint prototypes with conventional machining from proper materials. This will decrease internal friction together with the necessity of intensive force feedback. However, in further work it is necessary to improve induction training part of the test in order to avoid grading mistakes.

The statistical analysis along with the participants' feedback have revealed that the velocity control mode is easier to use in both joints. It is less sensitive to accidental motion and provides more precise and efficient control of the end-effector.

The comparison of the two joints has identified that the differential gear-based design provides better performance in the haptic device application. It was found that it ensures better mechanism control precision in the position control mode due to the simple kinematics. The tester feedbacks confirm the statistical analysis data. In 100% of cases, the participants who have tested both joint designs have chosen the differential gear-based design as the best tested joint.

Considering the experimental results and their analysis, it can be said that experimental part of this Thesis was completed successfully. All the goals, which were presented in the Section 5.1, were reached.

6. Summary and future research

6.1. Conclusions

In this dissertation the development and testing of two reconfigurable 2 DOF spherical-like joints has been accomplished. The proposed joints provide significant advantages over conventional spherical or universal joints by being applicable in various reconfiguration methods.

Chapter 1 has provided an in-depth study of the reconfiguration methods used in parallel robots. The use of reconfigurable joints has proven to be a smart solution to increase the capacity of the conventional parallel manipulators. In order to identify the most commonly used joint types, the commercially available parallel manipulators and haptic devices were considered. It was found that most of the considered mechanisms utilize spherical, universal, prismatic and revolute joints. Therefore, implementing a spherical or a universal joint as reconfigurable joints could provide the biggest profit, as they are used in the majority of manipulators and haptic devices. The patents and research related to the active spherical joints and mechanisms were studied. It was found that none of the existing solutions satisfies the desired criteria, these being: durable, low inertia forces, accuracy, simple to manufacture and assembly, high load capacity, small dimensions and big workspace. Hence, the necessity in a better design of a reconfigurable joint was indicated.

In Chapter 2, nine original designs of spherical reconfigurable joints and mechanisms were proposed. The advantages and disadvantages of the proposed joint designs were considered in detail. In addition, the conventional universal

joint was analyzed in order to compare it with the proposed designs. The comparison was made according to eight criteria: functionality, workspace size, workspace homogeneity, accuracy, manufacturing and assembly complexity, load capacity, dimensions, and inertia. The results indicated several prominent joint designs, from which two joints were selected for further study: active 2R spherical mechanism-based joint 2nd concept and differential gear-based design 3rd concept. These joint designs have shown to provide significant advantages in terms of their characteristics and applicability in different reconfiguration strategies, described in Chapter 1. Both joint designs are able to provide reconfigurability by relocation of one of the axes of the revolute joints that compose the proposed joints and locking it in the desired position.

In Chapter 3, the proposed two designs were subjected to thorough analysis in order to identify their strong and week points. The position analysis, the velocity equations, the workspace characterization, quasi-static and finite element analysis were presented.

The study of active 2R spherical mechanism-based joint indicated that it has quite simple equations of the direct and inverse position problems. The analysis of the Jacobian matrices derived from the velocity problem, established singularity positions in the workspace limits for the inverse Jacobian and two singularity types within the workspace limits for the direct Jacobian. However, the inverse singularities and one type of the direct singularity appear outside of the practical workspace of the joint. The remaining singularity type generates singular positions that cannot be reached at the same time by both blue cranks. Consequently, the joint remains controllable in every position within the practical workspace. In addition, within the practical workspace there exist some

special points where Kinematic Conditioning Index equals 1. The Global Conditioning index of the joint's practical workspace equals 0.35, thus, showing an adequate performance in this operational workspace. Regarding the quasi-static analysis, the results indicate that the joint experiences high load, when one of the blue cranks stays in a singular position and the remaining crank carries the entire load. This position was used in the finite element analysis to determine the mechanical properties of the joint parts. It was found that the most loaded part of the joint is the connection link. The stress values in the link can exceed the maximum load of the material that was selected for the prototype; however, as it was explained in Chapter 5, the real stress values in the prototype are smaller than the calculated ones. The structural properties of the joint can be improved by replacing current material (ABS and Onyx) by aluminum or steel.

In relation to the differential gear-based joint, it has been shown that it presents very simple and straightforward kinematics, which facilitates the control system to activate the joint. Its position and velocity equations are easy to solve, the analysis of the Jacobians did not indicate any singular positions. The Kinematic Conditioning Index and Global Conditioning index equal one in the whole workspace of the joint, thus having the optimum performance. The quasi-static analysis did not reveal any components that could cause additional friction in the mechanism of the joint. The force transmission in the joint is also very simple and mainly depends on the gear ratio of the bevel gears used in the joint. It was indicated that in the gears of the joint, the teeth are subjected to significant load, which is applied to a very small area. Hence, it can be stated with high probability that the gear teeth are the most loaded parts of the joint. The finite element analysis presented stress levels that are much smaller than the maximum for the S45C steel, which is the material of the gears.

From the control point of view, it has been proved that the differential gear-based design joint has advantages over the active 2R spherical mechanism-based joint, as it is simpler and it does not present any kind of singularity. Nevertheless, to prove the functioning in real practice it was necessary to manufacture and test the prototypes of both joints in order to define the best design.

In Chapter 4, the experimental setup design has been presented. Most of the parts were made using 3D printing with fused deposition modelling technology. The remaining parts were built by using conventional manufacturing methods. Specific software was developed in Python programming language to control the prototype.

In Chapter 5, the process of testing the joint prototypes has been described. The prototypes were subjected to two testing types: the functionality testing and the haptic device application testing. Special experimental setups were built for each type of testing, due to the difference in test conditions and joint designs.

The functionality testing served to prove the concepts of the joints. The first part of the test consisted of execution of a simple trajectory that contained six points. The trajectory was run several times in order to define the deviation from the specified parameters. In the second part of the test, the clearance compensation ability of the joints was tested. Both joints have presented satisfactory results in executing the trajectory, thus proving their controllability. The ability of clearance compensation was also confirmed for both joints.

The haptic device application testing was intended to investigate the joints' qualities as a haptic device. Each joint was used as a joystick with a force feedback system that controlled a 2-RFR planar ultraflexible mechanism. The

test included two control modes: velocity and position. Depending on the mode, the operator could control the velocity or the position of the end-effector of the manipulator. The operator had to execute four tasks in each of the control modes. The tasks included finding the workspace borders without the force feedback, finding the workspace borders with the force feedback, following the proposed trajectory, and following the leading object. A group of operators executed these tasks. After the tests, the operators were asked to fill NASA TLX form in order to assess the task execution. The participants also had a possibility to leave a written feedback to provide some more information about their experience. At first, the data was compared with the normal distribution using graphical approach and Shapiro-Wilk numerical test. According to the result, parametric or non-parametric statistical tools were used for the data analysis. To compare data with normal distribution paired and unpaired T-test was used; for the data that does not satisfy the normal distribution, or the mixed data, Wilcoxon's signed rank test and The Mann-Whitney U-test were used.

The results of the tests were divided into subjective (tasks 1 and 2) and objective parts (tasks 3 and 4). The subjective results are based on the testers' personal opinion, meanwhile the objective part results are based on numerical values, obtained by calculating the deviations in tasks 3 and 4. In order to calculate the deviations, the experimental process was filmed.

The data of the subjective part did not indicate statistically significant difference between the tasks with the force feedback system on or off in both control modes. It can be concluded that this is mainly related to some mistakes in the operators' assessment (some of the testers confused the low grade with the high) and prototype imperfections (internal friction). The analysis of the control mode

demonstrates that the velocity control mode provides better precision then the position mode. Some of the testers, however, refer to the position control mode as “more intuitive”. It can be concluded that the poor results of the position mode can be caused by the sensitivity problem (relation between the inclination of the handle and the displacement of the end-effector).

Regarding the joints’ performance, the data of the tasks 3 and 4 in position mode presented statistically significant difference in their values. The differential gear-based design joint produced better results due to the simplicity of control and less influence of the joint prototype imperfections. All the testers that participated in testing of both joints have clearly stated that they prefer the differential gear-based design joint.

Aside the four tasks related to the performance as a haptic device, the reconfigurability of the joints was also tested. By locking one DOF with the special clamp, the joints can provide precise motion of the 2-RFR mechanism in the horizontal direction. This functionality was tested in both control modes with the force feedback system turned on. The clamp implemented reliable fixation of the red cranks of the joints in all cases. No deviations from a straight motion were detected during the test. Thus, the reconfiguration ability was proven in the proposed application.

In summary, the following main targets have been achieved with this Thesis. Two designs of the reconfigurable active spherical-like 2-DOF joints were proposed and thoroughly investigated. The proposed joints have simple kinematics, small dimensions, high load capacity, simple design, low inertia, and wide workspace. The prototype testing has proved the concept of both joints, including the reconfigurability, in the haptic device application. The results

indicate superior performance of the differential gear-based design joint.

6.2. Main contributions of the Thesis

The main contributions of this Thesis are:

- Two novel reconfigurable 2R joints that can be used in parallel manipulators and haptic devices were developed
- The extensive theoretical characterization of the proposed joints was provided.
- Based on the novel joints, two reconfigurable haptic device designs were developed.
- The reconfigurability of these haptic device designs, consisting in the ability of a precise straight horizontal motion of the controlled mechanism's end-effector, was confirmed experimentally.

6.2. Future research

In order to improve the results of the experimental testing, the next measures could be implemented in the future work:

- Manufacture the joint prototypes from metal in order to reduce clearance and improve the durability.
- Redesign the force feedback system using DC motors to raise the frequency of the system and the time of response.
- Redesign the control system accordingly to the new hardware design.
- Raise the number of operators in the test to 30-40 without using the same people in testing of both joints in order to avoid bias results.

- Pay special attention to clarification of the assessment of test by the operators in order to avoid assessment mistakes.
- Introduce automatic mechanical locking system to implement the reconfigurability.
- Choose the architecture of the commercially available parallel manipulator to transform it into a reconfigurable one using the proposed joints. Carry out modelling of a novel reconfigurable manipulator and compare its characteristics with the base model.
- Manufacture a prototype of a reconfigurable parallel manipulator with the proposed joints to test its real qualities.
- Study the performance of the proposed haptic devices during human-robot cooperation.

7. Main Outcomes of this Thesis

Articles Indexed in Journal Citation Reports

M. Riabtsev, V. Petuya, M. Urízar, and E. Macho. “Design and analysis of an active 2-DOF lockable joint,” *Mech. Based Des. Struct. Mach.*, pp. 1–25, Jun. 2020. https://doi.org/10.1080/15397734.2020.1784203. Impact factor: 2.679 (year 2020). Category: Q2: 38/91 Engineering. Multidisciplinary.

M. Ceccarelli, M. Riabtsev, A. Fort, M. Russo, M.A. Laribi, M. Urizar. Design and Experimental Characterization of L-CADEL v2, an Assistive Device for Elbow Motion. *Sensors*. 21(15):5149. https://doi.org/10.3390/s21155149, 2021. Impact factor: 3.576 (year 2020). Category: Q1: 14/64 Instruments & Instrumentation; Q2: 82/273 Engineering, Electrical & Electronic

M. Riabtsev, V. Petuya, M. Urízar, O. Altuzarra. Design and Testing of Two Haptic Devices Based on Reconfigurable 2R Joints. Applied Sciences, 2022, Vol. 12 (1), 339 (18 pags.). https://doi.org/10.3390/app12010339. Impact factor: 2.679 (year 2020). Category: Q2: 38/91 Engineering. Multidisciplinary.

Conference Publications

M. Riabtsev, V. Petuya, A. Riera, and E. Macho, “Design of an active reconfigurable 2R joint,” 15th IFToMM World Congress on Mechanism and Machine Science, vol. 73, pp. 1423–1429, 2019. DOI: 10.1007/978-3-030-20131-9_140. ISBN: 978-3-030-20131-9

M. Riabtsev, V. Petuya, and A. Riera, “An Active / Passive Joint for

Reconfiguration Applications," in Proceedings of the Fifth MeTrApp Conference 2019, 2020, pp. 133–140. DOI: 10.1007/978-981-15-0142-5. ISBN: 978-981-15-0142-5

Patents

Marco Ceccarelli, Matteo Russo, Monica Urizar Arana, Mykhailo Riabtsev, Axel Fort, Mohamed Amine Laribi, Dispositivo portatile per assistenza motoria del gomito (Portable device for motion assistance of the elbow), nº 102021000013229, Italy, 20/5/2021

8. Bibliography

[1] C.-H. Kuo, J. S. Dai, and H.-S. Yan, “Reconfiguration principles and strategies for reconfigurable mechanisms,” *2009 ASME/IFToMM Int. Conf. Reconfigurable Mech. Robot.*, pp. 1–7, 2009.

[2] I. Chen, “Structure Synthesis and Singularity Analysis of a Parallel Manipulator Based on Selective Actuation,” *Structure*, no. April, pp. 4533–4538, 2004.

[3] Y. Jin, I. Chen, and G. Yang, “Structure Synthesis of 6-DOF 3-3 Decoupled Parallel Manipulators,” *12th IFToMM World Congr.*, 2007.

[4] I. M. Chen, “Rapid response manufacturing through a rapidly reconfigurable robotic workcell,” *Robot. Comput. Integr. Manuf.*, vol. 17, no. 3, pp. 199–213, 2001.

[5] Z. M. Bi and L. Wang, “Optimal design of reconfigurable parallel machining systems,” *Robot. Comput. Integr. Manuf.*, vol. 25, no. 6, pp. 951–961, 2009.

[6] P. Barattini *et al.*, “Towards tailor made robot co workers based on a plug&produce framework,” *Proc. - 2013 IEEE Int. Symp. Assem. Manuf. ISAM 2013*, pp. 1–7, 2013.

[7] W. Wang, H. Zhang, G. Zong, and Z. Deng, “A Reconfigurable Mobile Robots System Based on Parallel Mechanism,” *Parallel Manip. Towar.*

New Appl., no. April, 2008.

[8] F. Aimedee, G. Gogu, J. S. Dai, C. Bouzgarrou, and N. Bouton, “Systematization of morphing in reconfigurable mechanisms,” *Mech. Mach. Theory*, vol. 96, pp. 215–224, 2016.

[9] S. Li, H. Wang, Q. Meng, and J. S. Dai, “Task-based structure synthesis of source metamorphic mechanisms and constrained forms of metamorphic joints,” *Mech. Mach. Theory*, vol. 96, pp. 334–345, 2016.

[10] J. Yu, J. S. Dai, T. Zhao, S. Bi, and G. Zong, “Mobility analysis of complex joints by means of screw theory,” *Robotica*, vol. 27, no. 6, pp. 915–927, 2009.

[11] W. E. E. K. Lim and S. H. Yeo, “Kinematic Design of Modular Recon gurable In-Parallel Robots,” *Auton. Robots*, pp. 83–89, 2001.

[12] K. Wohlhart, “Kinematotropic Linkages,” *Recent Adv. Robot Kinemat.*, pp. 359–368, 1996.

[13] A. Mueller, “Redundant Actuation of Parallel Manipulators,” *Parallel Manip. Towar. New Appl.*, no. April, 2008.

[14] F. Xi, Y. Xu, and G. Xiong, “Design and analysis of a re-configurable parallel robot,” *Mech. Mach. Theory*, vol. 41, no. 2, pp. 191–211, 2006.

[15] T. Mannheim, M. Riedel, M. Hüsing, and B. Corves, “A New Way of Grasping:PARAGRIP—The Fusion of Gripperand Robot,” in *Handbook of Robotic Grasp*, vol. 10, G. Carbone, Ed. Springer, London, 2012, pp. 433–464.

[16] A. D. Finistauri, F. Xi, and B. Petz, “Architecture Design and Optimization of an On-the-Fly Reconfigurable Parallel Robot,” in *Parallel Manipulators, Towards New Applications*, H. Wu, Ed. Vienna: I-Tech Education and Publishing, 2008, p. 506.

[17] L. Nurahmi, S. Caro, P. Wenger, J. Schadlbauer, and M. Husty, “Reconfiguration analysis of a 4-RUU parallel manipulator,” *Mech. Mach. Theory*, vol. 96, pp. 269–289, 2016.

[18] J.-P. Merlet, “Determination of the optimal geometry of modular parallel robots,” vol. 1, pp. 1197–1202 vol.1, 2003.

[19] C. T. Chen, “Reconfiguration of a parallel kinematic manipulator for the maximum dynamic load-carrying capacity,” *Mech. Mach. Theory*, vol. 54, pp. 62–75, 2012.

[20] J. Borras, F. Thomas, E. Ottaviano, and M. Ceccarelli, “A reconfigurable 5-DoF 5-SPU parallel platform,” no. JULY, pp. 617–623, 2009.

[21] G. Coppola, D. Zhang, and K. Liu, “A 6-DOF reconfigurable hybrid parallel manipulator,” *Robot. Comput. Integr. Manuf.*, vol. 30, no. 2, pp. 99–106, 2014.

[22] G. Huang, S. Guo, D. Zhang, H. Qu, and H. Tang, “Kinematic analysis and multi-objective optimization of a new reconfigurable parallel mechanism with high stiffness,” *Robotica*, vol. 36, no. 2, pp. 187–203, 2018.

[23] Z. M. Bi and B. Kang, “Enhancement of Adaptability of Parallel

Kinematic Machines With an Adjustable Platform," *J. Manuf. Sci. Eng.*, vol. 132, no. 6, p. 061016, 2010.

[24] C. Viegas, M. Tavakoli, and A. T. d. Almeida, "A novel grid-based reconfigurable spatial parallel mechanism with large workspace," *Mech. Mach. Theory*, vol. 115, pp. 149–167, 2017.

[25] C. Viegas, M. Tavakoli, and A. T. d. Almeida, "A novel grid-based reconfigurable spatial parallel mechanism with large workspace," *Mech. Mach. Theory*, vol. 115, pp. 149–167, 2017.

[26] G. Wu, H. Dong, D. Wang, and S. Bai, "A 3 – RRR Spherical Parallel Manipulator Reconfigured with Four-bar Linkages," in *4th IEEE/IFToMM International Conference on Reconfigurable Mechanisms and Robots (ReMAR 2018)*, 2018, no. June, pp. 20–22.

[27] M. Callegari, L. Carbonari, G. Palmieri, and M. C. Palpacelli, "Parallel wrists for enhancing grasping performance," *Mech. Mach. Sci.*, vol. 10, pp. 189–219, 2012.

[28] J. A. Carretero, R. P. Podhorodeski, M. A. Nahon, and C. M. Gosselin, "Kinematic Analysis and Optimization of a New Three Degree-of-Freedom Spatial Parallel Manipulator," *J. Mech. Des.*, vol. 122, no. 1, pp. 17–24, Dec. 2000.

[29] S. Nansai, N. Rojas, M. R. Elara, and R. Sosa, "Exploration of adaptive gait patterns with a reconfigurable linkage mechanism," *IEEE Int. Conf. Intell. Robot. Syst.*, pp. 4661–4668, 2013.

[30] T. Hoeltgebaum, R. Simoni, and D. Martins, “Reconfigurability of engines: A kinematic approach to variable compression ratio engines,” *Mech. Mach. Theory*, vol. 96, no. 199, pp. 308–322, 2016.

[31] S. Sarabandi, P. Grosch, J. M. Porta, and F. Thomas, “A Reconfigurable Asymmetric 3-UPU Parallel Robot,” *2018 Int. Conf. Reconfigurable Mech. Robot. ReMAR 2018 - Proc.*, no. June, pp. 20–22, 2018.

[32] P. Grosch, R. Di Gregorio, J. Lopez, and F. Thomas, “Motion Planning for a Novel Reconfigurable Parallel Manipulatorwith Lockable Revolute Joints,” *IEEE Int. Conf. Robot. Autom.*, pp. 4697–4702, 2010.

[33] X. Kong, C. M. Gosselin, and P.-L. Richard, “Type Synthesis of Parallel Mechanisms With Multiple Operation Modes,” *J. Mech. Des.*, vol. 129, no. 6, p. 595, 2007.

[34] Y. Jin, I. M. Chen, and G. Yang, “Kinematic design of a family of 6-DOF partially decoupled parallel manipulators,” *Mech. Mach. Theory*, vol. 44, no. 5, pp. 912–922, 2009.

[35] J. I. Ibarreche, A. Hernández, V. Petuya, M. Urízar, and E. Macho, “Multioperation capacity of parallel manipulators basing on generic kinematic chain approach,” *Mech. Mach. Theory*, vol. 116, pp. 234–247, 2017.

[36] M. C. Palpacelli, L. Carbonari, G. Palmieri, and M. Callegari, “Analysis and Design of a Reconfigurable 3-DoF Parallel Manipulator for Multimodal Tasks,” *IEEE/ASME Trans. Mechatronics*, vol. 20, no. 4, pp. 1975–1985, 2015.

[37] L. Carbonari, D. Corinaldi, G. Palmieri, and M. C. Palpacelli, “Kinematics of a Novel 3-URU Reconfigurable Parallel Robot,” *2018 Int. Conf. Reconfigurable Mech. Robot. ReMAR 2018 - Proc.*, no. June, pp. 20–22, 2018.

[38] X. Kong and Y. Jin, “Type Synthesis of 3-DOF multi-mode translational/spherical parallel mechanisms with lockable joints,” *Mech. Mach. Theory*, vol. 96, pp. 323–333, 2016.

[39] W. I. Ye, Y. Fang, and S. Guo, “Reconfigurable parallel mechanisms with three types of kinematotropic chains,” *2015 IFToMM World Congr. Proceedings, IFToMM 2015*, 2015.

[40] A. Moosavian and F. Xi, “Holonomic under-actuation of parallel robots with topological reconfiguration,” *Mech. Mach. Theory*, vol. 96, pp. 290–307, 2016.

[41] L. Carbonari, M. Callegari, G. Palmieri, and M. C. Palpacelli, “A new class of reconfigurable parallel kinematic machines,” *Mech. Mach. Theory*, vol. 79, pp. 173–183, 2014.

[42] J. Wei and J. S. Dai, “Group Method for Synthesis of Metamorphic Parallel Mechanism with 1R2T and 2R1T Reconfiguration,” *2018 Int. Conf. Reconfigurable Mech. Robot. ReMAR 2018 - Proc.*, no. June, pp. 20–22, 2018.

[43] R. Li, J. Zhao, D. Fan, S. Liang, S. Song, and S. Bai, “Design and Workspace Analysis of Reconfigurable 3-RPRP Spherical Parallel Mechanisms,” *2018 Int. Conf. Reconfigurable Mech. Robot. ReMAR 2018*

- *Proc.*, no. June, pp. 20–22, 2018.

[44] J. De Dios Flores-Mendez, H. Schiøler, O. Madsen, and S. Bai, “Design of a Dynamically Reconfigurable 3T1R Parallel Kinematic Manipulator,” *2018 Int. Conf. Reconfigurable Mech. Robot. ReMAR 2018 - Proc.*, no. June, pp. 20–22, 2018.

[45] J. I. Ibarreche, A. Hernández, V. Petuya, and M. Urízar, “A methodology to achieve the set of operation modes of reconfigurable parallel manipulators,” *Meccanica*, vol. 54, no. 15, pp. 2507–2520, 2019.

[46] D. Gan, J. S. Dai, and Q. Liao, “Mobility Change in Two Types of Metamorphic Parallel Mechanisms,” *J. Mech. Robot.*, vol. 1, no. 4, p. 041007, 2009.

[47] D. Gan, J. S. Dai, J. Dias, and L. Seneviratne, “Reconfigurability and unified kinematics modeling of a 3rTPS metamorphic parallel mechanism with perpendicular constraint screws,” *Robot. Comput. Integr. Manuf.*, vol. 29, no. 4, pp. 121–128, 2013.

[48] D. Gan, J. S. Dai, J. Dias, and L. Seneviratne, “Joint force decomposition and variation in unified inverse dynamics analysis of a metamorphic parallel mechanism,” *Meccanica*, vol. 51, no. 7, pp. 1583–1593, 2016.

[49] D. Gan, J. Dias, and L. Seneviratne, “Unified kinematics and optimal design of a 3rRPS metamorphic parallel mechanism with a reconfigurable revolute joint,” *Mech. Mach. Theory*, vol. 96, pp. 239–254, 2016.

[50] L. Nurahmi and D. Gan, “Operation Mode and Workspace of a 3-rRPS

Metamorphic Parallel Mechanism with a Reconfigurable Revolute Joint," in *Proceedings of the 4th IEEE/IFToMM Int. Conf. on Reconfigurable Mechanisms and Robots (ReMAR 2018)*, 2018, no. June, pp. 20–22.

[51] Z. Li, Y. Lou, Y. Zhang, B. Liao, and Z. Li, "Type synthesis, kinematic analysis, and optimal design of a novel class of Schoñflies-motion parallel manipulators," *IEEE Trans. Autom. Sci. Eng.*, vol. 10, no. 3, pp. 674–686, 2013.

[52] A. Nayak, S. Caro, and P. Wenger, "A Dual Reconfigurable 4-rRUU Parallel Manipulator," *2018 Int. Conf. Reconfigurable Mech. Robot. ReMAR 2018 - Proc.*, no. June, pp. 20–22, 2018.

[53] B. J. Slaboch and P. A. Voglewede, "Profile Synthesis of Planar Rotational–Translational Variable Joints," *J. Mech. Robot.*, vol. 6, no. 4, p. 041012, 2014.

[54] T.-Y. Tseng, W.-C. Hsu, F.-F. Lin, and C.-H. Kuo, "Design and experimental evaluation of a reconfigurable gravity-free muscle training assistive device for lower-limb paralysis patients," in *Proceedings of the ASME 2015 International Design Engineering Technical Conferences and Computers and Information in Engineering Conference*, 2015.

[55] C. H. Kuo, L. Nguyen-Vu, and L. T. Chou, "Static Balancing of a Reconfigurable Linkage with Switchable Mobility by Using a Single Counterweight," *2018 Int. Conf. Reconfigurable Mech. Robot. ReMAR 2018 - Proc.*, no. June, pp. 20–22, 2018.

[56] H.-S. Yan and C.-H. Kuo, "Topological Representations and

Characteristics of Variable Kinematic Joints," *J. Mech. Des.*, vol. 128, no. 2, p. 384, 2006.

[57] C. Tian, Q. J. Ge, and Y. Fang, "Reconfigurable Generalized Parallel Mechanisms with Coupling Sub-chains," in *Proceedings of the 4th IEEE/IFToMM Int. Conf. on Reconfigurable Mechanisms and Robots (ReMAR 2018)*, 2018, no. June.

[58] X. Kong, J. Wang, J. Yu, and D. Li, "Reconfiguration Analysis of a Variable Degrees-of-freedom Multi-mode Parallel Manipulator," in *2018 International Conference on Reconfigurable Mechanisms and Robots, ReMAR 2018 - Proceedings*, 2018, no. June.

[59] P. A. Halverson, L. L. Howell, and S. P. Magleby, "Tension-based multi-stable compliant rolling-contact elements," *Mech. Mach. Theory*, vol. 45, no. 2, pp. 147–156, 2010.

[60] T. G. Nelson, R. J. Lang, S. P. Magleby, and L. L. Howell, "Curved-folding-inspired deployable compliant rolling-contact element (D-CORE)," *Mech. Mach. Theory*, vol. 96, pp. 225–238, 2016.

[61] C. C. Lee and J. M. Hervé, "Various types of RC//RC-like linkages and the discontinuously movable Koenigs joint," *Mech. Mach. Theory*, vol. 96, pp. 255–268, 2016.

[62] K. Suleman, K. Andersson, and J. Wikander, "Dynamic based control strategy for haptic devices," *2011 IEEE World Haptics Conf. WHC 2011*, pp. 131–136, 2011.

[63] Y. H. Hwang, S. R. Kang, S. W. Cha, and S. B. Choi, “An electrorheological spherical joint actuator for a haptic master with application to robot-assisted cutting surgery,” *Sensors Actuators, A Phys.*, vol. 249, pp. 163–171, 2016.

[64] M. Riabtsev, V. Petuya, A. Riera, and E. Macho, “Design of an active reconfigurable 2R joint,” *Mech. Mach. Sci.*, vol. 73, pp. 1423–1429, 2019.

[65] T. Sansanayuth, I. Nilkhamhang, and K. Tungpimolrat, “Teleoperation with inverse dynamics control for PHANToM Omni haptic device,” *Proc. SICE Annu. Conf.*, pp. 2121–2126, 2012.

[66] E. C. Shin and J. H. Ryu, “Transmission of operator intention impedance using phantom haptic device,” *2014 11th Int. Conf. Ubiquitous Robot. Ambient Intell. URAI 2014*, no. Urai, pp. 92–94, 2014.

[67] C. Luciano, P. Banerjee, T. DeFanti, and S. Mehrotra, “Realistic cross-platform haptic applications using freely-available libraries,” *Proc. - 12th Int. Symp. Haptic Interfaces Virtual Environ. Teleoperator Syst. HAPTICS*, pp. 282–289, 2004.

[68] 3D SYSTEMS, “Touch Haptic Device,” 2020. [Online]. Available: https://www.3dsystems.com/haptics-devices/touch. [Accessed: 24-Jul-2020].

[69] 3D SYSTEMS, “Phantom Premium Haptic Devices,” 2020. [Online]. Available: https://www.3dsystems.com/haptics-devices/3d-systems-phantom-premium. [Accessed: 24-Jul-2020].

[70] V. Hayward, “Toward a seven axis haptic device,” *IEEE Int. Conf. Intell. Robot. Syst.*, vol. 3, no. January 1995, pp. 133–139, 1995.

[71] C. Salisbury, C. Schwab, F. Conti, and J. K. Salisbury, “A 6-DoF Haptic Device for Microsurgery,” 2007. [Online]. Available: https://web.stanford.edu/group/sailsbury_robotx/cgi-bin/salisbury_lab/?page_id=399. [Accessed: 23-Jul-2020].

[72] N. Nishimura, D. Leonardis, M. Solazzi, A. Frisoli, and H. Kajimoto, “Wearable encounter-type haptic device with 2-DoF motion and vibration for presentation of friction,” *IEEE Haptics Symp. HAPTICS*, pp. 303–306, 2014.

[73] CyberGlove Systems, “CyberTouch,” 2017. [Online]. Available: http://www.cyberglovesystems.com/cybertouch. [Accessed: 27-Jul-2020].

[74] CyberGlove Systems, “CyberTouch II,” 2017. [Online]. Available: http://www.cyberglovesystems.com/cybertouch2/. [Accessed: 27-Jul-2020].

[75] F. Hao and J. P. Merlet, “Multi-criteria optimal design of parallel manipulators based on interval analysis,” *Mech. Mach. Theory*, vol. 40, no. 2, pp. 157–171, 2005.

[76] D. Chablat and P. Wenger, “A six degree-of-freedom haptic device based on the orthoglide and a hybrid agile eye,” *Proc. ASME Des. Eng. Tech. Conf.*, vol. 2006, 2006.

[77] HapticHouse, “White Falcon 3D Touch Haptic Controller,” 2020. [Online]. Available: https://hapticshouse.com/collections/frontpage/products/white-falcon-3d-touch-haptic-controller. [Accessed: 27-Jul-2020].

[78] F. Khadivar, S. Sadeghnejad, H. Moradi, G. Vossoughi, and F. Farahmand, “Dynamic Characterization of a Parallel Haptic Device for Application as an Actuator in a Surgery Simulator,” *5th RSI Int. Conf. Robot. Mechatronics, IcRoM 2017*, no. IcRoM, pp. 186–191, 2018.

[79] P. Bachman and A. Milecki, “MR haptic joystick in control of virtual servo drive,” *J. Phys. Conf. Ser.*, vol. 149, p. 012034, 2009.

[80] S. Kim, M. Ishii, Y. Koike, and M. Sato, “Haptic interface with 7 DOF using 8 strings: SPIDAR-G,” *10th Int. Conf. Artif. Real. Tele-existence*, pp. 224–230, 2000.

[81] G. C. Burdea, “Haptics issues in virtual environments,” *Proc. Comput. Graph. Int. Conf. CGI*, pp. 295–302, 2000.

[82] CyberGlove Systems, “CyberGrasp,” 2017. [Online]. Available: http://www.cyberglovesystems.com/cybergrasp/. [Accessed: 27-Jul-2020].

[83] CyberGlove Systems, “CyberForce,” 2017. [Online]. Available: http://www.cyberglovesystems.com/cyberforce/. [Accessed: 27-Jul-2020].

[84] “GLOBAL PARALLEL ROBOTS MARKET 2016-2020,” 2016.

[85] ABB, “IRB 360 FlexPicker,” 2020. [Online]. Available: http://new.abb.com/products/robotics/industrial-robots/irb-360. [Accessed: 23-Mar-2020].

[86] FANUC, “M-1iA/0.5S,” 2020. [Online]. Available: http://www.fanuc.eu/uk/en/robots/robot-filter-page/m1-series/m-1ia-05s?returnurl=http%3A%2F%2Fwww.fanuc.eu%2Fuk%2Fen%2Frobots%2Frobot-filter-page. [Accessed: 23-Mar-2020].

[87] OMRON, “Quattro,” 2020. [Online]. Available: https://industrial.omron.co.uk/en/products/quattro. [Accessed: 23-Mar-2020].

[88] FANUC, “F-200iB,” 2005. [Online]. Available: https://www.fanucamerica.com/docs/default-source/robotics-product-information-sheets/f-200ib-series_9.pdf?sfvrsn=f4faf90a_4. [Accessed: 23-Mar-2020].

[89] Symetrie, “BREVA,” 2020. [Online]. Available: http://www.symetrie.fr/en/products/positioning-hexapods/breva/. [Accessed: 23-Mar-2020].

[90] Gridbots, “Hexamove,” 2020. [Online]. Available: https://www.gridbots.com/hexamove.html. [Accessed: 23-Mar-2020].

[91] Mitsubishi Electric, “Micro working robot.” [Online]. Available: http://www.mitsubishielectric.com/fa/products/rbt/robot/items/micro/index.html#pageUnit01. [Accessed: 23-Mar-2020].

[92] Gridbots, “Rapi - Mov,” 2020. [Online]. Available: https://www.gridbots.com/rapiMov.html. [Accessed: 23-Mar-2020].

[93] R. Y. Dien and E. Luce, “Spherical robotic wrist joint,” 4628765, 1986.

[94] M. Simnofske, S. Kumar, B. Bongardt, and F. Kirchner, “Active ankle - An almost-spherical parallel mechanism,” *47th Int. Symp. Robot. ISR 2016*, vol. 4150, pp. 37–42, 2016.

[95] G. Palmieri, M. Callegari, L. Carbonari, and M. C. Palpacelli, “Design and testing of a spherical parallel mini manipulator,” *MESA 2014 - 10th IEEE/ASME Int. Conf. Mechatron. Embed. Syst. Appl. Conf. Proc.*, 2014.

[96] G. Wu, S. Caro, and J. Wang, “Design and transmission analysis of an asymmetrical spherical parallel manipulator,” *Mech. Mach. Theory*, vol. 94, pp. 119–131, 2015.

[97] V. Pandey and T. V. Hariskrishna, “Novel Contact-Type Actuated Sphere for Powered Prosthetic-Ankle Joint,” *Procedia Comput. Sci.*, vol. 133, pp. 181–189, 2018.

[98] J. Gewirts and J. R. Halpern, “Spherical gear,” US9027441B2, 2015.

[99] K. C. Wu and R. Melgoza, “Spherical robotic shoulder joint,” US5533418A, 1996.

[100] Y. Yu, Y. Narita, Y. Harada, and T. Nakao, “Research of 3-DOF active rotational ball joint,” *2009 IEEE/RSJ Int. Conf. Intell. Robot. Syst. IROS 2009*, pp. 5153–5158, 2009.

[101] Z. Fan, Z. Li, and Z. Jun, “Study on H8 Control of Active Magnetic Suspension Spherical Rotating Joint,” *Proc. - 2016 3rd Int. Conf. Inf. Sci. Control Eng. ICISCE 2016*, pp. 1141–1145, 2016.

[102] K. Abe, K. Tadakuma, and R. Tadakuma, “ABENICS: Active Ball Joint Mechanism With Three-DoF Based on Spherical Gear Meshings,” *IEEE Trans. Robot.*, vol. 37, no. 5, pp. 1806–1825, 2021.

[103] G. Palmieri, M. Callegari, L. Carbonari, and M. C. Palpacelli, “Mechanical design of a mini pointing device for a robotic assembly cell,” *Meccanica*, vol. 50, no. 7, pp. 1895–1908, 2015.

[104] RS Components, “RS PRO Universal Joint, Single, Plain, Bore 20mm, 82mm Length.” [Online]. Available: https://uk.rs-online.com/web/p/universal-joints/7906716/. [Accessed: 21-Dec-2020].

[105] M. Riabtsev, V. Petuya, M. Urízar, and E. Macho, “Design and analysis of an active 2-DOF lockable joint,” *Mech. Based Des. Struct. Mach.*, pp. 1–25, Jun. 2020.

[106] C. M. Gosselin, “Dexterity indices for planar and spatial robotic manipulators,” in *Proceedings., IEEE International Conference on Robotics and Automation*, 1990, pp. 650–655 vol.1.

[107] J. Angeles and C. Lopez-Cajun, “The dexterity index of serial-type robotic manipulators,” *ASME Trends Dev. Mech. Mach. Robot.*, vol. 7984, 1988.

[108] C. Gosselin and J. Angeles, “A Global Performance Index for the

Kinematic Optimization of Robotic Manipulators," *J. Mech. Des.*, vol. 113, no. 3, pp. 220–226, Sep. 1991.

[109] O. Altuzarra, D. M. Solanillas, E. Amezua, and V. Petuya, "Path analysis for hybrid rigid–flexible mechanisms," *Mathematics*, vol. 9, no. 16, 2021.

[110] P. Schleer, S. Drobinsky, and K. Radermacher, "Evaluation of Different Modes of Haptic Guidance for Robotic Surgery," *IFAC-PapersOnLine*, vol. 51, no. 34, pp. 97–103, 2019.

[111] C. J. Luciano *et al.*, "Percutaneous Spinal Fixation Simulation With Virtual Reality and Haptics," *Neurosurgery*, vol. 72, no. suppl_1, pp. A89–A96, Jan. 2013.

[112] C. G. Corrêa, F. L. S. Nunes, E. Ranzini, R. Nakamura, and R. Tori, "Haptic interaction for needle insertion training in medical applications: The state-of-the-art," *Med. Eng. Phys.*, vol. 63, pp. 6–25, 2019.

[113] A. Chowriappa *et al.*, "Augmented-reality-based skills training for robot-assisted urethrovesical anastomosis: A multi-institutional randomised controlled trial," *BJU Int.*, vol. 115, no. 2, pp. 336–345, 2015.

[114] K. S. Choi, S. H. Chan, and W. M. Pang, "Virtual suturing simulation based on commodity physics engine for medical learning," *J. Med. Syst.*, vol. 36, no. 3, pp. 1781–1793, 2012.

[115] J. Lee *et al.*, "An intravenous injection simulator using augmented reality for veterinary education and its evaluation," *Proc. - VRCAI 2012 11th ACM SIGGRAPH Int. Conf. Virtual-Reality Contin. Its Appl. Ind.*, vol. 1,

no. 212, pp. 31–34, 2012.

[116] A. Chellali, C. Dumas, and I. Milleville-Pennel, “Influences of haptic communication on a shared manual task,” *Interact. Comput.*, vol. 23, no. 4, pp. 317–328, 2011.

[117] A. Chellali, C. Dumas, and I. Milleville-Pennel, “Haptic Communication to Support Biopsy Procedures Learning in Virtual Environments,” *Presence*, vol. 21, no. 4, pp. 470–489, 2012.

[118] A. Chellali, C. Dumas, and I. Milleville, “Haptic communication to enhance collaboration in virtual environments,” *ECCE 2010 - Eur. Conf. Cogn. Ergon. 2010 28th Annu. Conf. Eur. Assoc. Cogn. Ergon.*, no. August, pp. 83–90, 2010.

[119] W. Y. Chan, J. Qin, Y. P. Chui, and P. A. Heng, “A serious game for learning ultrasound-guided needle placement skills,” *IEEE Trans. Inf. Technol. Biomed.*, vol. 16, no. 6, pp. 1032–1042, 2012.

[120] A. M. L. S. M. Christopher, “Training surgical residents with a haptic robotic central venous catheterization,” *Physiol. Behav.*, vol. 176, no. 1, pp. 100–106, 2016.

[121] A. Lécuyer, J. M. Burkhardt, and C. H. Tan, “A study of the modification of the speed and size of the cursor for simulating pseudo-haptic bumps and holes,” *ACM Trans. Appl. Percept.*, vol. 5, no. 3, 2008.

[122] E. L. Roth Monzon, A. Chellali, C. Dumas, and C. G. L. Cao, “Training effects of a visual aid on haptic sensitivity in a needle insertion task,”

Haptics Symp. 2012, HAPTICS 2012 - Proc., no. March, pp. 199–202, 2012.

[123] L. A. McWilliams, A. Malecha, R. Langford, and P. Clutter, "Comparisons of Cooperative-Based Versus Independent Learning While Using a Haptic Intravenous Simulator," *Clin. Simul. Nurs.*, vol. 13, no. 4, pp. 154–160, 2017.

[124] S. Kang and D. Lee, "Implementation of skin manipulation in a haptic interface of needle intervention simulation," *Int. Conf. Control. Autom. Syst.*, pp. 768–772, Dec. 2014.

[125] S. Benyahia, D. Van Nguyen, A. Chellali, and S. Otmane, "Designing the user interface of a virtual needle insertion trainer," *IHM 2015 - Actes la 27eme Conf. Francoph. sur l'Interaction Homme-Machine*, no. October, 2015.

[126] D. Van Nguyen, S. Ben Lakhal, and A. Chellali, "Preliminary evaluation of a virtual needle insertion training system," *2015 IEEE Virtual Real. Conf. VR 2015 - Proc.*, no. December, pp. 247–248, 2015.

[127] J. K. Y. Ko, V. Y. T. Cheung, T. C. Pun, and W. K. Tung, "A Randomized Controlled Trial Comparing Trainee-Directed Virtual Reality Simulation Training and Box Trainer on the Acquisition of Laparoscopic Suturing Skills," *J. Obstet. Gynaecol. Canada*, vol. 40, no. 3, pp. 310–316, 2018.

[128] W. Y. Chan *et al.*, "Learning ultrasound-guided needle insertion skills through an edutainment game," *Lect. Notes Comput. Sci. (including Subser. Lect. Notes Artif. Intell. Lect. Notes Bioinformatics)*, vol. 6250

LNCS, no. December 2013, pp. 200–214, 2010.

[129] D. Ni *et al.*, “A virtual reality simulator for ultrasound-guided biopsy training,” *IEEE Comput. Graph. Appl.*, vol. 31, no. 2, pp. 36–48, 2011.

[130] A. Ghasemi and S. Zahediasl, “Normality tests for statistical analysis: A guide for non-statisticians,” *Int. J. Endocrinol. Metab.*, vol. 10, no. 2, pp. 486–489, 2012.

[131] H. C. Thode, *Testing for normality*, vol. 164. CRC press, 2002.

[132] D. Coin and R. Corradetti, “Tests for Normality : Comparison of Powers,” *Power*, no. x, pp. 177–180, 1933.

[133] “Shapiro-Wilk Test Calculator,” *Statistics Kingdom*, 2017. [Online]. Available: https://www.statskingdom.com/320ShapiroWilk.html. [Accessed: 10-May-2021].

[134] F. S. Nahm, “Nonparametric statistical tests for the continuous data: The basic concept and the practical use,” *Korean J. Anesthesiol.*, vol. 69, no. 1, pp. 8–14, 2016.

[135] G. Di Leo and F. Sardanelli, “Statistical significance : p value , 0.05 threshold , and applications to radiomics — reasons for a conservative approach,” 2020.

[136] “Paired T-Test Calculator,” *Statistics Kingdom*, 2017. [Online]. Available: https://www.statskingdom.com/160MeanT2pair.html. [Accessed: 10-May-2021].

[137] “Two Sample T-Test Calculator (Pooled-Variance),” *Statistics Kingdom*, 2017. [Online]. Available: https://www.statskingdom.com/140MeanT2eq.html. [Accessed: 10-May-2021].

[138] “Wilcoxon Signed-Rank test,” *Statistics Kingdom*, 2017. [Online]. Available: https://www.statskingdom.com/175wilcoxon_signed_ranks.html. [Accessed: 10-May-2021].

[139] “Mann Whitney U test calculator (Wilcoxon rank-sum),” *Statistics Kingdom*, 2017. [Online]. Available: https://www.statskingdom.com/170median_mann_whitney.html. [Accessed: 10-May-2021].

Appendix A

Results of the haptic device experiment

Active 2R spherical mechanism-based joint

Table 18. Velocity mode Task 1 results.

Tester №	Mental demand, 1	Physical demand, 1	Temporal demand, 1	Performance, 1	Effort, 1	Frustration, 1
1	7	3	7	16	11	4
2	6	5	7	7	7	6
3	10	12	7	7	8	7
4	5	5	14	10	4	2
5	16	9	12	17	14	4
6	8	5	7	9	9	4
7	12	17	15	13	12	17
8	16	3	5	15	15	10
9	15	4	10	3	6	1
10	1	5	4	6	2	1
11	4	6	4	10	14	10
12	15	6	9	13	13	14
13	11	3	6	15	13	15
14	10	10	6	4	12	5
15	3	2	12	18	2	2
16	12	5	1	11	8	1
17	16	10	15	2	10	5
Mean	9.82	6.47	8.29	10.35	9.41	6.35

Table 19. Velocity mode Task 2 results.

Tester №	Mental demand, 1	Physical demand, 1	Temporal demand, 1	Performance, 1	Effort, 1	Frustration, 1
1	6	14	6	11	13	11
2	7	10	10	8	9	9
3	12	14	12	11	14	12
4	5	17	10	13	16	10
5	8	16	9	15	13	9
6	8	17	12	12	9	13
7	10	12	9	6	12	9
8	13	13	6	14	14	10
9	6	12	3	2	2	4
10	4	11	5	8	10	4
11	10	20	8	14	18	12
12	13	8	8	5	14	9
13	15	14	13	17	16	12
14	14	14	13	10	14	5
15	2	20	11	11	18	11
16	10	15	1	3	6	6
17	18	18	18	2	17	10
Mean	9.47	14.41	9.06	9.53	12.65	9.18

Table 20. Velocity mode Task 3 results.

Tester №	Mental demand, 1	Physical demand, 1	Temporal demand, 1	Performance, 1	Effort, 1	Frustration, 1
1	15	10	15	7	14	13
2	9	11	10	9	10	7
3	12	15	13	11	16	11
4	15	20	15	15	19	15
5	8	15	8	14	8	13
6	12	16	11	12	16	14
7	16	18	10	10	15	9
8	14	14	8	5	15	8
9	12	15	5	8	13	3
10	6	11	11	6	9	3
11	15	20	10	8	20	11
12	14	8	8	5	13	8
13	18	16	15	14	17	16
14	17	17	18	14	17	10
15	2	18	3	4	18	9
16	10	19	3	6	19	7
17	18	17	15	4	15	15
Mean	12.53	15.29	10.47	8.94	14.94	10.12

Table 21. Velocity mode Task 4 results.

Tester №	Mental demand, 1	Physical demand, 1	Temporal demand, 1	Performance, 1	Effort, 1	Frustration, 1
1	16	7	13	10	14	7
2	9	12	10	8	9	7
3	8	13	11	3	13	7
4	17	17	14	10	16	18
5	13	15	8	8	13	9
6	13	17	10	2	18	11
7	18	18	14	12	15	17
8	15	14	14	7	15	10
9	15	17	9	10	11	10
10	6	11	9	9	8	3
11	14	20	10	6	18	6
12	14	10	12	8	13	12
13	16	14	11	11	14	10
14	19	19	17	19	17	17
15	11	19	10	6	18	6
16	18	18	9	11	17	10
17	18	18	13	6	17	14
Mean	14.12	15.24	11.41	8.59	14.47	10.24

Table 22. Position mode Task 1 results.

Tester №	Mental demand, 1	Physical demand, 1	Temporal demand, 1	Performance, 1	Effort, 1	Frustration, 1
1	13	11	14	12	15	7
2	12	7	12	15	10	10
3	8	15	10	19	16	17
4	10	10	14	10	7	12
5	8	12	8	15	13	8
6	11	9	11	18	16	17
7	14	9	10	10	11	8
8	15	7	9	14	15	13
9	16	5	9	3	10	12
10	10	6	8	10	9	6
11	15	1	11	18	17	16
12	16	16	13	19	17	17
13	11	10	16	20	16	20
14	16	10	15	18	17	18
15	11	3	10	20	11	20
16	14	6	1	8	12	7
17	10	19	19	0	10	4
Mean	12.35	9.18	11.18	13.47	13.06	12.47

Table 23. Position mode Task 2 results.

Tester №	Mental demand, 1	Physical demand, 1	Temporal demand, 1	Performance, 1	Effort, 1	Frustration, 1
1	13	17	11	1	16	20
2	10	10	12	14	12	13
3	8	14	11	12	15	14
4	4	4	9	10	6	10
5	8	17	9	18	9	9
6	11	14	12	17	14	16
7	10	14	10	16	13	18
8	15	10	6	14	15	14
9	13	19	10	16	13	14
10	8	8	9	11	8	6
11	18	18	16	20	18	19
12	17	14	17	20	16	18
13	16	16	11	18	18	20
14	18	18	18	20	18	19
15	11	19	10	19	19	19
16	11	15	1	4	14	8
17	17	17	19	2	17	12
Mean	12.24	14.35	11.24	13.65	14.18	14.65

Table 24. Position mode Task 3 results.

Tester №	Mental demand, 1	Physical demand, 1	Temporal demand, 1	Performance, 1	Effort, 1	Frustration, 1
1	13	20	15	2	20	20
2	10	10	12	15	12	10
3	12	16	12	14	18	19
4	20	18	20	18	18	20
5	8	16	8	17	13	8
6	12	16	12	19	18	17
7	14	13	17	18	12	18
8	16	10	10	15	17	15
9	15	16	8	13	15	11
10	8	10	10	11	11	7
11	19	20	9	19	19	18
12	16	13	13	14	16	15
13	17	11	15	11	15	11
14	20	20	20	20	19	19
15	10	19	10	11	19	19
16	18	18	1	16	18	16
17	17	20	18	4	19	19
Mean	14.41	15.65	12.35	13.94	16.41	15.41

Table 25. Position mode Task 4 results.

Tester №	Mental demand, 1	Physical demand, 1	Temporal demand, 1	Performance, 1	Effort, 1	Frustration, 1
1	13	20	11	5	20	18
2	11	14	10	10	11	10
3	11	14	12	7	13	8
4	17	20	18	17	18	20
5	11	20	13	20	15	12
6	14	16	12	5	19	13
7	16	16	17	16	15	13
8	14	12	13	9	16	10
9	8	11	9	5	8	9
10	8	10	9	10	10	7
11	19	20	11	18	19	14
12	13	12	15	10	17	15
13	20	15	15	4	17	18
14	18	19	17	14	18	17
15	10	19	10	11	18	18
16	17	17	11	14	17	12
17	18	16	15	2	18	14
Mean	14.00	15.94	12.82	10.41	15.82	13.41

Table 26. Velocity mode Task 1 results.

Tester №	Mental demand, 1	Physical demand, 1	Temporal demand, 1	Performance, 1	Effort, 1	Frustration, 1
1	6	4	5	6	8	1
2	3	2	4	5	3	1
3	5	1	1	9	4	1
4	4	3	3	6	3	2
5	12	2	3	2	3	7
6	5	3	8	17	10	13
7	15	7	10	1	11	6
8	10	5	10	10	13	8
9	10	11	13	7	14	13
10	12	6	6	4	8	4
11	12	8	7	4	7	6
12	8	2	10	10	5	2
13	7	7	3	4	2	9
14	1	1	1	3	4	4
15	3	2	4	5	6	3
16	4	8	2	7	11	2
17	14	12	11	8	13	14
18	9	5	10	7	13	3
19	15	13	9	10	8	6
Mean	8.16	5.37	6.32	6.58	7.68	5.53

Table 27. Velocity mode Task 2 results.

Tester №	Mental demand, 1	Physical demand, 1	Temporal demand, 1	Performance, 1	Effort, 1	Frustration, 1
1	5	4	4	2	6	2
2	3	5	4	7	2	3
3	2	12	1	5	6	2
4	2	18	10	3	10	10
5	9	11	8	19	11	3
6	7	16	15	12	14	5
7	13	15	15	1	14	13
8	6	13	4	2	5	5
9	12	14	13	10	13	9
10	14	16	10	8	14	8
11	12	8	8	5	9	8
12	2	4	5	4	6	2
13	5	9	3	1	6	2
14	1	11	6	3	10	6
15	3	6	3	4	5	5
16	3	15	3	12	10	15
17	16	16	14	5	17	19
18	9	9	7	6	10	4
19	8	16	12	8	9	14
Mean	6.95	11.47	7.63	6.16	9.32	7.11

Table 28. Velocity mode Task 3 results.

Tester №	Mental demand, 1	Physical demand, 1	Temporal demand, 1	Performance, 1	Effort, 1	Frustration, 1
1	11	8	8	6	11	6
2	4	4	6	5	5	3
3	8	16	1	5	11	7
4	11	18	11	10	18	9
5	9	11	11	1	11	1
6	14	18	17	14	20	15
7	17	18	12	9	18	18
8	13	13	7	6	10	9
9	12	13	12	13	15	11
10	16	16	13	3	16	5
11	9	12	11	5	12	7
12	12	14	14	10	13	12
13	12	13	9	6	12	10
14	11	10	6	5	11	5
15	5	7	5	9	7	8
16	10	14	4	12	17	13
17	17	16	14	12	20	18
18	14	11	13	8	15	4
19	12	14	12	9	12	14
Mean	11.42	12,95	9.79	7.79	13.37	9.21

Table 29. Velocity mode Task 4 results.

Tester №	Mental demand, 1	Physical demand, 1	Temporal demand, 1	Performance, 1	Effort, 1	Frustration, 1
1	11	11	8	6	15	8
2	5	6	5	8	8	5
3	6	19	3	7	15	7
4	18	18	11	11	18	15
5	5	9	8	1	11	1
6	17	20	10	6	20	13
7	15	17	15	8	19	13
8	14	14	9	9	11	12
9	14	13	13	13	13	9
10	16	16	13	9	16	5
11	9	12	8	7	12	8
12	8	12	12	10	13	7
13	12	14	6	6	13	8
14	4	14	7	8	14	10
15	5	5	5	5	6	5
16	15	16	15	15	16	8
17	19	16	17	18	19	18
18	15	13	17	7	14	13
19	5	14	10	9	13	10
Mean	11.21	13.63	10.11	8.58	14.00	9.21

Table 30. Position mode Task 1 results.

Tester №	Mental demand, 1	Physical demand, 1	Temporal demand, 1	Performance, 1	Effort, 1	Frustration, 1
1	5	8	6	11	10	8
2	5	3	4	10	9	4
3	4	4	3	9	8	5
4	2	2	5	14	7	10
5	11	2	11	18	12	7
6	20	10	3	17	17	19
7	14	4	14	3	13	11
8	14	8	7	6	11	12
9	12	14	15	8	13	13
10	16	16	16	14	16	11
11	14	12	16	6	13	11
12	2	3	3	3	3	3
13	15	3	6	16	16	16
14	2	2	2	12	3	8
15	6	6	5	7	7	7
16	13	11	8	16	15	17
17	9	3	6	11	5	12
18	12	6	6	15	11	7
19	5	8	9	5	9	9
Mean	9.53	6.58	7.63	10.58	10.42	10.00

Table 31. Position mode Task 2 results.

Tester №	Mental demand, 1	Physical demand, 1	Temporal demand, 1	Performance, 1	Effort, 1	Frustration, 1
1	6	15	7	17	14	14
2	4	8	8	11	8	5
3	4	13	1	4	11	5
4	3	19	11	18	18	18
5	15	13	6	18	15	13
6	19	18	4	8	20	20
7	16	14	14	8	17	16
8	12	12	9	11	12	12
9	13	12	7	16	16	14
10	18	16	16	11	16	11
11	14	12	14	8	13	12
12	6	9	6	5	10	8
13	14	17	10	17	17	17
14	4	8	4	11	5	4
15	7	8	7	9	8	9
16	9	14	6	8	14	14
17	12	14	9	6	14	16
18	15	8	9	17	18	15
19	13	11	17	13	15	15
Mean	10.74	12.68	8.68	11.37	13.74	12.53

Table 32. Position mode Task 3 results.

Tester №	Mental demand, 1	Physical demand, 1	Temporal demand, 1	Performance, 1	Effort, 1	Frustration, 1
1	11	18	10	18	12	15
2	5	8	8	10	8	5
3	3	11	2	5	11	3
4	10	20	15	20	20	19
5	12	11	12	2	13	7
6	18	20	13	19	20	20
7	17	16	17	12	17	15
8	16	14	8	14	15	11
9	12	14	13	15	16	17
10	19	19	16	18	17	16
11	12	11	13	12	13	10
12	12	10	10	14	10	15
13	17	18	10	14	17	18
14	4	5	4	14	19	4
15	8	8	9	10	9	9
16	9	13	5	16	16	15
17	14	7	16	13	15	8
18	15	5	14	16	18	17
19	13	13	13	14	14	13
Mean	11.95	12.68	10.95	13.47	14.74	12.47

Table 33. Position mode Task 4 results.

Tester №	Mental demand, 1	Physical demand, 1	Temporal demand, 1	Performance, 1	Effort, 1	Frustration, 1
1	12	13	7	14	14	11
2	5	8	6	9	8	5
3	2	11	1	7	10	4
4	18	20	15	14	19	15
5	13	16	14	1	16	10
6	14	19	11	7	18	16
7	17	17	14	5	17	13
8	9	11	8	5	9	6
9	10	14	8	17	18	16
10	17	16	16	15	18	15
11	12	10	11	13	12	13
12	5	5	5	2	5	1
13	14	13	9	11	13	12
14	13	15	5	15	17	4
15	8	9	9	11	9	10
16	5	5	7	5	4	4
17	14	17	14	15	18	17
18	16	7	15	6	16	5
19	8	13	12	13	11	13
Mean	12.16	12.58	9.84	9.74	13.26	10.00

Appendix B

Task 3 and 4 score

Active 2R spherical mechanism-based joint

Table 34. Task 3 and 4 score, Active 2R spherical mechanism-based joint joint.

	Velocity mode		Position mode	
Tester №	Task 3	Task 4	Task 3	Task 4
1	1	6	20	20
2	0	2	20	20
3	3	2	20	20
4	6	7	20	20
5	0	6	20	20
6	2	2	20	20
7	6	7	20	20
8	1	10	20	20
9	1	6	20	20
10	0	5	20	20
11	0	3	20	20
12	0	2	20	20
13	3	7	20	20
14	1	6	20	20
15	3	9	20	20
16	1	5	20	20
17	3	9	20	20
Mean	1.82	5.53	20.00	20.00

Differential gear-based design

Table 35. Task 3 and 4 score, differential gear-based design joint.

	Velocity		Position	
Tester №	Task 3	Task 4	Task 3	Task 4
1	0	7	14	15
2	0	2	5	9
3	0	5	4	9
4	1	5	10	11
5	1	0	12	8
6	5	4	8	9
7	2	6	11	20
8	2	7	10	14
9	2	4	11	20
10	0	3	8	14
11	0	2	9	12
12	4	8	13	12
13	0	6	14	20
14	1	1	7	14
15	3	5	10	20
16	2	3	18	20
17	0	4	12	20
18	2	7	10	20
19	2	3	7	15
Mean	1.42	4.32	10.16	14.84

Appendix C

Tester comments

In this Section, the comments that the testers were leaving after the task execution are presented.

Active 2R spherical mechanism-based joint

Velocity control mode

Table 36. Tester comments Task 1

Tester №	Comment
7	It is hard to get the bottom in the beginning
8	Difficult to maneuver
11	It was easier to guess the horizontal boundary. Could not guess the vertical boundary.
12	It is more difficult than it seems.
13	It is complex to predict the end of the border
14	Easy to handle without force feedback

Table 37. Tester comments Task 2

Tester №	Comment
2	The force helps to know where the limits are, but also difficult to reach them. The control is not as precise because you have to do some force every time when leaving the boundaries, it still makes counter force.
4	Fighting with the handle sometimes
6	The force is very high to control it.
7	The force is not with me today!
12	It is much easier than the one without feedback. The feedback helps a lot when you feel it.
13	I feel more comfortable in the second task because I know better how does it work and the force feedback helps too
14	The lowest part of the feedback isn't clear enough. In the higher part it's easy to reach those points.
16	It is easier if your feedback has a support

Table 38. Tester comments Task 3

Tester №	Comment
1	It is quite difficult to move in X and Y at the same time
2	Quite "easy". The diagonal lines are more difficult to accomplish than horizontal/vertical ones. Also the control near the boundaries is more difficult than in the "center" of the image
4	Some points are easy to follow. Other ones, very difficult
6	It is very difficult when the variation of trajectory is pronounced
7	Physically demanding, but I liked it
12	It's the easiest of the first 3 tasks
13	It has been most difficult until this moment because in the border there is some force reaction.
14	When you are reaching the limits, the feedback is a bit rough.
15	Force is so strong

Table 39. Tester comments Task 4

Tester №	Comment
1	This is the most enjoying task
2	Not knowing the trajectory of the point difficulty reaching the position in time. Again, near the boundaries is harder.
4	At first, not very good at following the dot. Then, afterwards, it got better
7	Had to do it right
12	The most difficult moment is when the red dot changes the direction near the border
13	It is the easiest task of the four of velocity test.
14	The handling may have less sensitivity than I expected sometimes.

Position control mode

Table 40. Tester comments Task 1

Tester №	Comment
1	Why is so different to the velocity mode?! It is quite difficult!
2	It is less effort needed to move, but very imprecise. Harder (almost impossible) to move the straight lines. Also noticed some kind of lag. Sometimes the command position and the reached position did not match.
4	Some strange motion in some parts of the workspace. Surely, near singularities.
6	It is more difficult than velocity control
12	It is much more difficult than the velocity one
13	It is much more difficult than the velocity mode to control precisely

Table 41. Tester comments Task 2

Tester №	Comment
1	It is impossible to follow red lines!
2	It is more difficult. Specially, the top horizontal line. The control is not precise. It seems to jump. Not only in zones close to boundaries.
5	The force is too strong
6	It is hard to control the position
12	When it starts moving up and down it's so difficult to predict where it is going to go

Table 42. Tester comments Task 3

Tester №	Comment
1	Position mode with force feedback is bad! I cannot control the end-effector.
2	It is hard to reach the position. Ever the counterforce does not help to achieve the position! Quite difficult. Again, in some position the mechanism "jumps", so you cannot control it.
4	Near the borders, not possible to follow
5	As the force is too high, it increases the difficulty
6	The force is too strong
7	Couldn't do it!
12	It is easier than number 2
13	I perform this task better than I thought. It is still more difficult then the velocity mode.

Table 43. Tester comments Task 4

Tester №	Comment
2	It is difficult to follow the trajectory. Especially in the limits (zones where the mechanism makes the counter force are hard) There are "jumps" difficult to predict. In the central zone is easier and smoother.
3	I've expected it harder than the task 3. But, I think I did better and controls were not so bad
4	Again, very complex near the borders or singularities
5	It is too difficult, because of the force you need apply to do it
9	For this task, I think, it is better the position mode when you are far from the WS boundaries.
11	In my opinion, Velocity control mode is the most intuitive control mode. Force feedback is useful in Velocity mode, but becomes a drawback in Position mode.
12	It is easier when the dot moves around the center position
13	The best perform that I've made in the position mode. I like position mode better more than velocity mode because it is complicated to control, but finally I have could handle it well.
14	I feel like the position test is more demanding and challenging. Therefore once you understand how it works it's more "fun"
15	I need two hands to use it with feedback.
16	Maybe too much force feedback

Differential gear-based design

Velocity control mode

Table 44. Tester comments Task 1

Tester №	Comment
4	It is harder than before
7	I find it noisy! (in both modes)
10	The control of the joystick is better than the first version. It's easier to complete the task
11	Easier than with the joint 1
13	It was easier for me to follow the vertical line than the horizontal one
15	I think it is easier than the previous mechanism. Maybe failed to reach bottom because the "bars" knuckled
16	I give a medium mark to the "Physical demand" because the ball of the joystick is not very ergonomic
19	I think the ball should be a little bit bigger

Table 45. Tester comments Task 2

Tester №	Comment
1	This force feedback is more gentle. My elbows suffer much less.
7	Noisy! Action could be smoother!
10	It is a little bit difficult because the force feedback, but its still easier to perform than the first version of the joint.
11	Force feedback makes it easier to use.
15	The problem is that when reaching the boundaries the counterforce pushes you even if you try to correct the position going back to a "safe" zone. Of course it is easier to predict the limits
16	My level of frustration regards to the vibrations during the work

Table 46. Tester comments Task 3

Tester №	Comment
1	With this joint, the force feedback allows to complete the trajectory much better.
10	This task requires more concentration but with the correct speed, you can do it very well.
13	It was difficult to stop the end-effector exactly in the moment I wanted. By the time it had stopped, I had already missed the point where I had to turn.
15	Again, I think the hand control is easier than the previous one. But, going fast I got lost in some points, maybe Velocity control is not suitable when changing direction. As in the previous one, diagonals were more challenging.

Table 47. Tester comments Task 4

Tester №	Comment
1	It is quite difficult to follow the point near to the workspace border. But it is still being much easier than with the other joint.
10	It is easier to perform than the first joint.
11	It is difficult to follow the red dot in the boundaries
13	There was one moment when I could not stop the end-effector on time and it went far away from the red dot.
15	Better than the previous task, and much better than the previous control.
18	Sometimes it is strange because the feedback force is suddenly very strong and when it has change, the position the joystick is again very soft. That gives you the impression that you have broken something. Somehow this does not feel like it is perfectly normal working.

Position control mode

Table 48. Tester comments Task 1

Tester №	Comment
1	Although position mode is more difficult than velocity mode, I have to say that this position mode is much softer and easier than the one of the other joint.
7	The action of the handle is smoother, but the response is two sensitive!!
10	It is difficult to control but is better than the first version of the mechanism. The joystick is very sensitive.
11	It is difficult to do it fast, but if you do it slowly it makes the task much easier
15	More difficult. There some points I could not reach and I really thought the mechanism could do so.

Table 49. Tester comments Task 2

Tester №	Comment
1	Force feedback in position mode seems to be more sensible than in velocity mode
4	Too much force
5	This task is harder to predict
7	Smother action on the handle than in velocity mode, but the response is too sensitive.
11	In the Velocity mode the feedback makes easier to control the move, but in the position one that feedback makes it more difficult.
13	It was difficult to keep the end-effector fifed in one place
15	I think that, even if this one is easy, I am failing in comparison with the other handle system (which was more difficult and harder)

Table 50. Tester comments Task 3

Tester №	Comment
1	Position mode is the worst one! Reaction forces near the WS border are too high.
2	This joint is easier to control in the position mode.
7	I like the smoother action, not so much the sensitive response!!
10	It is very frustrating to control in this task
11	The "Joint 2" is better than the Joint 1, but the difference between the two joints can feel better in the position mode than in the velocity mode.
13	I felt the joystick was pushing me so much that I had to grab the table!
15	Some lines were quite easy to accomplish, where as others were almost impossible. Near the boundaries I was not able to follow the line. Diagonals were this time easy to make.

Table 51. Tester comments Task 4

Tester №	Comment
1	It could be said that position mode allows to follow the point in a better way than velocity mode, when the point is far from WS border. However, near to the WS border it is much more difficult.
2	Again it is easier to control the position with the second joint
10	It is easier than the first version, however it is still difficult to manage it.
11	I still prefer the Velocity mode, but with this joint the gap between velocity and the position mode is closer, makes the position mode much easier.
13	It was really easier to follow the dot far away from the WS boundaries
15	I really think I have failed. This joint has some good things in comparison with the other one, but still, the counter force makes things hard. It is not easy to control near boundaries.
18	It is difficult to compensate the feedback force to do a uniform movement. In the central area of the joystick workspace is much easier to control the end-effector.

Appendix D

Distribution graphs

Active 2R spherical mechanism-based joint

Tasks 1 and 2

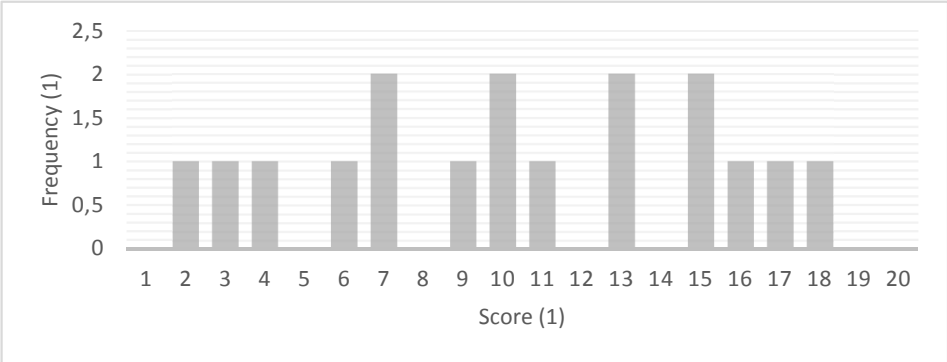

Figure 115. Score distribution, velocity control mode, Task 1.

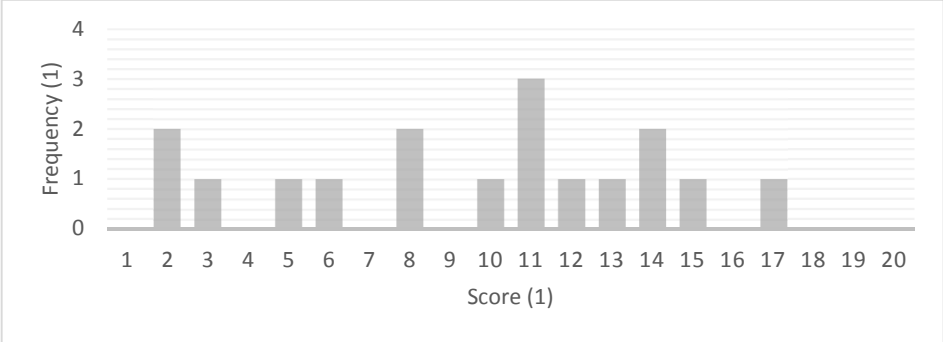

Figure 116. Score distribution, velocity control mode, Task 2.

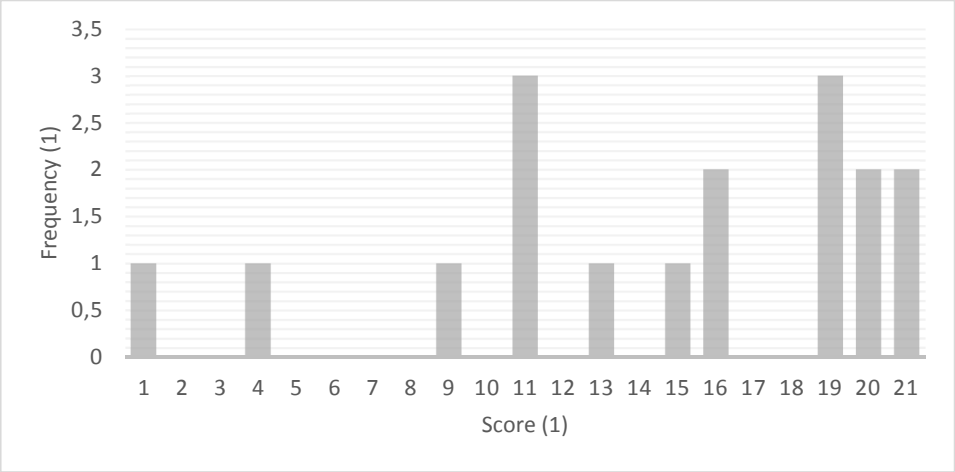

Figure 117. Score distribution, position control mode, Task 1.

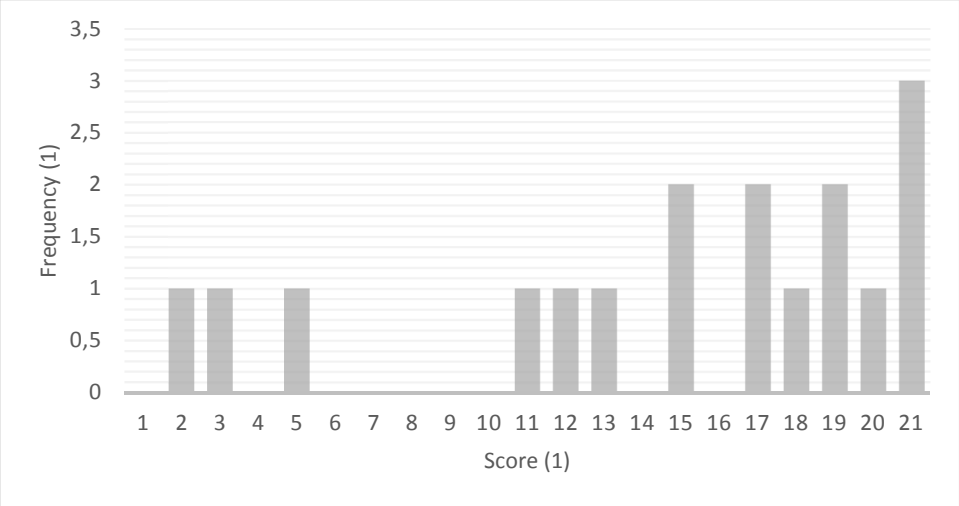

Figure 118. Score distribution, position control mode, Task 2.

Tasks 3 and 4

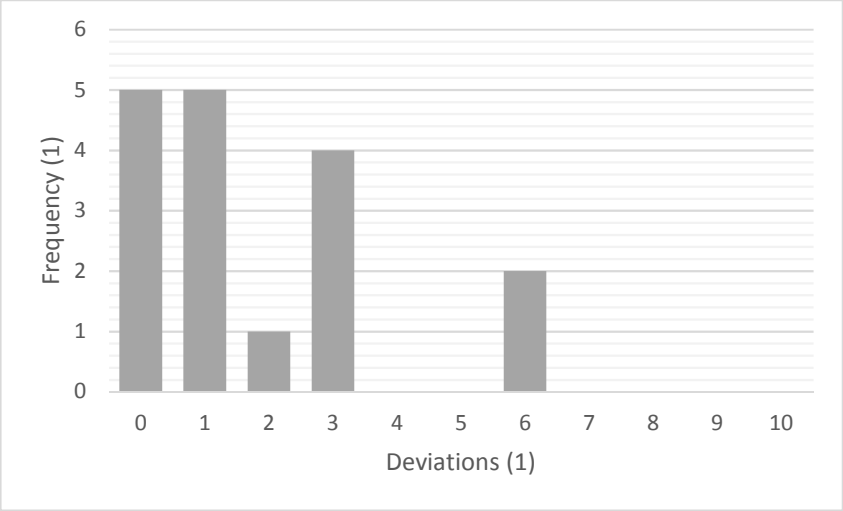

Figure 119. Deviation number distribution, velocity control mode, Task 3.

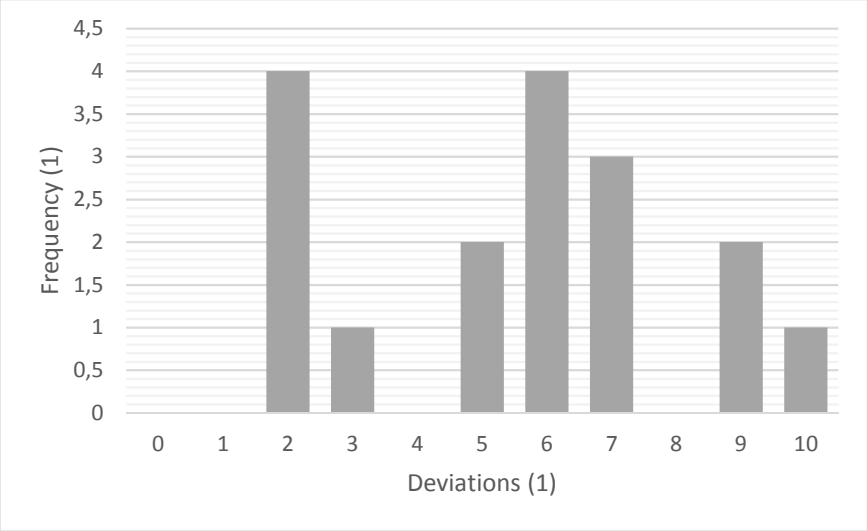

Figure 120. Deviation number distribution, velocity control mode, Task 4.

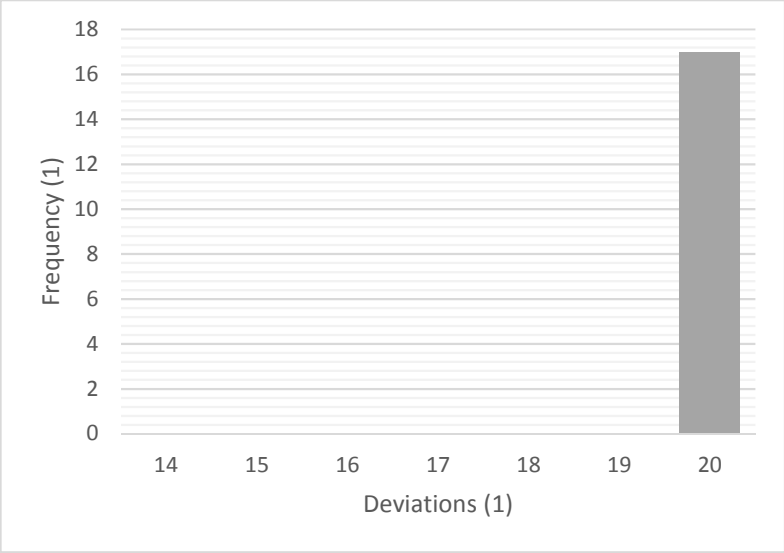

Figure 121. Deviation number distribution, position control mode, Task 3.

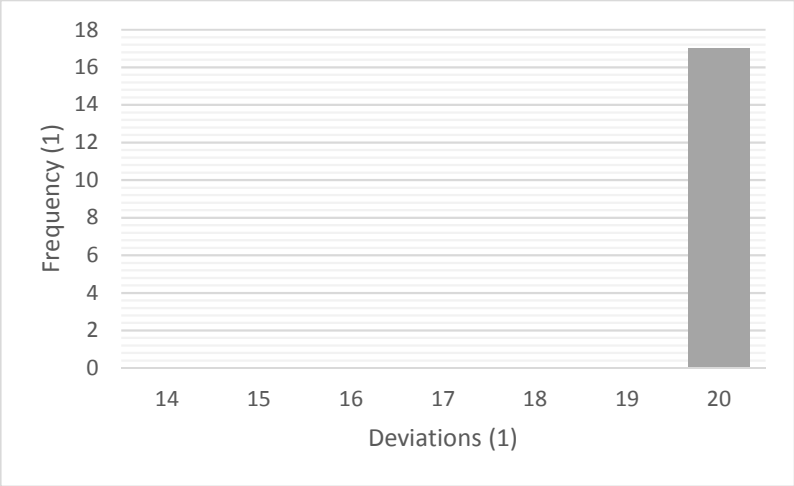

Figure 122. Deviation number distribution, position control mode, Task 4.

Differential gear-based design

Tasks 1 and 2

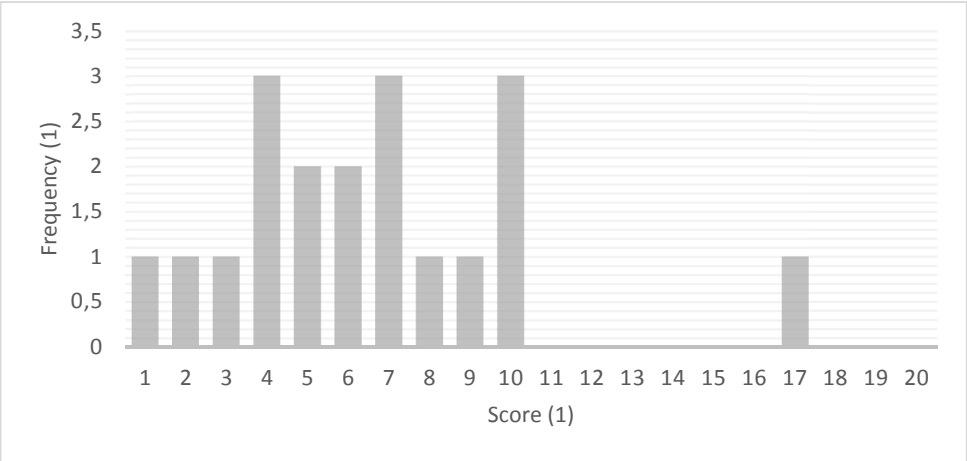

Figure 123. Score distribution, velocity control mode, Task 1.

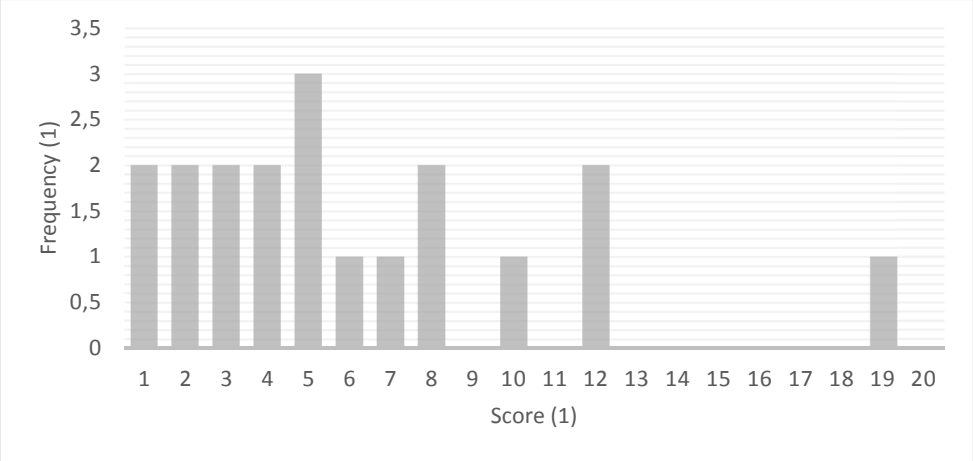

Figure 124. Score distribution, velocity control mode, Task 2.

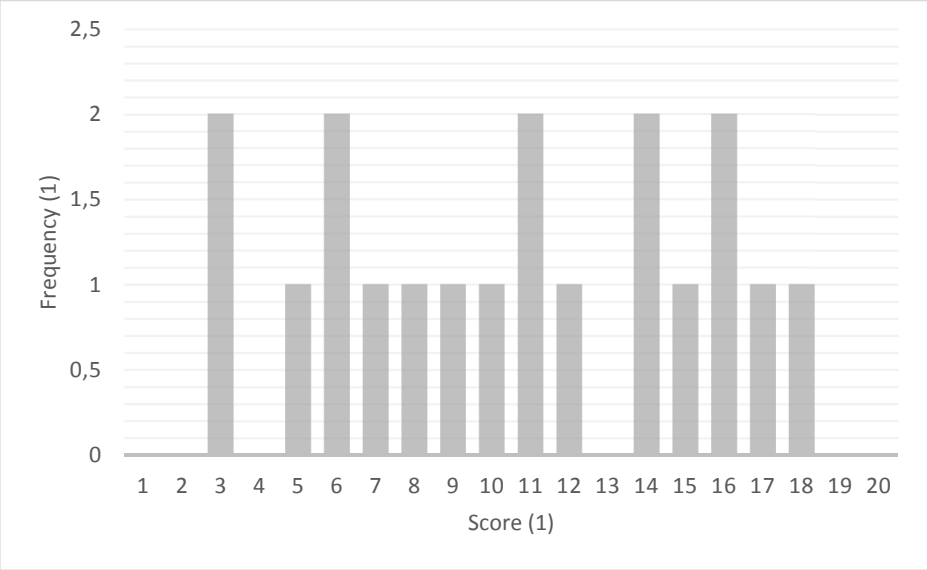

Figure 125. Score distribution, position control mode, Task 1.

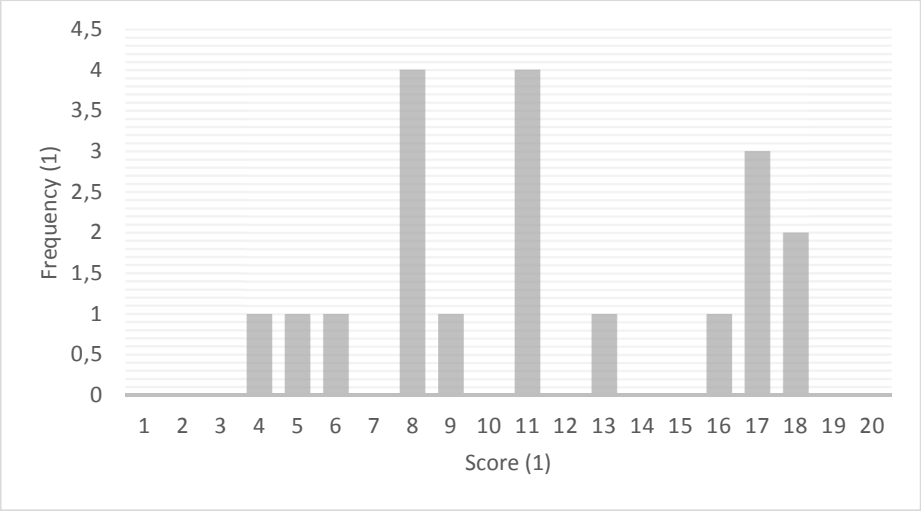

Figure 126. Score distribution, position control mode, Task 2.

Tasks 3 and 4

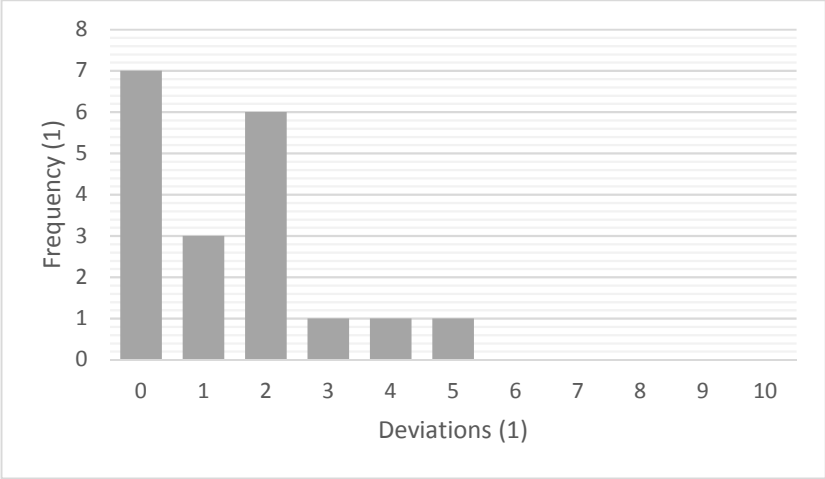

Figure 127. Deviation number distribution, velocity control mode, Task 3.

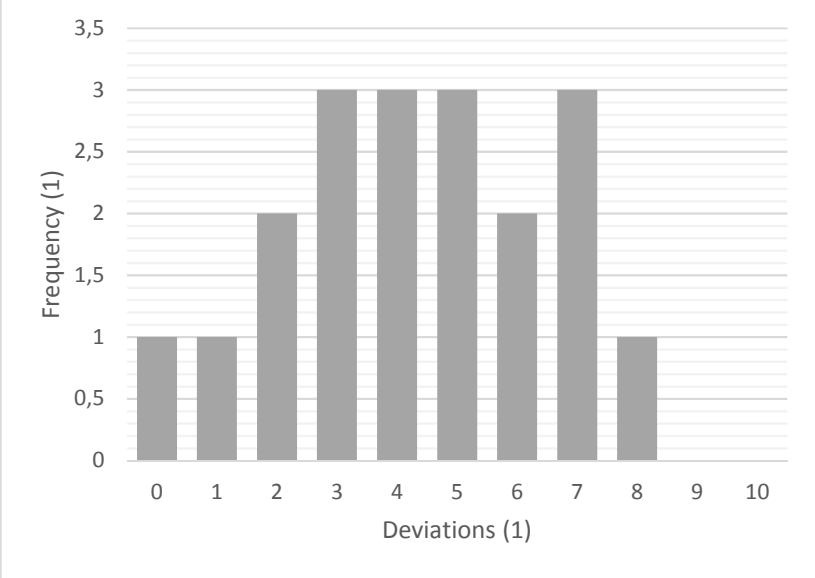

Figure 128. Deviation number distribution, velocity control mode, Task 4.

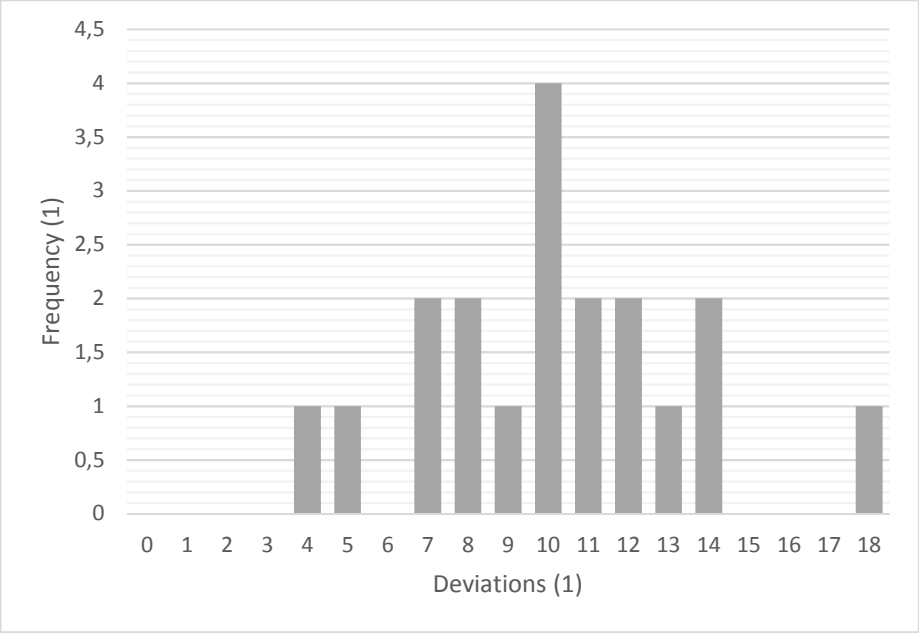

Figure 129. Deviation number distribution, position control mode, Task 3.

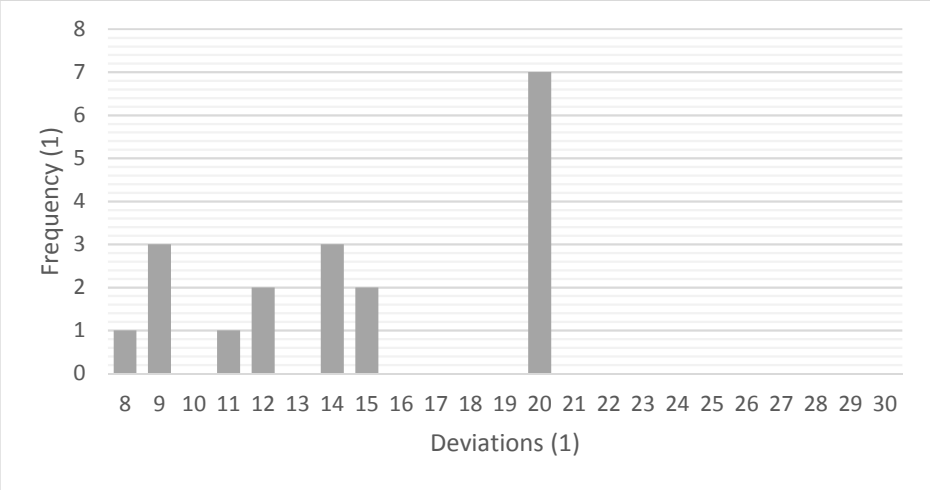

Figure 130. Deviation number distribution, position control mode, Task 4.